

Design and Characterization of a Multi-Vapor Preconcentrator for a
Micro-Scale Gas Chromatograph

by

Rebecca A. Veeneman

A dissertation submitted in partial fulfillment
of the requirements of the degree of
Doctor of Philosophy
(Chemistry)
in the University of Michigan
2009

Doctoral Committee:

Professor Edward T. Zellers, Chair
Professor Mark M. Banaszak Holl
Professor Richard M. Laine
Assistant Professor Stephen A. Maldonado

© Rebecca A. Veeneman

2009

To My Family

Acknowledgements

First, I would like to thank Dr. Edward Zellers. Working with him provided numerous opportunities I would not have had otherwise. I have also learned many valuable lessons from him that I will carry with me throughout my career. His involvement in the WIMS Center also provided unique opportunities for collaboration and provided funding for my time in lab.

I would like to thank my dissertation committee members, Dr. Banaszak Holl, Dr. Laine, and Dr. Maldonado. They have provided various insights into my research and made the major milestones throughout my educational career memorable. I was also lucky enough to have worked with Dr. Sacks. He was a wonderful addition to my committee and the WIMS Center. He is greatly missed.

Dr. Helena Chan, Ms. Katharine Beach, Mr. Robert Gordenker, and Mr. Brendan Casey also deserve acknowledgement for the fabrication and assistance with the micro-preconcentrators. Thank you for all the wire bonds and experimental insights.

A big thank you is owed to members of the Zellers lab, both past and present. I learned a great deal from all of them and I always enjoyed our conversations, scientific or not. Thank you also to the other students that have populated the seventh floor from time to time. Once again, they provided stimulating conversations and much laughter.

Thank you to my new co-workers, especially Dr. Bill Wilson. He helped me tremendously in the last stages of my dissertation. I would also like to thank the “kids’ table”; they provided a welcome break from writing and were always encouraging.

My in-laws have provided a tremendous amount of support throughout my education. JMom, Dad, Norine, Michael, Maria, Micayla, and Mya were always there when I needed them and gave me a wonderful second family. Norine and I could sympathize over graduate school. Michael, always the big brother, pushed me, “when can I call you doctor?”

To Mom and Dad, I couldn’t ask for better parents. You prepared me well for life and I know that I have made you proud. You helped me grow in ways I didn’t know I could, and for that I am very thankful. Kevin, thank you for being my brother. You always motivated me to work harder which helped me become a better student and researcher. You inspire me, and I hope that I can do the same for you.

Last, thank you to my wonderful husband, John. He put up with the long hours and held our family together for 4 years. Without him and all the support he gave me, this dissertation may not have been completed.

It seems as though two pages are not nearly enough to fully express my gratitude to everyone who has helped me, because there are so many and so much more to say.

Thank you.

Table of Contents

Dedication	ii
Acknowledgements	iii
List of Figures	vii
List of Tables	x
Chapter	
1. Introduction.....	1
Micro-Gas Chromatograph	3
Benefits of Preconcentration.....	4
Methods of Preconcentration	6
Adsorption Isotherms.....	7
Equilibrium vs. Exhaustive Preconcentration.....	9
Thermal Desorption	11
Adsorbent Materials.....	14
Micro-Preconcentrator Designs	19
Wheeler Model.....	26
Equilibrium Adsorption Capacity	30
Kinetic Rate Coefficient	34
Mixture Analysis.....	37
Summary	40
References.....	57
2. Characterizing Vapor Adsorption on Graphitized Carbons	
at Low Concentrations	63
Introduction.....	63
Model Descriptions.....	65
Experimental Section.....	69
Materials	69
Isotherm Collection.....	70
Results and Discussions.....	72
Isotherms.....	72
Characteristic Energies from the DR Model.....	74
Physical Interpretation	76
Practical Implications.....	81
Conclusions.....	83
References.....	90
3. Kinetic Factors Affecting the Performance of a Microfabricated	
Vapor Preconcentrator	93
Introduction.....	93
Model Descriptions	95

Experimental.....	99
Device and Materials	99
Breakthrough Testing.....	101
Results and Discussion	102
Breakthrough Volumes	102
Device Modeling.....	105
Conclusions.....	108
References.....	118
4. Wheeler Model Predictions of Binary Mixture Breakthrough Volumes on a Miniature Preconcentrator Filled with Graphitized Carbon.....	122
Introduction.....	122
Single Vapor System.....	124
Binary Vapor System.....	126
Experimental	130
Materials	130
Preconcentrator Construction.....	131
Atmosphere Generation	131
Breakthrough Volumes	132
Results and Discussion	133
Single Vapor Analysis	133
Binary Mixture Analysis.....	135
Modeling of Binary Mixtures	139
Practical Implications.....	141
Conclusions.....	142
References.....	150
5. Conclusions.....	153
Summary of Dissertation	153
Future Work.....	158
Appendix.....	163

List of Figures

Figure		
1-1	A block diagram showing the three main components of a generic gas chromatographic system.....	44
1-2	A microfabricated PCF wirebonded in its testing package.	45
1-3	An array of microfabricated columns are shown with a quarter for size (left).....	46
1-4	Structures of the thiolate monolayer on the MPNs commonly used in the μ GC: n-octanethiol (C8), 1-mercapto-6-phenoxyhexane (OPH), 7-mercaptoheptanitrile (CCN), methyl 6-mercaptohexanoate (HME), and 4-mercaptodiphenylacetylene (left) [108]	47
1-5	A block diagram of the WIMS μ GC	48
1-6	An early prototype of a WIMS μ PCF showing the three materials used for the μ GC	49
1-7	Isotherms at various scales of p/p_{sat} [27].....	50
1-8	The various shapes for the six isotherm types are given [27]	51
1-9	Cartoons representing vapor adsorbing on the adsorbent bed (top) and the resulting concentration profile for the adsorbent bed (bottom) [25]	52
1-10	The μ PCF developed by Voiculescu [40]	53
1-11	The WIMS μ PCF developed by Chan, featuring open bays to hold the adsorbent materials [21]	54
1-12	Example of breakthrough curves showing a symmetric profile from a constant k_v (solid line) and a skewed, asymmetric profile resulting from a changing k_v (dashed line)	55
1-13	Example breakthrough volumes for a range of bed residence times on the WIMS μ PCF.....	56
2-1	Representative adsorption isotherms of a) m-xylene on Carbopack B and b) trichloroethylene on Carbopack X.....	88
2-2	Linearized DR plots of a) m-xylene on Carbopack B and b) trichloroethylene on Carbopack X.....	89
3-1	Pictures of a) the inner cavities of the μ PCF on a dime, b) the multi-stage μ PCF in the testing package, and c) the cPCF with a wrapped heater and thermocouple with a nickel for size (clockwise from bottom left)	112
3-2	Breakthrough curves for toluene (squares) and benzene (circles) are shown for the longest (filled symbols) and shortest (open symbols) bed residence times, τ	113

3-3	Breakthrough curves for a) toluene at 5 mL/min and b) benzene at 4 mL/min are shown to compare the difference in V_{b-10} for the cPCF (open symbols) and the μ PCF (filled symbols).....	114
3-4	Linear plots of breakthrough time vs. bed residence time from the Wheeler model for a) toluene and b) benzene for the μ PCF (filled symbols) and the cPCF (open symbols).....	115
3-5	Breakthrough volume vs. bed residence time curves for a) toluene and b) benzene on the μ PCF (filled symbols) and the cPCF (open symbols).....	116
3-6	Curves reflecting the dependence of k_v on linear velocity are shown for a) toluene and b) benzene for the cPCF (open symbols) and the μ PCF (filled symbols).....	117
4-1	Breakthrough volumes over a range of bed residence times for single vapors (open symbols) and binary mixtures (filled symbols).....	146
4-2	Example breakthrough curve of benzene and toluene in a mixture at similar concentrations (114 and 100 ppb, respectively).....	147
4-3	Example breakthrough curve of heptane and toluene at similar concentrations (100 and 90 ppb, respectively) at a flow rate corresponding to 18 msec.....	148
4-4	Benzene, toluene, and heptane exhibit similar shapes of curves for k_v vs. v_L	149
A-1	The isotherm for benzene on Carbopack B with the DR modeling result using two energies is shown (top).....	164
A-2	The isotherm for trichloroethylene on Carbopack B with the DR modeling result using two energies is shown (top).....	165
A-3	The isotherm for butyl acetate on Carbopack B with the DR modeling result using two energies is shown (top).....	166
A-4	The isotherm for hexanal on Carbopack B with the DR modeling result using two energies is shown (top).....	167
A-5	The isotherm for butanol on Carbopack B with the DR modeling result using two energies is shown (top).....	168
A-6	The isotherm for perchloroethylene on Carbopack B with a single DR equation model (top).....	169
A-7	The isotherm for toluene on Carbopack B with the DR modeling result using two energies is shown (top).....	170
A-8	The isotherm for octane on Carbopack B with the DR modeling result using two energies is shown (top).....	171
A-9	The isotherm for m-xylene on Carbopack B with the DR modeling result using two energies is shown (top).....	172
A-10	The isotherm for α -pinene on Carbopack B with the DR modeling result using two energies is shown (top).....	173
A-11	The isotherm for d-limonene on Carbopack B with the DR modeling result using two energies is shown (top).....	174
A-12	The isotherm for decane on Carbopack B with the DR modeling result using two energies is shown (top).....	175
A-13	The isotherm for hexane on Carbopack X with the DR modeling	

	result using two energies is shown (top).	176
A-14	The isotherm for trichloroethylene on Carbopack X with the DR modeling result using two energies is shown (top).	177
A-15	The isotherm for hexanal on Carbopack X with the DR modeling result using two energies is shown (top).	178
A-16	The isotherm for on butyl acetate Carbopack X with the DR modeling result using two energies is shown (top).	179
A-17	The adsorption isotherm for benzene on Carbopack X with the DR modeling result from a single linear regression is shown (top).....	180
A-18	The adsorption isotherm for butanol on Carbopack X with the DR modeling result from a single linear regression is shown (top).....	181
A-19	The isotherm for 2-butanone on Carbopack X with the DR modeling result using two energies is shown (top).	182
A-20	The isotherm for isooctane on Carbopack X with the DR modeling result using two energies is shown (top).	183
A-21	The isotherm for heptane on Carbopack X with the DR modeling result using two energies is shown (top).	184
A-22	The isotherm for toluene on Carbopack X with the DR modeling result using two energies is shown (top).	185
A-23	The isotherm for 2,5-dimethylfuran on Carbopack X with the DR modeling result using two energies is shown (top).	186

List of Tables

Table

1-1 Adsorbents tested with relevant properties and results from adsorption capacity and desorption tests.....	43
2-1 Physical properties of the compounds tested as adsorbates.....	85
2-2 Results derived from fitting data for Carbopack B to the DR model	86
2-3 Results derived from fitting data for Carbopack X to the DR model	87
3-1 Values of relevant variables and performance metrics of the μ PCF and cPCF.....	111
4-1 Values of W_e for single vapors and mixtures are given along with the mole fraction used to calculate the W_e for the mixture	145

Chapter 1

Introduction

This dissertation focuses on the design and characterization of a microfabricated preconcentrator/focuser (μ PCF) for a microfabricated gas chromatograph (μ GC). The research described here was performed in conjunction with the Engineering Research Center for Wireless Integrated MicroSystems (WIMS) at the University of Michigan and was funded by the National Science Foundation. The WIMS Center fosters collaborative and interdisciplinary research among eight participating universities. Multiple departments from engineering and physical sciences are engaged in the research effort, which facilitates novel approaches to problem solving and systems engineering as well as providing a unique experience for the students. The μ GC is a major project within the WIMS Center and the μ PCF is an integral part of that system [1-3].

The μ GC consists of three main components, which enable the capture, injection, separation, and detection of vapor mixtures (Figure 1-1). The μ PCF serves as the sample collection and injection device to the system (Figure 1-2). The separation module consists of an ensemble of two polymer-coated etched-Si/glass channels with resistive

heaters and temperature sensors that can be independently temperature programmed to achieve a range of separations (Figure 1-3). The detection of the resolved compounds is achieved by an array of chemiresistors (CR), which measure changes in resistance of thin surface films of monolayer protected gold-thiolate nanoparticles (MPN) films as a function of reversible vapor sorption (Figure 1-4).

Microanalytical systems, such as the μ GC described here, are aimed at applications including homeland security, environmental air monitoring, industrial process control, biomarker studies, and medical surveillance [4]. These applications often involve concentration levels in the parts-per-billion (ppb) to parts-per-trillion (ppt) range, which makes detection of the target compounds difficult. To achieve detection limits in this concentration range, preconcentration is required. The μ PCF not only improves the limits of detection (LOD) of the system, facilitating analysis of trace compounds, but also provides a focused injection pulse, which can improve analyte resolution if designed and operated properly.

The following investigations describe the material-vapor interactions inherent to the design and operation of the μ PCF. These studies represent the first attempt to model the capacity and flow dynamics of this device. These data provide a sound basis for guiding the design of future μ PCFs. In this introduction, we will present the background relevant to the research presented here. The needs for preconcentration within micro-analytical systems as well as methods of preconcentration are discussed. Since preconcentration is limited to physisorption for this discussion, adsorption isotherms are presented. The advantages and disadvantages of operating μ PCFs on the basis of equilibrium-based preconcentration versus exhaustive preconcentration are discussed as

an introduction prior to discussing factors that influence preconcentrator operation and design. These factors include efficient thermal desorption as well as adsorbent material choice. A review of μ PCFs, including the current design for the WIMS μ GC is also presented. Last, the thermodynamic and kinetic models used throughout this dissertation to describe the adsorbing rate coefficient, equilibrium adsorption capacity, and mixture analysis are presented.

Micro-Gas Chromatograph

It has been nearly 30 years since the first reported μ GC [5]. Since then numerous efforts have been mounted to develop μ GCs that are capable of capturing, separating, and detecting the components of mixtures of gases and vapors [1-2, 5-18]. The effort underway in the WIMS Center is among these. The block diagrams in Figure 1-5 lay out the analytical sub-system of the WIMS μ GC, with arrows indicating the flow paths followed during the two-step analytical process.

In the first step, air is sampled, using a vacuum pump to collect a predetermined sample volume. This draws large volume of air through the inlet filter to remove any particulates and past a calibration-vapor generator that serves as a source of an internal standard. The volatile organic compounds (VOCs) in the sample volume are collected on a multi-stage μ PCF filled with granular adsorbents. The multi-stage μ PCF is designed such that the least volatile compounds are trapped first on the lowest surface area adsorbent with higher volatility compounds being sequentially trapped on higher surface area adsorbents (Figure 1-6). It can be packed with different adsorbent materials to achieve quantitative trapping of VOCs spanning a wide range of structures and

volatilities [19-21].

After sampling the predetermined volume of air, the flow is reversed by switching a series of valves and the μ PCF is rapidly thermally desorbed with the resulting desorption band being injected into the separation module. The separation module includes a two glass capped spiral silicon channels whose interior walls are coated with commercially available polymers (Figure 1-3). The columns are individually temperature programmed with integrated heaters and pressure tuning can be used to adjust analytes' retention [22-23]. Pressure tuned separation can be achieved with the aid of the valve between the two columns. This valve allows flow to be diverted around the first column, to essentially cease flow in the first column, which allows compounds on the second column to elute further. This is useful for vapor pairs that are separated by the first, non-polar column, but then co-elute from the second column by inserting additional time between the two peaks [23].

After separation is complete, the eluting VOCs are detected by the CR array. The CR array comprises eight sets of interdigitated electrodes, coated with different monolayer protected gold-thiolate nanoparticles (MPNs) (Figure 1-4). The MPNs consist of gold cores with a self-assembled monolayer of functionalized thiolate ligands. As vapors are exposed to the MPN coated CR array the resistances of the films are shifted to varying extents [24]. When combined with retention times, these responses facilitate vapor identification.

Benefits of Preconcentration

As mentioned above, most potential applications of the μ GC require detection

limits of ppb or ppt concentration, but the CR array has inherent detection limits in the high-ppb or low-parts-per-million (ppm) range. It is therefore necessary to employ a preconcentration step. By desorbing the captured vapors into a much smaller volume than initially collected, it provides a preconcentration factor, which can effectively increase sensitivity and reduce the limits of detection of the CR array. The preconcentration factor is determined by dividing the sampled volume, $V_{sampled}$, by the desorbed volume, $V_{desorbed}$:

$$PF = \frac{V_{sampled}}{V_{desorbed}} = \frac{V_{sampled}}{W_h \times u} \quad (1.1)$$

The desorbed volume is found by multiplying the width of injection band, W_h (min), by the desorption flow rate, u (mL/min) [25].

Additionally, the microfabricated columns have a limited total number of theoretical plates, $\sim 12,000$ for each 3-m column [2, 23]. The number of theoretical plates, N , is as a measure of column efficiency and is calculated by:

$$N = 5.545 \left(\frac{t_R}{W} \right)^2 \quad (1.2)$$

where t_r is the retention time (min) and W is the peak width at half height (min) [26]. Typically a non-retained species is used for calculating N , although any analyte could be used. A larger W , stemming from a larger injection band, yields a lower value for N [26]. If the μ PCF is designed and operated as efficiently as possible, a narrow injection band

can be achieved. A narrow injection band, characterized by a smaller W , gives a larger value for N , indicating a higher number of available theoretical plates to achieve separation.

Employing a μ PCF in the μ GC then enhances the performance of the CR array and the separation module. The integration of these three components is critical to the analysis of complex mixtures by μ GC.

Methods of Preconcentration

Preconcentration can be achieved by chemisorption or physisorption. Chemisorption relies on the formation of chemical bonds to achieve sorption, while physisorption relies on mainly on Van der Waals forces for sorption. Chemisorption is not easily reversed, since it requires breaking covalent bonds, and often employs a chemical reagent to facilitate derivitization. Reversal of this process requires a substantial amount of energy and can be a difficult process. This is not a viable option for micro-analytical instruments with goals of field deployment. On the other hand, physisorption, involves weak intermolecular interactions that are easily reversed. The simplicity and reversibility of physisorption makes it the preferred method for preconcentration.

Physisorption can entail adsorption and absorption or both. *Adsorption* occurs only on the surface of a solid. *Absorption* involves diffusion of the analyte into a solid or liquid. Physisorption can be achieved by absorption into solution, cold trapping, and adsorption on solids or thick sorbent films, usually polymeric. Absorption into solution can be used as another method of preconcentration. Since a liquid matrix is employed,

low volatility compounds are often easily trapped and humidity generally does not reduce the efficiency of the absorption. However, the potential loss of sample, analyte dilution, and need for special materials and equipment outweigh the potential advantages [25]. Cold trapping, or cryogenic cooling, captures the analytes on a bare surface or on a sorbent that has been cooled to below room temperature. This approach can capture a wide range of compounds and reduces the chance of decomposition since the analytes have been cooled below its boiling point. Controlling the temperature also facilitates selective adsorption and desorption, by bracketing smaller ranges of compounds with similar boiling points [25].

Because both absorption into solution and cryogenic trapping are difficult to employ with microanalytical system, adsorption on solid surfaces and absorption into thick-films, provides a more practical approach to preconcentration. The simplicity of the process, necessary equipment, and the flexibility of the material choice are key advantages. While these methods have drawbacks, including sample degradation on the sorbent upon desorption, capture of water, and low desorption efficiency for high molecular weight compounds, they can be minimized by carefully choosing the sorbent material and operating parameters [25].

Adsorption Isotherms

Adsorption isotherms give a measure of the amount of adsorbate (the species adsorbing) as a function of the partial pressure (or gas-phase concentration) of the adsorbate at a given temperature (Figure 1-7) [27]. Isotherms are classified by one of six

types, which describe the shape of the isotherm and can reveal features of the adsorbate-adsorbent interaction. Figure 1-8 shows these six isotherm types [27].

Type I isotherms are characteristic of monolayer adsorption, where adsorption reaches a plateau or a limiting value. Type I isotherms are commonly observed for microporous adsorbents where the initial concave portion is due to pore filling. Type II isotherms are initially concave to the pressure axis and then become convex at higher pressures. This isotherm has a short linear section through the mid-area. Type II isotherms are characteristic of non-porous materials that form monolayers initially with multilayer adsorption occurring at higher pressure. Type III isotherms are convex to the pressure axis over the course of the entire isotherm and indicate weak vapor-adsorbent interactions. Type IV, and V are variations of Type II and III isotherms. Type IV isotherms are similar to Type II isotherms except they reach a plateau at high pressures. Type V isotherms are similar to Type III where the isotherm is initially convex to the pressure axis, but like Type IV isotherms, it plateaus at high pressures. These isotherms (Type III, IV, and V) indicate pore filling. Last are Type VI isotherms, the least common, which demonstrates stepwise adsorption indicating the formation of multiple layers.

Porosity is a measure of the void space within the adsorbent material, when compared to the total volume the material occupies. Type I, III, IV, and V isotherms are often given by porous materials, and the shape of these isotherms can provide initial indication of the presence of porosity. The porosity of a material can also be described by the size of the pores of the material. Microporous materials have pores no larger than 2 nm wide and tend to give Type I isotherms. Mesopores are slightly wider, spanning

from 2 to 50 nm. Macropores denote a pore width greater than 50 nm [27]. Porosity can increase the capacity of the adsorbent because it represents additional surface on which adsorption can occur. However, the pore size can also limit the adsorption by acting like a sieve for the adsorbing molecules. Porosity influences the shape of the isotherm, as well as the capacity of the adsorbent material and is thus an important aspect of adsorbent materials.

Equilibrium vs. Exhaustive Preconcentration

Whether considering adsorption on solid surfaces or absorption into adsorbent films, there are two schools of thought with regards to the operation of preconcentrators. Equilibrium-based preconcentration, whose roots lie in chromatography, relies on the concentration on a surface, or in a sorbent film being at equilibrium with the sample air [28-30]. The mass of vapor trapped in the sorbent at equilibrium, M_{eq} is:

$$M_{eq} = C_s V_s \quad (1.3)$$

where C_s is the analyte concentration in the sorbent at equilibrium and V_s is the volume of the sorbent. The partition coefficient, K ($K=C_s/C_a$), is used to substitute C_s with C_a , the analyte concentration in the air, which can be easier to determine:

$$M_{eq} = K C_a V_s \quad (1.4)$$

Since V_s can also difficult to calculate, the analyte retention factor, k ($k=KV_s/V_m$), is used to replace V_s with V_m , the volume of the mobile phase, or the sampled volume:

$$M_{eq} = C_a k V_m \quad (1.5)$$

The analyte retention factor provides a measure of how long the analyte is in the stationary phase in comparison to the time the analyte spends in the mobile phase. It can also be given by $(V_r - V_m)/V_m$, which when used in Equation 1.5 yields:

$$M_{eq} = C_a (V_r - V_m) \quad (1.6)$$

where V_r is the analyte retention volume. When the sample volume is negligible with respect to the retention volume, M_{eq} in Equation 1.6 simplifies to approximately $C_a V_r$. In this case, the mass trapped by the sorbent after equilibrium is equal to the amount of mass contained in a sample volume equal to V_r . If, on the other hand, V_s is much larger than the volume of the sorbent, the mass captured after equilibrium can be calculated from Equation 1.4 [30]

With this method, the captured analyte mass is independent of the sampled volume, but directly dependent on the concentration of the sampled air. Eliminating the need for a defined sample volume is a key advantage of this approach. The sample volume can be as long or as short as needed to achieve equilibrium [28-30]. However, if a purge step is employed, where clean air is passed over the sorbent, a portion of the captured analyte will be lost. The mass of vapor lost can be approximated from the

concentration in the air and the volume used to purge the trap [29]. Lastly, since the mass collected is proportional to the challenge concentration, M_{eq} depends on the sorption isotherm. At low concentrations, the isotherm is presumed to be linear; therefore as the concentration increases, M_{eq} increases, and as the concentration decreases, M_{eq} decreases [28]. However, in the case of a nonlinear isotherm, M_{eq} will not change with challenge concentration as expected; it will not increase or decrease at the same rate of change as the concentration. At the extreme, as in a plateau in the isotherm, M_{eq} will not change at all regardless of increase or decrease in the concentration.

Preconcentrator devices designed for exhaustive trapping on the other hand, capture all the analyte from a given sample volume. As the challenge air concentration is sampled, the analyte is depleted from the sample (Figure 1-9). This technique allows for a range of sample volumes, which directly impact the total analysis time [25, 30]. Exhaustive trapping also usually implies larger partition coefficient and retention volumes, meaning a larger sample volume can be used while still completely adsorbing all the analyte in the challenge concentration. On the other hand, a greater affinity for the sorbent, may lead to difficulties in extracting the analyte from the sorbent. The most likely disadvantage of this method, however, occurs when the pre-determined sample volume is exceeded. In this instance, a portion of the sampled concentration will be lost.

Thermal Desorption

Regardless of which method of preconcentration, equilibrium or exhaustive, recovery of the trapped analytes is a necessary step. With microanalytical systems, only thermal desorption is a viable method. Thermal desorption is achieved by rapidly heating

the sorbent. This evaporates the sample from the sorbent so that the trapped analyte(s) can be analyzed [31]. Thermal desorption allows analysis of the entire preconcentrated amount. It can be achieved relatively quickly and it is fairly simple to implement [25]. It is especially useful for interfacing with gas chromatographs because the thermally desorbed plug can be directly injected onto the separation column. While thermal desorption can lead to sample or sorbent degradation, the increase in sensitivity, achieved with this method outweighs the potential disadvantage [25, 31].

Various factors are known to influence the injection plug resulting from thermal desorption as well as the desorption efficiency, meaning the percentage of trapped species that are recovered. These factors include flow rate through the device, heating rate, and desorption temperature [25, 32]. Considering the injection band first, the best results are achieved with fast heating rates ($\geq 100^{\circ}\text{C}/\text{sec}$) and high flow rates (≥ 5 mL/min). For example, in one study, doubling the heating rate of the preconcentrator can result in a 25% decrease in the injection bandwidth for pentane. The injection band was measured as the width of the pentane peak eluting from the column. Likewise, the same study showed a 4-fold increase in flow rate resulting in a 2.5-fold decrease in bandwidth [32]. The combination of increasing these two rates results in a 4-fold decrease in the width of the injection plug. There is, however, a limit on the maximum flow rate. Sweeping the volume of the adsorbent bed quickly decreases the time between desorption and separation by the column (transport time), but the increased flow rate can also broaden the injection plug once it is injected on the column, which decreases separation resolution and can effectively dilute the injected VOCs [32].

Efficiency of thermal desorption must also be considered. The efficiency of desorption is taken as the mass of vapor desorbed in comparison to the amount of mass sampled. To maximize the efficiency of thermal desorption, the choice of adsorbent material, desorption temperature, and flow rate through the device are important factors. The adsorbent material can effect how efficiently the trapped species can be recovered. For example, a range of materials with different surface areas is employed within the μ PCF. The lowest volatility compounds are trapped on the lowest surface area. Higher volatility compounds are trapped on higher surface area materials. During desorption, the preconcentrator flow is reversed to prevent low volatility compounds from being trapped on high surface area materials. If low volatility compounds are trapped on high surface area materials, adsorption is nearly irreversible and poor recovery of the analytes results, thus lowering the desorption efficiency. Likewise, the desorption temperature relates to preventing these trapped species from decomposing, which would also lead to decreased desorption efficiency.

The desorption temperature is an important aspect of thermal desorption since it is partially dictated by thermal stability of the adsorbent material and it impacts the integrity of the trapped species. The desorption temperature should be maximized to fully evaporate all the trapped species, without exceeding the maximum temperature of the material or surpassing the thermal stability temperature of the analyte [25, 33]. Operating at temperatures higher than that of the thermal stability of the material or analytes can result in poor regeneration of the material and decomposition of the adsorbates, although the exact ranges will vary based on the material and analytes. For the graphitized carbons used here, temperatures of 300°C can be achieved for most VOCs

without decomposition. Optimizing desorption conditions for both narrow injection plugs and high desorption efficiency promotes efficient and accurate sample analysis and is an important consideration when designing and operating μ PCFs. However, the main focus of this dissertation is describing sorbent-vapor interaction.

Adsorbent Materials

More commonly, optimizing thermal desorption involves the choice of adsorbent material rather than the operating temperature, flow rate, or heating rate [25, 31, 34]. Adsorbent capacity (retention volume), desorbed peak width, temperature stability, and the hydrophobic nature are factors that can affect adsorption and desorption [25, 34]. A number of materials, including rubbery polymers, granular polymers, and granular carbon adsorbent, have been previously examined and can be compared in terms of these factors [31, 35]. Supelco, a popular supplier of commercial adsorbents, also provides a technical report, which provides a list of their adsorbents and properties. The report also includes retention and desorption data for 43 different VOCs to aid in choosing the right adsorbent for a given application. These materials include graphitized carbons, carbon molecular sieves, porous polymers, and other adsorbents, including glass beads and charcoal [36].

Thick-film polymers provide viable options as adsorbent materials in μ PCFs because adsorption and equilibrium is achieved relatively quickly since they typically have smaller partition coefficients and smaller breakthrough volumes, in comparison to granular adsorbents [37]. These polymers can be coated on the walls of capillary tubes or spin-coated onto flat surfaces. They can also be functionalized to target specific classes of vapors [37-40]. However, some of the polymeric films examined for use in the WIMS

μ PCFs have lower thermal stability ($\leq 200^\circ\text{C}$), which is disadvantageous when sampling high-boiling compounds that require higher thermal desorption temperatures [38].

Granular adsorbents (porous polymers and carbon-based), on the other hand, generally have higher breakthrough/retention volumes and therefore require a longer time to reach equilibrium. The carbon-based adsorbents are also stable at higher temperatures [31]. A number of granular adsorbent materials have been investigated for potential use in the μ PCF for the WIMS μ GC. Their properties and key features are given in Table 1-1. When choosing materials for the μ PCF in the μ GC, there are specific properties that are integral for successful trapping and desorption. High adsorption capacity (evident from the adsorption isotherms, or retention volume analysis) of VOCs is needed so that a large sample volume can be obtained to maximize preconcentration factor. Since the μ PCF is thermally desorbed, thermal stability is needed along with a narrow desorption peak width and efficient desorption. Lastly, the μ GC is operated at ambient conditions with air as a carrier gas, which can introduce water into the analytical system through humidity. For that reason, hydrophobic materials are ideal for use in analysis. Depending on the target analysis, the properties desired in the adsorbent materials will differ. While we have focused on non-polar adsorbents, a number of polar polymers are available. Chromosorb and Poropak are examples of materials available from Supelco that specifically target polar and functionalized vapors [36].

A number of materials have been previously investigated for use in the μ PCF [37, 38, 41, 42]. These four studies provide the basis for future μ PCF design. Zellers examined two polymers for porous-layer open tubular capillaries. Using a test set of five vapors (2-butanone, trichloroethylene, toluene, m-xylene, and

dimethylmethylphosphonate), 1.0-1.5 cm sections were investigated for use as vapor preconcentrators with challenge concentrations of 5-300 ppm and flow rates of 1 mL/min [37]. Groves investigated 11 preconcentrators with six vapors (m-xylene, 1,1,1-trichloroethane, dichloromethane, 2-butanone, and acetone) to provide an initial screening of these materials. Preconcentrators constructed with 10-140 mg of adsorbent material were challenged with concentrations of 2-200 ppm at 100 mL/min [38]. Last the two studies by Lu examined 43 vapors total, spanning a 10^4 -fold range in vapor pressure. At concentrations of 0.1-1 ppm, the 1-20 mg preconcentrators were challenged at 100 mL/min [41, 42]. The usefulness of these materials for mPCFs was based on their adsorption capacity (retention volume), desorption peak width, and water retention [37, 38, 41, 42]. As seen from Table 1-1, there are two materials in particular that demonstrate large retention volumes, narrow injection bands, with minimal water retention. Carbopack B and Carbopack X provided a convenient balance of adsorption capacity and desorption efficiency, over a wide range of volatilities and chemical functionality. Of the 13 materials examined by Groves [38], Zellers [37], and Lu [41, 42], Carbopack B, Carbopack X, the Dow polymers and carbon molecular sieves had high enough adsorption capacity (retention volumes > 1 L) for the authors to consider these materials potentially useful in a μ PCF. Tenax, Carbopack Y, Carbotrap C, and the thick film polymers exhibited very low adsorption capacity (retention volumes of $\ll 1$ L, although exact numbers were not available) for the subset of VOCs of interest, and the authors concluded that these were inappropriate for use in the μ PCF [41, 42]. Of the remaining adsorbents, the co-polymer XUS565 has low thermal stability (180°C), which was found to limit the range of compounds that can be efficiently desorbed. Of the remaining

adsorbents, the co-polymer XUS465, Carbosieves, and the Carboxens have long desorption peak widths (>3 sec), which do not make them amenable for use in the μ GC [38, 41, 42]. Furthermore, the other carbon molecular sieves retain water, which partially diminishes their usefulness in the μ GC.

While Carbopack B and Carbopack X was shown to have good desorption and adsorption properties for 43 VOCs commonly targeted during indoor air quality analysis, they have limited ranges of volatile analytes that are adequately trapped on each graphitized carbon [41, 42]. The study by Lu provides a general guideline for ranges of vapors expected to be trapped on Carbopack B and X. Through a series of experiments, he determined the sentinel compound for each adsorbent, that is, the highest volatility vapor that was still retained on the adsorbent. In doing so, he determined that, in general, Carboapck B captures compounds with vapor pressures <25 torr, where Carbopack X captures compounds with vapor pressures between 95 and 25 torr. In general, compounds that have vapor pressures above 95 torr are poorly retained on these two materials [41, 42]. Because these carbons have limited ranges of volatility, a third material, Carboxen 1000, is included in the μ PCF to capture the high volatility compounds. Carboxen 1000 is a carbon molecular sieve and will trap water as well, which is important to consider during analysis and preconcentrator design.

Because graphitized carbons perform well for most vapors of interest in terms of adsorption capacity and desorption efficiency, while being hydrophobic, they are the primary material choice for the μ PCF and will be the focus for the remainder of this discussion. Graphitized carbons have been in use for over 20 years and have been treated at >2500°C [43]. The precursor is usually a granular carbon black (formed by heating a

polymeric precursor to 1200°C) [43, 44]. After this process (graphitization), the solid is nonporous with a uniform surface morphology [45]. These nonporous adsorbents ideally yield Type II or IV isotherms. Carbopack B, which is non-porous, should yield Type II isotherms. However, Carbopack X, which is mesoporous, could exhibit Type IV shaped isotherms [27, 43]. Adsorption isotherms of nitrogen and krypton on graphitized carbons yield Type II or Type IV shapes, characteristic of multi-layer adsorption [27]. Additionally, graphitized carbons have homogeneous and non-polar surfaces. Because of this, most molecules, even those with functional groups, adsorb via similar adsorbent-adsorbate interactions [27]. This feature makes the graphitized carbons nearly ideal materials for the μ PCF in the μ GC since the non-specificity allows adsorption of a large range of compounds. Additionally, they are synthetic materials that do not decompose or produce artifacts upon heating, unlike activated charcoal, which is commonly used for air sampling.

Graphitized carbons have been used widely as supports in gas-solid and gas-liquid chromatography [45-52]. Most work exploring graphitized carbons as chromatographic stationary phases entail modification with a liquid or polymer coating to enhance or change the adsorption properties [45-49, 52]. There has been very little GC work done with unmodified graphitized carbons.

Other applications of graphitized carbons include air sampling for VOCs and air cleaning [43-52]. For these applications, graphitized carbons make nearly ideal materials due to their hydrophobic nature and high thermal stability [45]. While these materials have been widely used, they have not been examined at low concentrations. The adsorption capacity and adsorbent-adsorbate interactions at the low-and sub-ppb

concentrations of interest in many target applications of the μ GC and those typically encountered in indoor air monitoring adsorptive behavior has not been explored. Most studies focus instead on concentrations of 10 ppm and higher and extrapolate to lower concentrations [27, 53-60]. Moreover, VOCs have not been examined in depth. The non-ideal gases that have been examined represent a only small subset of VOCs typically encountered in air and indoor environments.

Micro-Preconcentrator Designs

A number of other miniaturized or microfabricated preconcentrator devices have been reported, and they most commonly fall into two categories: those using equilibrium adsorption [37, 39, 50, 61-68] and those relying on exhaustive trapping [6, 19-21, 39, 41, 42]. Within both categories, devices have a range of designs, operating parameters, adsorbent materials that differentiate them and provide range of results for both adsorption capacity and desorption efficiency, including preconcentration factors.

The vast majority of micro-preconcentrators rely on equilibrium adsorption [17, 18, 37, 39, 40, 61-68]. With equilibrium adsorption, thick-film adsorbents are arguably the most commonly used, although the device designs are decidedly different. Conventional, capillary preconcentrators are often used as test platforms for the adsorbent material of interest. Capillary preconcentrators provide a simple design to determine the adsorbent properties as they relate to the device operation, including flow rate, challenge concentration, and adsorbent mass. The early work of Zellers et al. falls into this category [37]. They provided a study determining the feasibility porous layer open tubular capillaries, and used two different coatings: styrene divinylbenzene and

vinylpyridine-divinylbenzene. These two polymers were coated on the walls of capillary tubes, 30 m in length, to yield porous-layer-open-tubular (PLOT) columns and aimed to use these as preconcentrators for microanalytical systems. The PLOT columns examined achieved breakthrough almost immediately (<3 min), even with relatively slow flow rates (1 mL/min), which means they reach equilibrium very quickly. While desorption can be very efficient, these devices give preconcentration factors of only 3-9 [37].

Likewise, Ciucanu used a crosslinked poly(dimethylsiloxane) film coated on a helical support within an 80 mm long silicosteel tube to achieve preconcentration [61]. They hypothesized that the helical configuration provided better adsorption capacity than a coated straight capillary because of increased turbulent flow. This study is one of very few that investigated breakthrough as a function of flow rate. They observed a decrease in breakthrough time as flow rate increased, but did not discuss the implications of these results. Also lacking was a discussion of desorption efficiency, although the injection band provided by the preconcentrator was narrow enough to facilitate separation of four VOCs in less than 1 minute [61].

Other capillary devices relying on equilibrium adsorption use granular or solid adsorbents rather than thick films. For example, Grate used a porous metal support filled with 25 mg of Tenax TA to yield a device 12.7 mm long [62]. By incorporating the metal support, the temperature uniformity improved which enabled preconcentrator-based separations through temperature programmed desorption. By programming the desorption temperature (with rates up to 10°C/sec), a ternary separation (methyl ethyl ketone, toluene, and dimethyl-methylphosphonate) was achieved without the use of a

chromatographic column [62]. While this separation was achieved in under 3 minutes, it is about 3 times longer than other preconcentrator-enabled separations.

Last in this category of equilibrium based capillary μ PCFs are two devices from the Mitra group at the New Jersey Institute of Technology. His group developed both a single stage and dual stage PCF envisioned for used in online monitoring of VOCs [63, 64]. Like Grate, Mitra employed granular carbon adsorbents rather than polymeric films. These devices were constructed with 10 mm of stainless steel tubing but with internal diameters ranging from 0.53 to 1.3 mm i.d. [63]. His dual stage device consisted of a larger “retention trap” (400-800 mg Carbopack C) used to capture the VOCs, with a second, smaller, “injection trap” (20 mg Carbopack C) used to provide a focused injection plug [64]. Both papers gave qualitative discussions of performance, although they were able to demonstrate separation of four light VOCs (methanol, acetone, 1-propanol, and 2-butanone) in less than 1 minute [63, 64].

Other configurations of equilibrium-based preconcentrators have also been investigated. Microfabricated structures can provide easier integration solutions for microanalytical systems while improving preconcentration through narrower injection bands and more efficient desorption. Kim [65], Voiculescu [40], Martin [66], and Davis [39] developed microfabricated preconcentrators in which the adsorbent is deposited atop a micro-heater.

Kim developed a microfabricated preconcentrator as an injector for a μ GC. One of the earlier microfabricated PCFs (ca. 2003), the 960 mm² square device consists of heated channels that are coated with a polymer film [65]. Higher concentrations (20-800 ppm) were investigated and discussions of adsorption capacity and desorption efficiency

were qualitative. This represents one of the earliest microfabricated preconcentrators, but left a significant void to be filled.

The devices developed with the Naval Research Laboratory by Voiculescu and Martin are similar, especially in their applications [40, 66]. Voiculescu used hotplates configured as microbridges, allowing for a larger volume of air through the device (Figure 1-10) [40]. This is in contrast to the hotplate used by Martin, which yields flow perpendicular to the preconcentrator (Figure 1-11) [66]. These square devices are considerably smaller than that developed by Kim [65], being 44 mm² (for the microbridges) [40] and 22 mm² (for the perpendicular flow device) [66], and grossly smaller than the capillary preconcentrators described above, which ranged from 10 cm to 30 m (for the PLOT columns) [37]. While both devices were targeted for homeland security applications, Voiculescu focused only on DMMP [40], a chemical warfare simulant whereas Martin extended the range of compounds to include TNT [66]. Because the microbridges had a larger active area, the amount of vapor collected was larger which results in a higher preconcentration factor (10) when compared to that found with the perpendicular flow device (3) [40, 66]. These devices are notable for their target compounds, but lack the larger range of compounds typically found in the field.

Davis [39] and Manginell [67, 68] yield some of the better performing equilibrium-based preconcentrators. Davis is most notable for the incorporation of both solid adsorbents and polymeric films along with the smaller masses of adsorbents used (9 mg PDMS and 7 mg of Carboxen 1000) [39]. A number of other granular adsorbents were investigated for potential use in their preconcentrator, but only Carboxen 1000 was used to assess performance. The preconcentrator, a micromachined hotplate, was

integrated with a chemiresistor detector. The dimensions of the μ PCF were not given, although they were able to achieve preconcentration factor of 200 for m-xylene [39]. This preconcentration factor is much larger than those achieved by any of the devices reviewed so far and it notable for its integration with the chemiresistor detector.

The work of Manginell on the preconcentrator for the μ ChemLab, Sandia National Laboratory's μ GC, is notable for its integration into the microfabricated GC system [17, 18, 67, 68]. There have been two designs for the μ ChemLab, a planar design and a three-dimensional (3D) design. While the devices reviewed thus far emphasized the preconcentrator factors achieved, Manginell emphasizes the low power consumption, less than 100 mW to achieve 200°C. This is an improvement, since microhotplates typically require >150 mW to achieve 120°C [66] and capillary μ PCFs that require >1W to achieve 200°C [41, 42]. Also notable is the size and sorbent used for these devices. The planar device has an active area of <5 mm² and is coated with a hydrophobic sol-gel layer [67]. The 3D device has a larger active area and traps a larger volume of adsorbate [68]. Various materials have been investigated for use in this device, ranging from the sol-gel used in the planar device to nanoporous carbons and commercially available sorbents.

All of the above devices are capable of producing preconcentration factors, but the short sample times limit the preconcentration factor. Preconcentration factors in this range, while somewhat improving the system's LODs, do not lower the LODs enough to meet the target applications concentrations. It is notable that in these devices, operational parameters are often not described in detail, especially flow rate and challenge concentrations.

As seen from this review, equilibrium-based preconcentrators are prominent within literature. The devices range in design and materials used, but all of them aim to improve the detection of the target compounds. Exhaustive trapping preconcentrators have the same goal, but achieve it very differently. Exhaustive preconcentrators are not as common within the body of literature surveyed, but still fall into two major device design categories: capillary and microfabricated.

Capillary preconcentrator devices have been an ongoing project in the Zellers lab at the University of Michigan. Groves [38] and Lu [41, 42] provide a large data set for capillary preconcentrators. Between the three studies, 11 different adsorbent materials were investigated for a μ PCF (Table 1-1). The devices examined by Lu represent the smallest capillary devices available in literature [41, 42]. His dual adsorbent μ PCF consisted of 3.4 mg Carbopack X and 1.2 mg Carbopack B and was able to quantitatively trap 20 VOCs spanning a 30-fold range in volatility [41]. The 3-stage capillary μ PCF added 1.8 mg of Carboxen 1000 and captured 43 VOCs spanning a 10^3 range in volatility [42]. The devices examined by Lu are not only the smallest of the capillary devices reviewed here, but they also examine the widest range of VOCs. However, this later work from the Zellers group represents the only capillary devices that rely on exhaustive trapping. This work is also some of the only research that fully disclose operational parameters, including flow rate, challenge concentration, and adsorbent mass.

The information gleaned from the capillary devices developed in the Zellers group contributed largely to the design of the μ PCF developed by Tian [19, 20]. Tian's μ PCF is different from the microfabricated preconcentrators described previously not only for relying on exhaustive trapping, but also because the structure is a series of high

aspect ratio slats that act as heaters (Figure 1-6). His single stage μ PCF, consisting of 1.8 mg Carbopack X, yielded preconcentration factors of 5600 (the highest preconcentration factor reported) with 2.25 W [19]. This design was improved when extended to three stages, consisting of 1.6 mg Carbopack B, 1.0 mg Carbopack X, and 0.6 mg Carboxen 1000, and used 0.8 W per stage [20]. While both devices use more power than those developed by Manginell [67, 68], the preconcentration factors achieved with Tian's devices are far better [19, 20]. The work of Chan continued Tian's μ PCF fabrication, but eliminated the slats to provide better flow through the device while still decreasing power consumption [21].

Chan's device, and the device currently employed in the WIMS μ GC, consists of three open cavities with volumes of 4.41, 2.54, and 1.63 mL, which accommodate 1.2, 0.8, and 0.64 mg of Carbopack B, X, and Carboxen 1000 respectively (Figure 1-11) [21]. The device is fabricated from two wafers, one for the microfabricated cavities, and a second for the bulk silicon heater and resistive temperature devices (RTDs). Chan's device requires a total of 1.6 W to achieve a heating rate of 30°C/sec for a 3-stage device, which is equivalent to \sim 0.5 W per stage, an improvement from the previous device [21]. This and the previous devices require more power than other μ PCFs, but they encompass larger quantities of adsorbent mass to ensure exhaustive trapping.

Regardless of design or material, it is rare to find studies that consider the fundamental factors affecting μ PCF performance. Zellers [37], Groves [38], Lu [41, 42], Tian [19, 20], Chan [21], and Manginell [69] represent some of only studies that examine device performance as a function of bed mass, flow rate, or desorption heating rates. The modeling work of Manginell demonstrates the importance of fluid dynamics with

equilibrium based μ PCFs [69]. The work of Zellers [37], Groves [38], Lu [41, 42] and Tian [19, 20] demonstrate the importance of flow rate and bed mass considerations when designing packed bed μ PCFs. The studies presented in this dissertation build upon these studies to provide better guidelines for device operation in terms of material capacity, flow rate, and binary mixtures.

Wheeler Model

When trying to predict the performance of packed beds μ PCFs, the Wheeler model is a useful tool. Originally developed by Wheeler and Robell to describe the saturation of a catalytic bed by a poison [70], it was later modified by Jonas to describe adsorption of organic vapors on activated charcoal [71]. Since then, the Wheeler model has been widely used in determining performance of packed bed respirators filled with activated carbon [54, 55, 72-77]. The modified Wheeler model depicts the capture of vapors in a packed bed as a function of key design and operating variables. The modified Wheeler model is the most common form and is given in Equation 1.7:

$$V_b = \frac{W_e W_B}{C_o} \left[1 - \frac{\rho_B Q}{k_v W_B} \ln \left(\frac{C_o}{C_x} \right) \right] \quad (1.7)$$

where V_b is breakthrough volume (L), W_e the equilibrium adsorption capacity (g/g), W_B is the bed mass (g), C_o is the challenge concentration (g/L), C_x is the fraction of C_o where breakthrough is measured, k_v is the kinetic rate coefficient (min^{-1}), ρ_B is the packing

density (g/cm³) and Q is volumetric flow rate (L/min). For the studies present here, C_x is assigned a value of 0.1 (10%) at which point, $\ln(C_o/C_x)$ become 2.3, a constant.

For any given system, there are specific results we can expect from inspection of the modified Wheeler model. Simplification of Equation 1.7 yields an easier solution for determining the dependence of the Wheeler model parameters on the breakthrough volume:

$$V_b = \frac{W_e W_B}{C_o} - \frac{W_e \rho_B Q}{C_o k_v} \ln\left(\frac{C_o}{C_x}\right) \quad (1.8)$$

First, for a linear isotherm, W_e increases as C_o increases, which means W_e/C_o is a constant, and V_b should not change with changes in C_o . Next, since W_B is in the numerator of the first term in Equation 1.8, we can expect that as W_B increases, V_b will increase as well. The flow rate is in the second term, which is subtracted. Therefore, as Q increases, the second term increases, which results in an overall decrease in V_b .

The bed residence time, τ , is a useful variable for expressing void time and is defined as $W_B/\rho_B Q$ (min). The bed residence time where breakthrough is instantaneous is τ_c , referred to as the critical bed residence time, which can be found by setting $V_b = 0$ in Equation 1.7 and solving for τ .

$$0 = \frac{W_e W_B}{C_o} - \frac{W_e W_B \rho_B Q}{C_o k_v W_B} \ln\left(\frac{C_o}{C_x}\right) \quad (1.9)$$

Simplification of Equation 1.9 and substitution of $W_B/\rho_B Q$ with τ_c yields:

$$\tau_c = \frac{1}{k_v} \ln\left(\frac{C_o}{C_x}\right) \quad (1.10)$$

which shows that τ_c is independent of W_e and W_B and inversely proportional k_v (since C_o/C_x is a constant).

The modified Wheeler model gives the breakthrough volume as a combination of thermodynamic and kinetic factors. The first term in Equation 1.7, $W_e W_B / C_o$, represents the sample volume required to reach W_e at the challenge concentration. This means that for a given challenge concentration a sample volume equal to $W_e W_B / C_o$ is required to capture the amount of vapor on W_B at W_e [38]. The second term in Equation 1.7, containing k_v , describes the shape of the concentration front moving through the adsorbent bed (Figure 1-12). Higher flow rates lead to increased k_v values, which yields a steep, s-shaped breakthrough curve will result. If k_v changes as the front moves through the bed (due to flow rate irregularities), a asymmetric curve will result [54].

Two key variables are required in order to use the model as a predictive tool: W_e and k_v . Only W_e can be determined independently, through thermogravimetric analysis or gas chromatography, but k_v must be determined empirically. While it is possible to determine W_e independently, in most cases it is determined from a series of breakthrough experiments [72]. Measuring V_b for a series of μ PCFs containing different adsorbent masses and plotting vs. W_B yields a straight line with the slope is equal to $m=W_e/C_o$ and the y-intercept equal to $\ln(C_o/C_x)W_e\rho_B/k_vC_o$. The determination of k_v depends on the calculation of W_e (from the slope), meaning errors in the calculation of W_e increase errors

for k_v . The y-intercept is usually near zero, of which the inverse must be taken to calculate k_v . While our studies focused on a C_x of 0.1, other authors choose lower values of C_x , (0.05 and 0.01). This can produce significant errors and can differ depending on the C_x chosen [54]. By using classical models of thermodynamics, as well as kinetic models of flow through packed beds, we can relate W_e and k_v to the V_b for single vapors. Determining V_b as a function of Q allows the verification of empirical correlation models for k_v as a function of linear velocity and particle diameter.

The modified Wheeler model has been used widely to predict the service life of air-purifying respirator cartridges [54, 55, 72-77]. In these instances, the challenge conditions are quite different from typical applications of the μ PCF ($C_o > 100$ ppm and $Q = 50$ L/min). Since the adsorbent beds of the respirator cartridges are at least ~ 50 g, bed residence times are on the order of 0.4 – 1 sec, about 100 times longer than that anticipated and observed with the prototype μ PCF devices tested to date (Figure 1-13) [41, 42, 54, 55, 72-77]. This is important to recognize because a longer bed residence time increases the probability of adsorption occurring, and minimizes premature breakthrough.

Previous work in the Zellers group compared V_b predictions from the Wheeler model to experimental data. Values for W_e and k_v were determined for a select set of vapors on Carbo-pack X, Dow XUS565 (a porous polymer from Dow), and thick film coated capillaries [37, 38, 41]. These values were experimentally determined from breakthrough volume experiments. However, the values obtained from breakthrough experiments for W_e and k_v were not compared to independently determined values. A complete study of W_e and its dependence on vapor-adsorbent pairs and concentration was

not performed. Additionally, the influence of Q on k_v was not examined and challenge conditions (100 ppm, 100 mL/min, 3-5 mg adsorbent) were higher than anticipated for the μ GC (sub-ppb, 25 mL/min, 1 mg adsorbent). This left a significant void to be filled with the research presented here.

Equilibrium Adsorption Capacity

Models describing the adsorption of vapors by (microporous) solids as a function of concentration and temperature have been known for decades. Examples include the Langmuir, Freundlich, Hill-DeBoer, Tempkin, BET, and Dubinin-Radushkevich [27, 54, 56, 77]. Of these, Langmuir, BET, and Dubinin-Radushkevich are the most common. The Langmuir isotherm model is arguably the simplest of the isotherm models because it assumes a finite number of adsorption sites, all of equal energy. It is given by:

$$\theta = \frac{Kp}{1 + Kp} \quad (1.11)$$

where θ is the surface coverage (another way of expressing W_e), K is an adsorption constant and p is pressure [78]. The Langmuir isotherm is limited to a monolayer (Type I). Since graphitized carbons tend to give isotherms other than Type I, the Langmuir model is one of the most useful isotherms [27]. Graphitized carbons are capable of multi-layer adsorption, which can be described by the BET isotherm model. The BET isotherm extends the Langmuir model to include multi-layer adsorption:

$$\theta = \frac{c(p/p_{sat})}{(1 - (p/p_{sat}))\{1 - (1 - c)(p/p_{sat})\}} \quad (1.12)$$

where c is a constant, and p_{sat} is the analyte vapor pressure. BET isotherms typically follow Type II shapes. However, BET lacks a measure of vapor properties, other than p_{sat} . Its adsorption constant, c , is also rather general and does not adequately describe the adsorption phenomena seen here [78].

The Dubinin-Radushkevich model (DR) is based on Polyani's adsorption potential and incorporates material properties as well as vapor properties. The DR isotherm equation is given by:

$$W_e = V_o \rho_L \exp\left[\left(\frac{-RT}{\beta E_o}\right) \ln\left(\frac{p_{sat}}{p}\right)\right]^2 \quad (1.13)$$

where V_o is the micropore volume, ρ_L is the density of the vapor condensed in the micropores, R is the ideal gas constant, T is temperature, β is the affinity coefficient, E_o is the adsorption energy and p_{sat}/p is a concentration term [54]. This equation was the first to introduce micropore filling. They started with Polyani's adsorption potential theory:

$$A = -RT \ln(p/p_{sat}) \quad (1.14)$$

where A is the Polyani adsorption potential [27]. This was then combined with aspects of micropore filling (V_o) and surface adsorption (E_o) to yield their isotherm model.

The DR equation can also be expressed in its linearized form:

$$\ln W_e = \ln(V_o \rho_L) - \left[\left(\frac{RT}{\beta E_o} \right) \ln \left(\frac{p_{sat}}{p} \right) \right]^2 \quad (1.15)$$

This form proves to be useful because E_o and V_o can be determined from the slope and y-intercept. When $\ln(W_e/\rho_L)$ is plotted versus $[(RT/\beta)\ln(p_{sat}/p)]^2$, the slope is equivalent to $(-1/E_o^2)$ and the y-intercept is equal to $\ln V_o$ [54]. The affinity coefficient, β , is used to determine E_o for different vapors. Using a reference vapor (by convention, benzene), for which $\beta = 1$, additional values for E_o can be calculated [79]:

$$\beta_{ben} E_o(ben) = \beta_{vap} E_o(vap) \quad (1.16)$$

Determining E_o for an additional vapor in Equation 1.16 depends on the calculation of β for that new vapor. Common methods of calculating β include taking ratios of molar polarizabilities or molar volumes for the challenge vapor to that of a reference vapor. However, both the parachor and molar volume depend on liquid properties (e.g. surface tension) and can vary due to changes in temperature and pressure. For that reason, polarizability, P_e has been viewed as a more preferable option to calculate β [79]:

$$\beta_{vap} = \frac{P_e(vap)}{P_e(ben)} \quad (1.17)$$

Molar polarizability can be calculated from the refractive index, n_d , the molecular weight, MW , and liquid density, ρ_L , of the vapor of interest, which are readily available [79, 80]:

$$P_e = (MW/\rho_L)(n_d^2 - 1)/(n_d^2 + 2) \quad (1.18)$$

The DR model has been used largely to characterize activated carbons (microporous) [81]. Isotherm data has been largely limited ideal gases and permanent gas hydrocarbons [81-84]. This small range of compounds is not representative of what is typically seen with air sampling. When other hydrocarbons were examined, the functionality was limited to straight-chain alkanes, alkenes, and simple aromatics. Furthermore, these compounds were analyzed by GC [82, 84-86]. The concentrations examined in these studies were high (ppm range). These concentrations are considerably higher than those found in the applications of interest.

The DR model was originally developed to describe the adsorption of gases and vapors on microporous carbons [60], and it has been used to described adsorption on other microporous materials as well [49, 87]. For materials such as the graphitized carbons examined here, which lack microporosity, the V_o term loses its physical meaning. The Dubinin-Radushkevich-Kaganer (DRK) model is a derivative of the original DR model that is often used to describe adsorption on nonporous solids:

$$N_a = N_{am} (DRK) \exp\left[-(A/E_{DRK})^2\right] \quad (1.19)$$

Here $A = RT \ln(p_{sat}/p)$, as found in the DR model.

Thus, $N_{am}(DRK)$ replaces V_o and it is typically evaluated by extrapolation from data collected at vapor concentrations $> 0.1p_{sat}$, where the surface coverage starts to approach

a full monolayer [88-90]. For the current study, the concentrations and surface coverages are far below such levels, rendering the validity of any extrapolations less reliable. For this reason, and since our interest lies primarily in evaluating E_o and W_e values for the adsorbates tested, we have elected to use the original DR expression and to disregard the y-intercept. In fact, Sing points out that materials classified as nonporous may still exhibit behavior characteristic of micropores at low pressures which is the realm in which we are interested [81]. Stoeckli studied the use of the DR model for nonporous carbons and determined that the DR model could be applied [85]. Because of the concentration range that is of interest, the data are well below the monolayer capacity, further arguing for the use of the DR model over the DRK for our studies.

Kinetic Rate Coefficient

Since the equilibrium adsorption capacity can be estimated through the DR model, determining the kinetic rate coefficient, k_v is still required in order to allow predictions of V_b with the Wheeler model. The kinetic rate coefficient is a pseudo first order rate constant describing vapor adsorption on solids. Since it has no theoretical basis, there is only experimental evidence for the dependence of k_v on various material and fluidic properties (e.g., particle diameter and linear velocity). For vapor adsorption on solids, which is a first order reaction with respect to the vapor, the rate of adsorption is limited by the transfer of the vapor to the surface of the adsorbent. A few empirical relationships between k_v and several operating variables have been published. In one of those, k_v depends on linear velocity, v_L (cm/sec), and particle diameter, d_p (cm) [91]:

$$k_v = 1.86v_L^{0.5}d_p^{-1.5} \text{ sec}^{-1} \quad (1.20)$$

Equation 1.20 was empirically determined from experiments with respirator cartridges filled with activated carbon. Using benzene as the challenge vapor, breakthrough times were found for a range of activated carbon adsorbent masses (40-230 g) over a range of linear velocities (120-3000 cm/min). Linear regressions permitted the determination of W_e and k_v from the Wheeler model. Comparing the calculated k_v values obtained from the linear regressions to those obtained from Equation 1.20 gave errors in the calculated values up to 40%. The highest and lowest flow rates gave the best agreement with errors of only 2%, but the poor agreement for the mid-range flow rates prompted additional studies.

Wood and Lodewyckx extended Equation 1.20 to account for vapor interactions with the adsorbent bed [92]:

$$k_v = 13.3\beta^{0.33}v_L^{0.75}d_p^{-1.5}\left(\frac{W_e}{MW}\right)^{0.5} \quad (1.21)$$

where MW (g/mol) is the molecular weight of the analyte. In this model, W_e must be determined beforehand. As with Jonas and Rehrmann, a series of breakthrough experiments (55 experiments in total) were performed for 12 vapors and 7 carbon adsorbents over a range of flow rates to validate the equation [92]. Comparing the experimentally determined values of k_v to those calculated from Equation 1.21 resulted in better agreement between experiment and equation, yielding an r^2 of 0.95 for Equation 1.20 and an r^2 of 0.78 for Equation 1.20 [91, 92].

When accounting for linear velocity, or bed residence time, it is necessary to account for the volume that the adsorbent material occupies in the bed. By convention, with respirator cartridges, the volume of the bed is estimated as the total volume of the cartridge. With microdevices, the ratio of interstitial space to the diameter to the device bed is such that the adsorbent material occupies a significant volume that must be accounted for when calculating bed residence time or linear velocity [93]. Linear velocity can be calculated from the bed residence time by:

$$v_L = d_{PCF} / \tau \quad (1.22)$$

where d_{PCF} is the diameter of the μ PCF (assumed to be a cylinder of circular cross section) and τ is the bed residence time calculated as:

$$\tau = \frac{(V_{bed} - V_{ads})}{Q} \quad (1.23)$$

where Q is the volumetric flow rate, V_{bed} is the total volume of the adsorbent bed, and V_{ads} is the volume of the adsorbent calculated from:

$$V_{ads} = W_B / \rho_B \quad (1.24)$$

where W_B is the mass of adsorbent used and ρ_B is the packing density of the material as supplied by the manufacturer. This method of calculating both the linear velocity and bed residence time provides the most accurate measure for small bed preconcentrators.

As noted before, in order to apply the Wheeler model to untested vapors, both W_e and k_v must be determined. A majority of authors perform a series of breakthrough experiments for a range of adsorbent masses and flow rates and determine W_e and k_v from the resulting linear regressions [38, 54, 56, 72, 77]. Here we determine W_e from thermogravimetric analysis and use published equations for k_v for use in the Wheeler model. This way we could validate the published equations for k_v for micro-devices and use them to improve the predictive capabilities of the Wheeler model.

Mixture Analysis

While W_e and k_v have been examined in the context of the Wheeler model for respirator cartridge service life monitoring and for preconcentrators, few have looked at either in cases involving multi-vapor adsorption or high humidity [75-77, 94-105]. In the case of humidity, few effects on k_v or W_e were observed for relative humidities (RH) below 50% on activated carbon (charcoal) [77, 95, 98]. Since graphitized carbons are hydrophobic, we can expect similar behavior between wet and dry conditions. However, in a binary mixture of organic vapors, W_e and k_v may change. There are various methods available for determining W_e of a binary mixture from a single vapor W_e value. Wood published an extensive review of these methods [106]. The Molar Proportionality Method (MPM) is the simplest model, where W_e for a vapor in a mixture decreases with

decreased mole fraction of the vapor in air [106]. MPM allows for calculation of new W_e values based on the mole fraction of the vapor continuants in the challenge sample:

$$W_{e(t)} = x_1 W_{e(1)}^0 + x_2 W_{e(2)}^0 \quad (1.25)$$

where $W_{e(t)}$ is total amount adsorbed in the mixture (g/g), x_1 and x_2 are the mole fractions of components 1 and 2 and $W_{e(1)}^0$ and $W_{e(2)}^0$ are the amounts (g/g) adsorbed by single vapor 1 and 2, respectively. By this relation, then the amount adsorbed by the individual vapors in the mixture are equal to:

$$W_{e(i)} = x_i W_{e(i)}^0 \quad (1.26)$$

where $W_{e(i)}$ is the amount (g/g) adsorbed by component i in the mixture, x_i is its mole fraction, and $W_{e(i)}^0$ is the amount (g/g) adsorbed by component i as a single vapor. While MPM assumes a limited number of sites for adsorption, it has been applied with reasonable success to large-scale adsorbent beds [97, 99].

Ideal Adsorbed Solution Theory (IAST) provides a way of determining the fraction of each vapor in the mixture adsorbed on the surface. This theory is difficult to apply because of the complexity of the equation and includes a spreading pressure. The spreading pressure is the difference between surface tension of the analyte at the pure vapor-solid interface and surface tension of the analyte at the mixture-solid interface. This implies that the vapor is condensing on the surface of the adsorbent in bulk. While this model has shown measured success, at the concentrations investigated here, this

colligative property is not applicable. The applications of the MPM have also shown success and provide a simpler, more straightforward way of determining W_e for mixtures.

Wood also provides a focused analysis of the effect of mixtures on k_v [107]. He reviewed the mixture data on various respirator cartridges from six different authors and nine different studies with the goal of determining the effect of co-vapors on the adsorption rate coefficient. Wood used values of k_v calculated from the breakthrough experiments for the single vapors and mixtures and calculated ratios of $k_v(\text{mixture})/k_v(\text{single})$. From these studies and his independently collected data, Wood concluded that the effect of mixtures on k_v differs depending on the breakthrough order. Vapors that breakthrough first show no difference for k_v in a mixture as compared to single vapor, that is to say $k_v(\text{mixture})/k_v(\text{single})$ is approximately one. This is because, being the first vapor moving through the bed, it sees the adsorbent bed as if it were a single vapor, not a vapor in a mixture. Vapors that breakthrough second or later exhibit a decrease in k_v by about 15%, i.e., $k_v(\text{mixture})/k_v(\text{single})$ is 0.85. This is only true for vapors with sufficiently different breakthrough curves. For vapors with overlapping breakthrough curves, the 15% decrease is to be applied to both vapors (regardless of breakthrough order). Wood did report significant standard deviations. He found standard deviations of 0.21 for first vapor and 0.24 for second vapors, but did not provide a measure of fit for this correction factor.

Adjusting W_e and k_v for mixtures using the MPM and Wood's correction factor allows the prediction of breakthrough volume from the Wheeler model. In fact, authors who have applied the MPM for mixture analysis reported less than 30% deviation between model and experiment [97, 99]. While Wood has been one of the few that

looked at k_v as a function of binary mixtures, the factors affecting k_v , i.e., linear velocity, were not examined in depth for mixtures.

Summary

This dissertation encompasses both fundamental and applied investigations of materials and preconcentrators. The Wheeler model, DR equation, and other empirical equations are used to determine W_e and k_v , respectively, two key parameters of the Wheeler model describing both thermodynamic and kinetic phenomena. Here an in depth examination is undertaken to more fully understand the adsorption phenomenon of organic vapors on graphitized carbons at low concentrations.

In Chapter 2 the adsorption of a series of volatile organic compounds (VOCs) on the non-microporous graphitized carbons Carbopack X and Carbopack B at air concentrations in the parts-per-billion (ppb) range is assessed in the context of the DR model. Adsorption isotherms were determined gravimetrically at 300 K for 11 or 12 VOCs on each adsorbent at concentrations between 10 and 3,600 parts-per-billion (ppb). Attempts to fit the data to the DR model using a single value of the characteristic adsorption energy failed to yield acceptable correlations in all but two cases. For the remaining 21 cases, it was necessary to apply two separate DR models (adsorption energies) to accurately model the data, with discontinuities in the DR plots occurring at a surface coverage in the range of 1-17 nL/m². Polar vapors and poorly adsorbed non-polar vapors invariably are characterized by lower adsorption energies at lower concentrations, while well-adsorbed non-polar vapors are characterized by higher adsorption energies at lower concentrations. The systematic differences in observed behaviors on these non-

microporous adsorbents are explained in terms of the energies of adsorbate-adsorbent and adsorbate-adsorbate interactions over different ranges of surface coverage. The relevance of these findings to the design of adsorbent preconcentrator modules in micro-analytical systems intended for the determination of trace-level VOCs is emphasized.

The effect of flow rate on the breakthrough volume of a μ PCF and capillary μ PCF was investigated in Chapter 3. Critical bed residence times, defined as the point at which the μ PCF does not trap any vapors, were determined for two vapors (benzene and toluene) on both devices for a <1.5 mg of a single adsorbent (Carbopack X). Benzene and toluene were chosen they represented the best and worst retained compounds on Carbopack X. By collecting breakthrough volumes on both devices for a range of flow rates corresponding to bed residence times of 5-30 msec, we were able to determine critical bed residence times as well as safe operating parameters. Operating the μ PCF at flow rates above 10 mL/min leads to significant reductions in performance (a 50% increase in flow rate leads to a 50% decrease in μ PCF performance). Flow rates greater than 25 mL/min result in immediate breakthrough for benzene. Toluene gave a slightly lower critical flow rate of 15 mL/min.

These results were also considered in the context of k_v and the empirical equations available for k_v . With W_e measured by thermogravimetric analysis, and breakthrough volumes determined for a range of flow rates, the kinetic rate coefficient was calculated. Good agreement was found when comparing the value of k_v found from the breakthrough volume experiments, and k_v calculated from Equation 1.21. A systematic study of this kind has not been performed on adsorbent beds of this size in the range of flow rates examined, which is very near the critical bed residence times of the μ PCF. The

implications of these findings are significant since previous authors have not acknowledged the extent that breakthrough volume is dependent on flow rate. Understanding the dependence of breakthrough volume on flow rate provides better guidelines for operating the μ PCF in order to achieve exhaustive trapping and efficient desorption.

The results achieved in Chapter 2 and 3 allowed for the extension of this work to binary mixtures, found in Chapter 4. Using the results of adsorbent modeling from Chapter 2, we determined the adsorption capacity for each vapor in two binary mixtures, benzene/toluene and toluene/heptane. By once again examining breakthrough volume as a function of flow rate, we generated a data curve on which to build our model. Applying the Molar Proportionality Model allowed the calculation of W_e for each vapor in the mixture. We applied Wood's correction factor for compounds based on their breakthrough order to obtain new values of k_v . This allowed us to extend the Wheeler model determined for single vapors on the μ PCFs to binary mixtures. Fair agreement was found between model and experiment (20% difference).

This research found in this study provides necessary insights into the design and operation of future μ PCFs. Based on fundamental thermodynamic models and empirical kinetic relationships, a unique perspective is provided compared to previous work that has been mainly application driven. The extension of these models and relationships to μ PCFs is also noteworthy since few people have applied these models to devices of this scale.

Table 1.1. Adsorbents tested with relevant properties and results from adsorption capacity and desorption tests.

Adsorbent	Type ^a	Surface area (m ² /g)	Pore size (Å)	t _{max} (°C)	General result	reference
Tenax TA	1	35	2000	350	Low capacity ^b	38, 41
Tenax GR	1	24	-	350	Low capacity	38, 41
Dow XUS493	1	1100	-	-	Water retention	38
Dow XUS565	1	1000	24	180	Long desorption peak ^c	38, 41
Carbopack B	2	100	-	400	Ok	38, 41
Carbopack X	2	250	100	400	Ok	41, 42
Carbopack Y	2	25	-	400	Low capacity	42
Carbotrap C	2	10	-	400	Low capacity	42
Carboxen 569	3	485	5-8	400	Broad desorption	38, 41
Carbosieve SIII	3	820	8-11	400	Broad desorption	38, 41
Carboxen 1000	3	1200	10-12	400	Water retention	41, 42
Styrene divinylbenzene	4	N/A	-	200	Low capacity	37
Vinylpyridine-divinylbenzene	4	N/A	-	200	Low capacity	37

^a1-granular porous polymer; 2-graphitized carbon; 3-carbon molecular sieve; 4-thick-film polymer; ^bLow capacity denote retention volumes <<1L; ^cLong desorption peak denotes a peak width of >3 sec

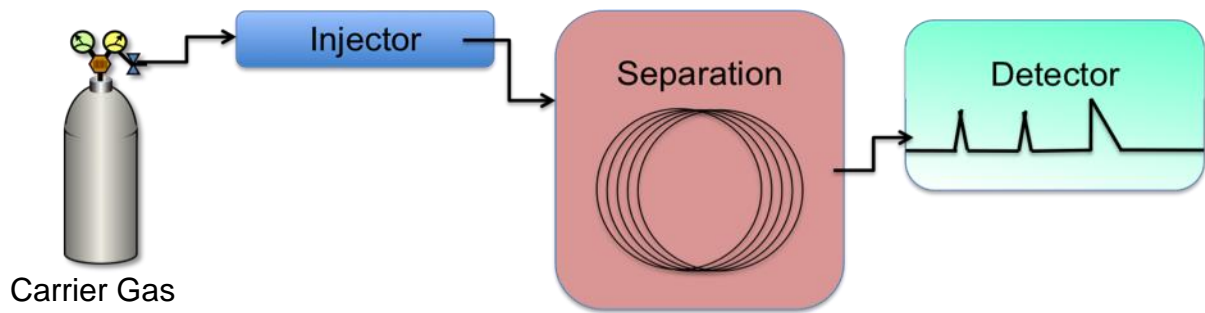


Figure 1-1. A block diagram showing the three main components of a generic gas chromatographic system. For the WIMS μ GC, the μ PCF serves as the injection module, two microfabricated columns are used for separation, and a chemiresistor array is used for detection.

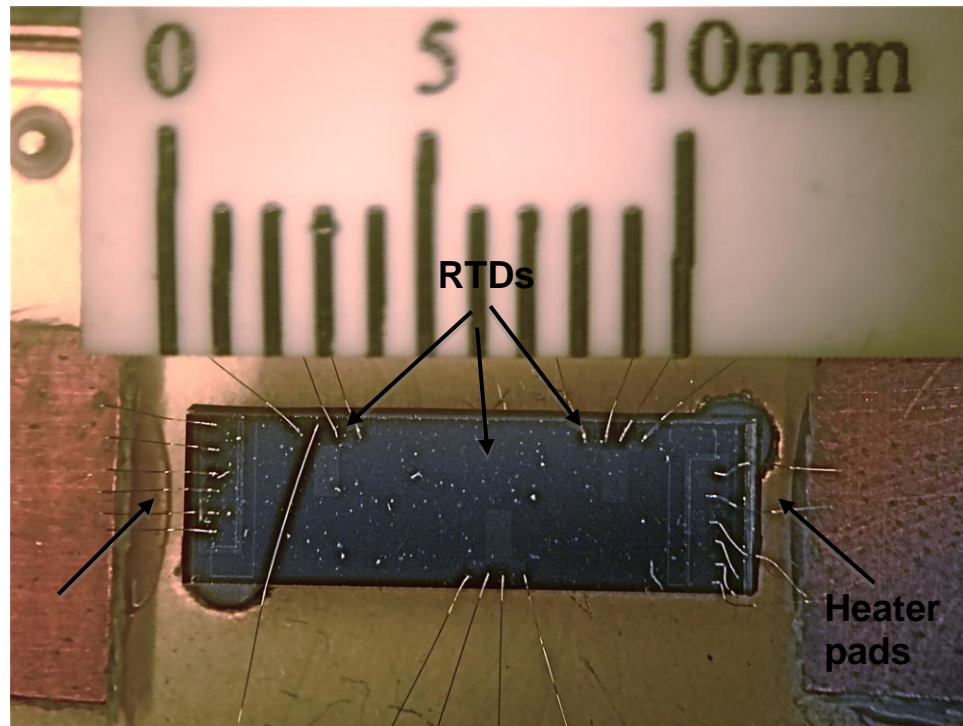


Figure 1-2. A microfabricated PCF wirebonded in its testing package. The WIMS μ PCF consists of three microfabricated channels capable of accommodating up to 1.5 mg of adsorbent material. The wire bonds provide connections for heating and for monitoring the device temperature via resistive temperature devices (RTDs).

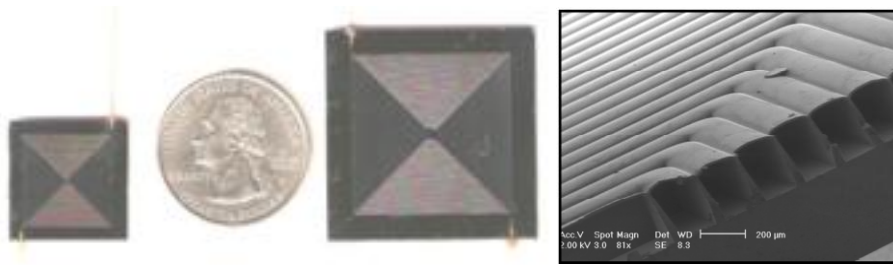


Figure 1-3. An array of microfabricated columns are shown with a quarter for size (left). These columns range from 3 m to 25 cm in length. A cross-section of these columns is shown on the right.

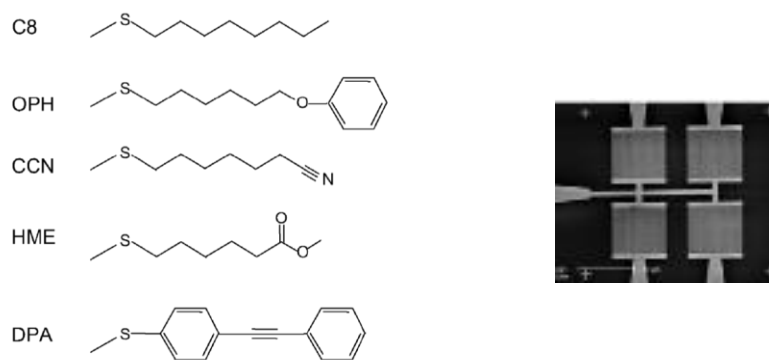


Figure 1-4. Structures of the thiolate monolayer on the MPNs commonly used in the μ GC: n-octanethiol (C8), 1-mercapto-6-phenoxyhexane (OPH), 7-mercaptoheptanitrile (CCN), methyl 6-mercaptohexanoate (HME), and 4-mercaptodiphenylacetylene (left) [108]. The interdigitated fingers of a 4-sensor CR array on which the MPNS are coated are shown on the right. Each CR contains 20 pairs of electrodes with 15 μ m spacing.

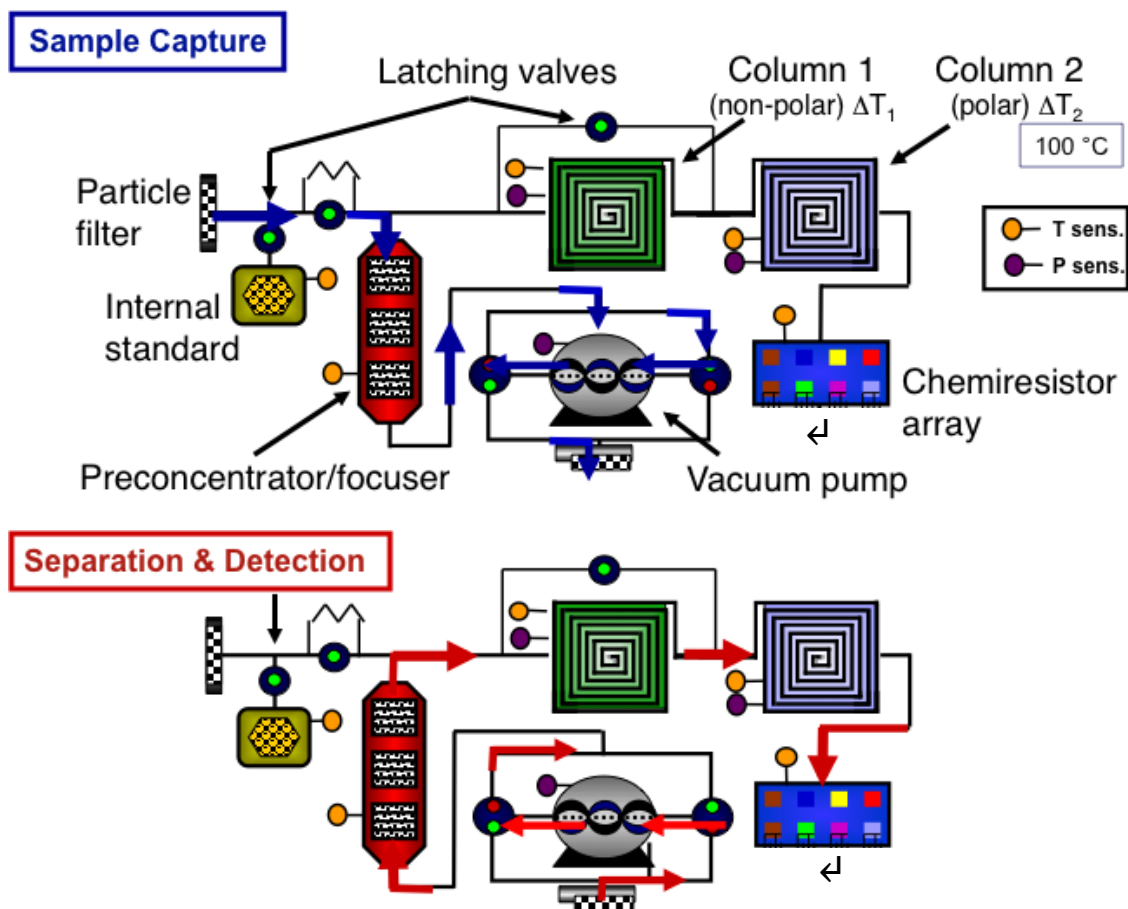


Figure 1-5. A block diagram of the WIMS μ GC. The top diagram shows the sample capture flow path, while the bottom diagram shows the flow path for analysis where the μ PCF is thermally desorbed and the resulting injection band is separated by the dual column ensemble and detected by the CR array.

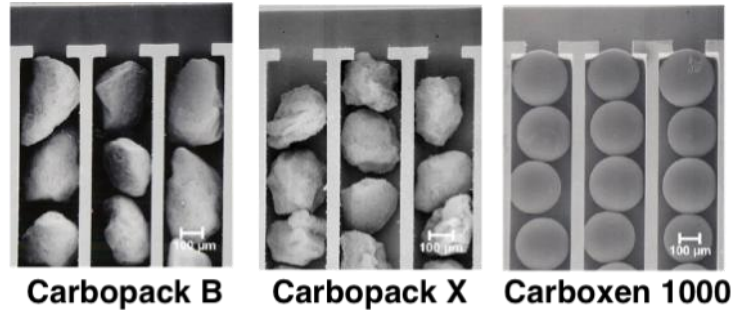


Figure 1-6. An early prototype of a WIMS μ PCF showing the three materials used for the μ GC. The slatted heater structure is filled with adsorbents in order of increasing surface area. From left to right, the specific surface areas are $100 \text{ m}^2/\text{g}$, $250 \text{ m}^2/\text{g}$, and $1200 \text{ m}^2/\text{g}$ for Carbopack B, X, and Carboxen 1000 respectively.

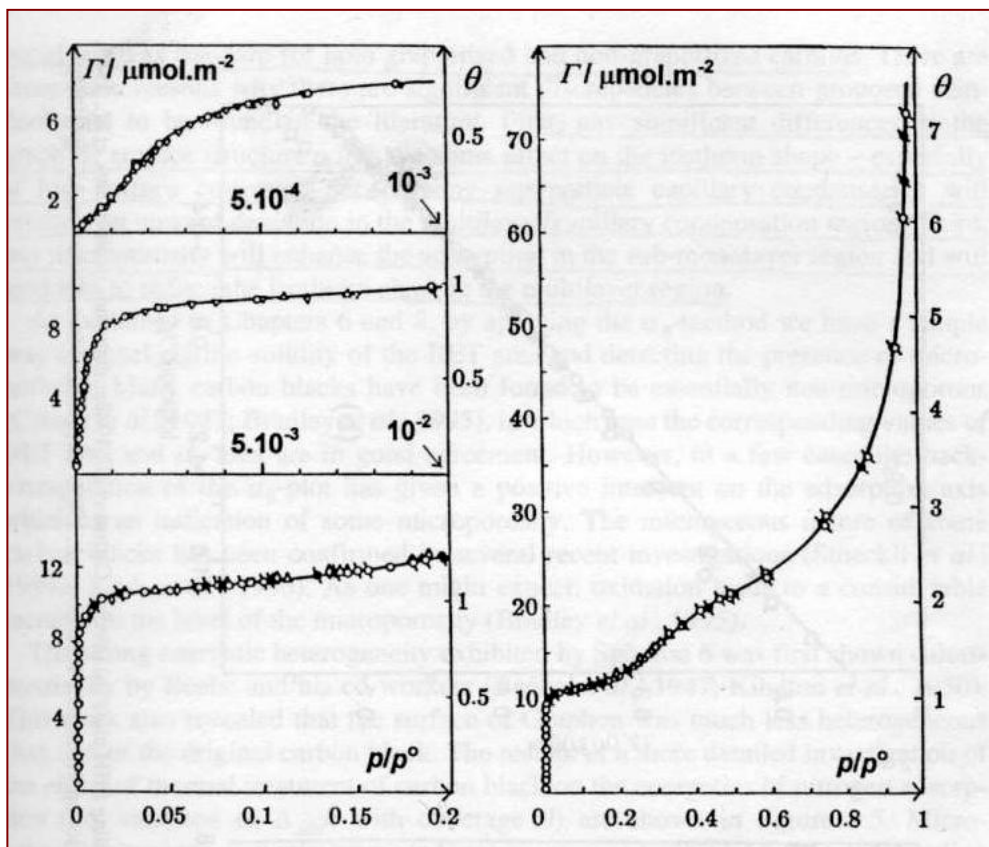


Figure 1-7. Isotherms at various scales of p/p_{sat} [27]. Units of $\mu\text{mol}/\text{m}^2$ are used as a measure of the amount of adsorbate adsorbed per the specific surface area of the adsorbent. Other measures of the amount of adsorbate adsorbed include $\mu\text{mol}/\text{g}$ and g/g .

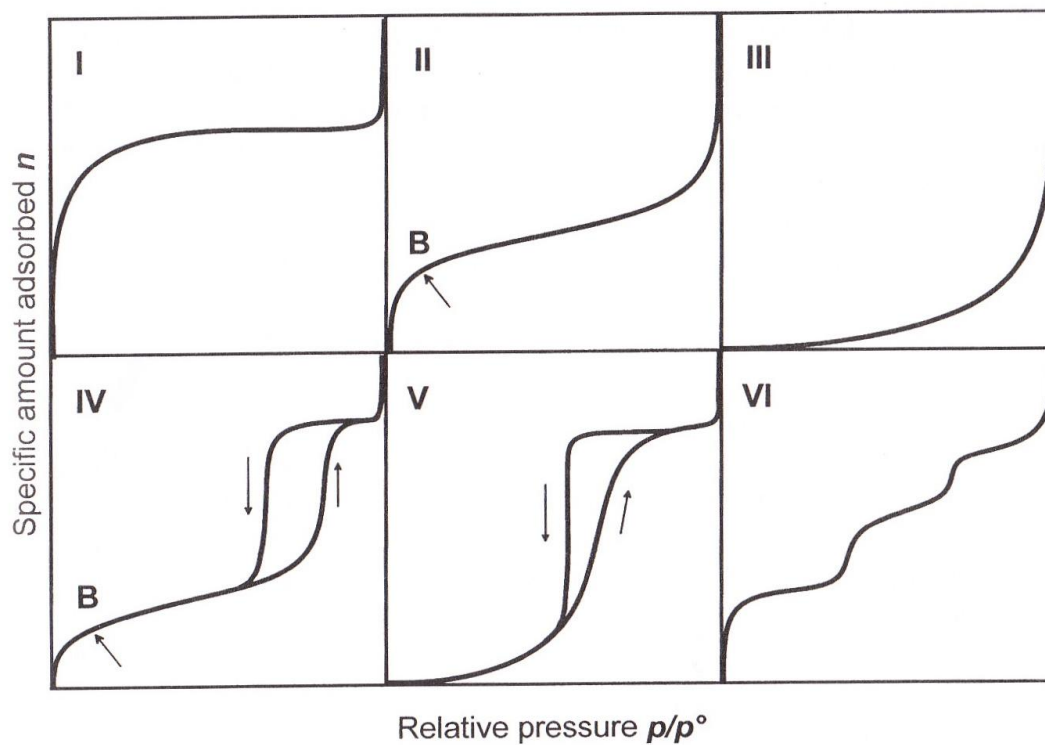


Figure 1-8. The various shapes for the six isotherm types are given [27]. The arrows indicating point B on Types II and IV represent the completion of the first layer and the beginning of multi-layer adsorption. The arrows indicating direction on Types IV and V show both adsorption and desorption. Those isotherms without directional arrows have identical isotherms for both adsorption and desorption.

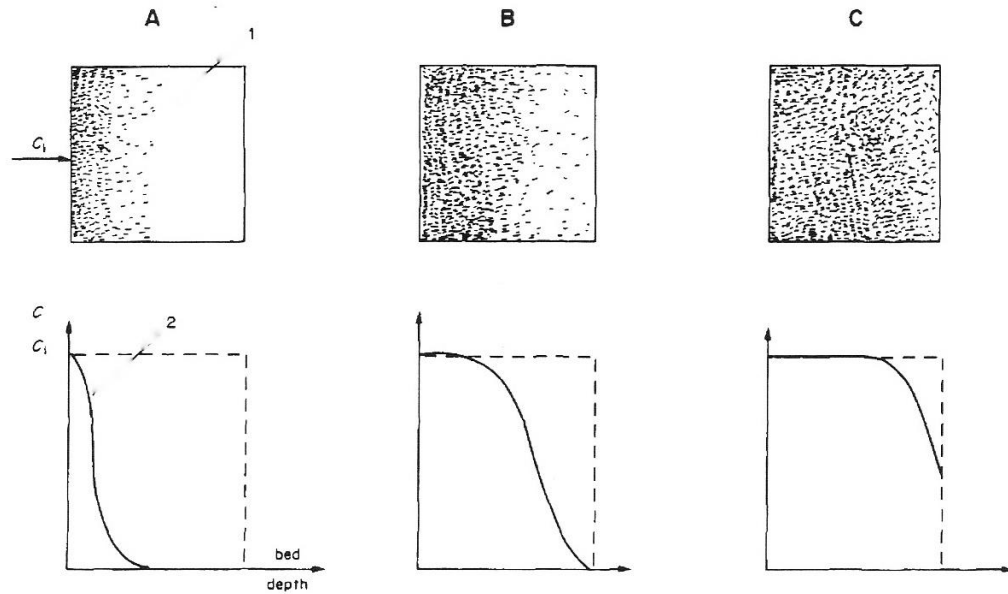


Figure 1-9. Cartoons representing vapor adsorbing on the adsorbent bed (top) and the resulting concentration profile for the adsorbent bed (bottom) [25]. As the vapor stream moves through the bed, the vapor is depleted from the air and trapped on the adsorbent (A). Over time, vapor occupies more sites of the adsorbent material (B) and eventually saturates the adsorbent (C). At this point, a fraction of the incoming vapor concentration is evident at the outlet of the μ PCF (C, bottom).

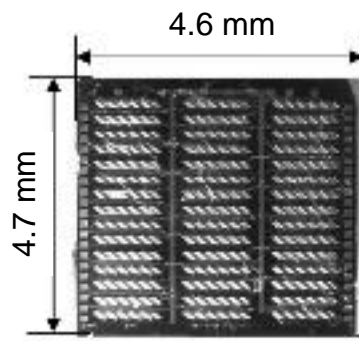


Figure 1-10. The μ PCF developed by Voiculescu [40]. The microbridges are suspended hotplates that allow for flow through the preconcentrator device.



Figure 1-11. The WIMS μ PCF developed by Chan, featuring open bays to hold the adsorbent materials [21]. From left to right, the adsorbent materials are Carboxen 1000, Carbopack X, and Carbopack B.

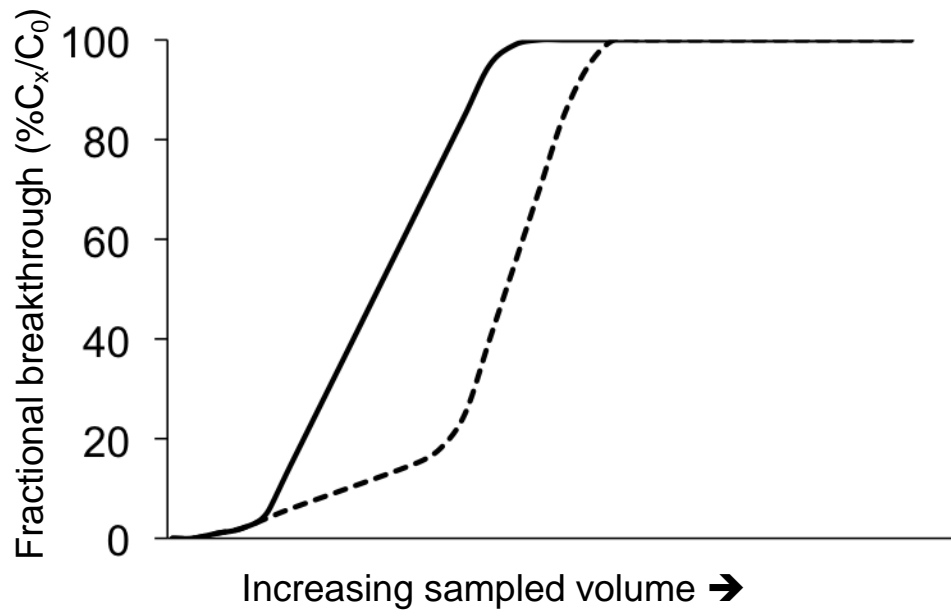


Figure 1-12. Example of breakthrough curves showing a symmetric profile from a constant k_v (solid line) and a skewed, asymmetric profile resulting from a changing k_v (dashed line).

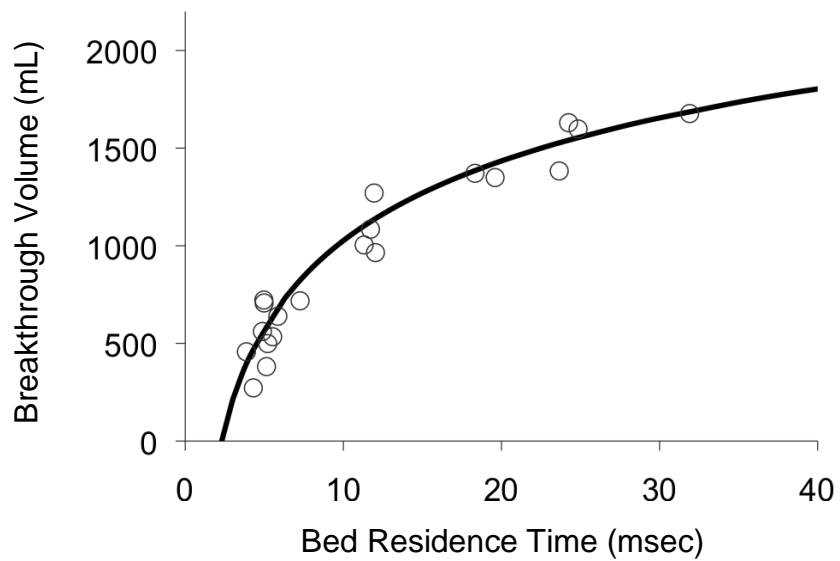


Figure 1-13. Example breakthrough volumes for a range of bed residence times on the WIMS μ PCF. Bed residence times for the μ PCF are 100 times longer than those observed on activated carbon filled respirator cartridges.

References

- [1] E. T. Zellers, W. H. Steinecker, G. R. Lambertus, M. Agah, C. –J. Lu, H. K. L. Chan, J. A. Potkay, M. C. Oborny, J. M. Nichols, A. Astle, H. S. Kim, M. P. Rowe, J. Kim, L. W. da Silva, J. Zheng, J. J. Whiting, R. D. Sacks, S. W. Pang, M. Kaviany, P. L. Bergstrom, A. J. Matzger, C. Kurdak, L. P. Bernal, K. Najafi, and K. D. Wise, *Technical Digest 2004 Solid-State Sensor and Actuator Workshop*, Hilton Head, SC, **2004**, Transducer Res. Foundation, Cleveland, pp. 61-66.
- [2] E. T. Zellers, S. Reidy, R. Veeneman, R. Gordenker, W. Steinecker, G. R. Lambertus, H. Kim, J. Potkay, M. P. Rowe, Q. Zhong, C. Avery, H. Chan, R. Sacks, K. Najafi, K. Wise, *Proc. 2007 Solid-State Sensor and Actuator Conf.-Transducers 07*, Lyon, France, **2007**, pp. 2091 - 2094.
- [3] WIMS Center, accessed online, <http://wimserc.org>
- [4] WIMS annual report
- [5] S. C. Terry, J. H. Jerman, and J. B. Angell, *IEEE Trans. Electron Dev.*, **1979**, 26, 1880.
- [6] P. R. Lewis, R. P. Manginell, D. R. Adkins, R. J. Kottenstette, D. R. Wheeler, S. S. Sokolowski, D. E. Trudell, J. E. Byrnes, M. Okandan, J. M. Bauer, R. G. Manley, and G. C. Frye-Mason, *IEEE Sensors J.*, **2006**, 6, 784.
- [7] C. –J. Lu, W. H. Steinecker, W. –C. Tian, M. C. Oborny, J. M. Nichols, M. Agah, J. A. Potkay, H. K. L. Chan, J. Driscoll, R. D. Sacks, K. D. Wise, S. W. Pang, and E. T. Zellers, *Lab on a Chip*, **2005**, 5, 1123.
- [8] C2V Concept to Volume, accessed online, <http://www.c2v.nl>
- [9] A. de Mello, *Lab on a Chip*, **2002**, 2, 48N.
- [10] SLS Micro Technology, accessed online, <http://www.sls-micro-technology.de>
- [11] M. Stadermann, *Anal. Chem.*, **2006**, 78, 5639.
- [12] R. R. Reston and E. S. Kolesar, *J. Microelectromech. Syst.*, **1994**, 3, 134.
- [13] C. M. Yu, M. Lucas, J. C. Koo, P. Stratton, T. DeLima and E. Behmeyer, *Proc. ASME Micro-Electro-Mechanical Systems*, Anaheim, CA, **1998**, pp. 481–486.
- [14] U. Lehmann, O. Krusemark and J. Muller, *Proceedings Micro Total Analysis Systems Workshop*, Enschede, Netherlands, May **2000**, pp. 167–170.

- [15] H. Noh, P. J. Hesketh and G. C. Frye-Mason, *J. Microelectromech. Syst.*, **2002**, 11, 718.
- [16] G. E. Spengler, *Anal. Chem.*, **1998**, 70, 4805.
- [17] G. Frye-Mason, R. Kottenstette, C. Mowry, C. Morgan, R. Manginell, P. Lewis, C. Matzke, G. Dulleck, L. Anderson and D. Adkins, in *Proceedings Micro Total Analysis Systems Workshop*, ed. J. M. Ramsey and A. van den Berg, Kluwer, Dordrecht, The Netherlands, **2001**, pp. 658–660.
- [18] R. P. Manginell, M. Okandan, R. J. Kottenstette, P. R. Lewis, D. R. Adkins, J. M. Bauer, R. G. Manley, S. Sokolowski and R. J. Shul, in *Proc. 7th International Conf. on Miniaturized Chemical and Biochemical Analysis Systems – mTAS '03*, Squaw Valley, CA, **2003**, pp. 1247–1250.
- [19] W. C. Tian, S. W. Pang, C. J. Lu, and E. T. Zellers, *J. Microelectromech. Sys.*, **2003**, 12, 264.
- [20] W. C. Tian, H. K. L. Chan, C. J. Lu, S. W. Pang, and E. T. Zellers, *J. Microelectromech. Sys.*, **2005**, 14, 498.
- [21] H. K. L. Chan, S. W. Pang, R. A. Veeneman, E. T. Zellers, and M. Takei, *Proc. 2005 Solid-State Sensor and Actuator Conf.-Transducers-05*, Seoul, Korea, **2005**, pp. 2091 - 2094.
- [22] S. Reidy, D. George, M. Agah, and Sacks, R. *Anal. Chem.*, **2007**, 79, 2911.
- [23] G. Lambertus and R. Sacks, *Anal. Chem.*, **2005**, 77, 2078.
- [24] W. H. Steinecker, M. P. Rowe, and E. T. Zellers, *Anal. Chem.*, **2007**, 79, 4977.
- [25] J. Namiesnik, *Talanta*, **1988**, 35, 567.
- [26] K. J. Hyver, *High Resolution Gas Chromatography 3rd edition*, Hewlet Packard: **1989**.
- [27] F. Rouquerol, J. Rouquerol, and K. Sing, *Adsorption by Powders and Porous Solids*, Academic Press: London, **1999**.
- [28] B. Egorov, M. J. O'Hara, and J. W. Grate, *Anal. Chem.*, **2006**, 78, 5490.
- [29] H. P. Tuan, H. –G. Janssen, and C.A. Cramers, *J. Chrom. A.*, **1997**, 791, 177.
- [30] G. Ouand and J. Pawliszyn, *Anal. Bioanal. Chem.*, **2003**, 366, 1059.
- [31] M. Harper, *J. Chrom. A.*, **2000**, 885, 129.

- [32] J. J. Whiting and R. D. Sacks, *J. Sep. Sci.*, **2006**, 29, 218.
- [33] J. Sanchez and R. Sacks, *J. Sep. Sci.*, **2005**, 28, 22.
- [34] E. Woolfenden, *Indoor Built Environ.*, **2001**, 10, 222.
- [35] R. Yang, *Adsorbents: Fundamentals and Applications*, Wiley Science: Hoboken, New Jersey, **2003**.
- [36] J. Brown and B. Shirey, *Technical Report for Supelco*, T402025, Bellefonte, PA, **2001**.
- [37] E. T. Zellers, M. Morishita, and Q.-Y. Cai, *Sens. Actuators B*, **2000**, 67, 244.
- [38] W. A. Groves, E. T. Zellers, and G. C. Frye, *Anal. Chim. A.*, **1998**, 371, 131.
- [39] C. E. Davis, C. K. Ho, R. C. Hughes, and M. L. Thomas, *Sens. Actuators B*, **2005**, 104, 207.
- [40] I. Voiculescu, R. A. McGill, M. E. Zaghoul, D. Mott, J. Stepnowski, S. Stepnowski, H. Summers, V. Nguyen, S. Ross, K. Walsh, and M. Martin, *IEEE Sensors J.*, **2006**, 6, 1094.
- [41] C.-J. Lu and E. T. Zellers, *Anal. Chem.*, **2001**, 73, 3449.
- [42] C.-J. Lu and E. T. Zellers, *The Analyst*, **2002**, 127, 1061.
- [43] D. Vitkuske, *The Reporter*, **2005**; 23.1, 3.
- [44] G. R. Hill and H. M. Fox, US patent 4,005,181, **1975**.
- [45] F. Bruner, G. Crescentini, and F. Mangani, *Chromatographia*, **1990**, 30, 565.
- [46] F. Bruner, P. Cicciooli, F. Di Nardo, *J. Chrom.*, **1974**, 99, 661.
- [47] N. V. Kovaleva and K. D. Shcherbakova, K. D., *J. Chrom.*, **1990**, 520, 55.
- [48] F. Bruner, G. Bertoni, and P. Cicciooli, *J. Chrom.*, **1976**, 120, 307.
- [49] F. Bruner, G. Crescentini, F. Mangani, and L. Lattanzi, *J. Chrom.*, **1990**, 517, 123.
- [50] R. Lebeda, A. Lodyga, and A. Giera, *Mater. Chem. and Phys.*, **1997**, 51, 216-232.

- [51] A. R. Mastrogiacomo, E. Pierini, and L. Sampaolo, *Chromatographia*, **2000**, 52, 345.
- [52] F. Bruner, P. Ciccioli, and F. Di Nardo, *J. Chrom.*, **1974**, 99, 661.
- [53] EPA TO-17, Compendium of Methods for the Determination of Toxic Organic Compounds in Ambient Air, Report No. EPA/625/ R-96/010b, US Environmental Protection Agency, Washington, DC, 2nd edn, 1997.
- [54] G.O. Wood, *Carbon*, **2002**, 40, 1883.
- [55] G. O. Wood and E. S. Moyer, *Am. Ind. Hyg. Assoc. J.*, **1989**, 50, 400.
- [56] G. O. Wood, *Carbon*, **1992**, 30, 593.
- [57] K. Dettmer and W. Engewald, *Anal. Biochem.*, **2002**, 373, 490.
- [58] A. R. Mastrogiacomo, E. Pierini, and L. Sampaolo, *Chromatographia*, **2000**, 52, 345.
- [59] E. Matisova and S. Skrabakova, *J. Chrom. A*, **1995**, 707, 145.
- [60] F. Stoeckli, *Carbon*, **1998**, 36, 363.
- [61] I. Ciucanu, A. Caprita, A. Chiriac, and R. Barna, *Anal. Chem.*, **2003**, 75, 736.
- [62] J. W. Grate, N. C. Anheier, and D. L. Baldwin, *Anal. Chem.*, **2005**, 77, 1867.
- [63] S. Mitra and C. Yun, *J. Chrom. A*, **1993**, 648, 415.
- [64] C. Feng and S. Mitra, *J Chrom A*, **1998**, 805, 168.
- [65] M. Kim and S. Mitra, *J. Chrom.A*, **2003**, 996, 1.
- [66] M. Martin, M. Crain, K. Walsh, R. A. McGill, E. Houser, J. Stepnowski, S. Stepnowski, H.-D. Wu, and S. Ross, *Sens. Actuators B*, **2007**, 126, 447.
- [67] R.P. Manginell, G.C. Frye-Mason, R.J. Kottenstette, P.R. Lewis, C.C. Wong, *Tech. Digest 2000 Sol.-State Sensor and Actuator Workshop*, Transducers Research Foundation, Cleveland, OH, USA, **2000**, pp. 179-182.
- [68] P.R. Lewis, R.P. Manginell, D.R. Adkins, R.J. Kottenstette, D.R. Wheeler, S.S. Sokolowski, D.E. Trudell, J.E. Byrnes, M. Okandan, J.M. Bauer, R.G. Manley, G.C. Frye-Mason, *IEEE Sens. J.*, **2006**, 6, 784.
- [69] R. P. Manginell, S. Radhakrishnan, M. Shariati, A. L. Robinson, J. A. Ellison, R.

- J. Simonson, *IEEE Sensors J.*, **2007**, 7, 1032.
- [70] A. Wheeler and A. J. Robell, *J. Catalysis*, **1969**, 13, 299.
- [71] L. A. Jonas and J. A. Rehrmann, *Carbon*, **1972**, 10, 657.
- [72] P. Lodewcky, G. O. Wood, and S. K. Ryu, *Carbon*, **2004**, 42, 1351.
- [73] Y. H. Yoon and J. H. Nelson, *Am. Ind. Hyg. J.*, **1984**, 45, 509.
- [74] G. O. Nelson, A. N. Correia, and C. A. Harder, *Am. Ind. Hyg. Assoc. J.*, **1976**, 37, 280.
- [75] G. O. Nelson and C. A. Harder, *Am. Ind. Hyg. Assoc. J.*, **1976**, 37, 514.
- [76] Y. H. Yoon, J. H. Nelson and J. Lara, *Am. Ind. Hyg. Assoc. J.*, **1996**, 57, 809.
- [77] G. O. Wood, *J. Occup. Environ. Hyg.*, **2004**, 1, 472.
- [78] P. Atkins, *Physical Chemistry 6*, W. H. Freeman and Company, New York: **1999**.
- [79] K. E. Noll, D. Wang, and T. Shen, *Carbon*, **1989**, 27, 239.
- [80] Lide DR, editor. *Physical Constants of Organic Compounds*, in CRC Handbook of Chemistry and Physics. Internet Version 2007, (87th Edition), Taylor and Francis, Boca Raton, FL.
- [81] K. S. W. Sing, *Carbon*, **1994**, 32, 1311.
- [82] P. J. M. Carrott and K. S. W. Sing, *J. Chrom.*, **1987**, 406, 139.
- [83] C. Pierce and B. Ewing, *J. Phys. Chem.*, **1964**, 68, 2562.
- [84] P. J. M. Carrott, R. A. Roberts, and K. S. W. Sing, *Langmuir*, **1988**, 4, 740.
- [85] A. Andreu, H. F. Stoeckli, and R. H. Bradley RH, *Carbon*, **2007**, 45, 1854.
- [86] N. N. Avgul and A. V. Kiselev, *Chemistry and Physics of Carbon*, **1965**.
- [87] H. F. Stoeckli, D. Huguenin, and A. Laederach, *Carbon*, **1944**, 32, 1352.
- [88] P. J. M. Carrott, M. Brotas De Carvalho, and K. S. W. Sing, *Adsorption Sci Tech*, **1989**, 6, 93.
- [89] P. J. M. Carrott, M. M. L. Ribeiro Carrott, I. P. P. Cansado, and J. M. V. Nabais, *Carbon*, **2000**, 38, 465.

- [90] D. Hugi-Cleary, S. Wermeille, and F. Stoeckli, *Chimia*, **2003**, 57, 611.
- [91] L. A. Jonas and J. A. Rehrmann, *Carbon*, **1974**, 12, 95.
- [92] G. O. Wood and P. Lodewcky, *Am. Ind. Hyg. Assoc. J.*, **2003**, 64, 646.
- [93] G.O. Wood, personal communication.
- [94] G. O. Wood, *Am. Ind. Hyg. Assoc.*, **1987**, 48, 622.
- [95] T. Hall, P. Breyse, M. Corn, and L. A. Jonas, *Am. Ind. Assoc. J.*, **1988**, 49, 461.
- [96] Y. H. Yoon, J. H. Nelson, J. Lara, C. Kamel, and D. Fregeau, *Am. Ind. Hyg. Assoc. J.*, **1992**, 53, 493.
- [97] C. A. Robbins and P. N. Breyse, *Am. Ind. Hyg. Assoc. J.*, **1996**, 57, 717.
- [98] P. Lodewyckx and E. F. Vansant, *Am. Ind. Hyg. Assoc. J.*, **1999**, 60, 612.
- [99] L. A. Jonas, E. B. Sansone, T. S. Farris, *Am. Ind. Hyg. Assoc. J.*, **1983**, 44, 716.
- [100] Y. H. Yoon, J. H. Nelson, J. Lara, C. Kamel, and D. Fregeau, *Am. Ind. Hyg. Assoc. J.*, **1991**, 52, 65.
- [101] Y. H. Yoon, J. H. Nelson, J. Lara, C. Kamel, and D. Fregeau, *Am. Ind. Hyg. Assoc. J.*, **1992**, 53, 493.
- [102] P. M. Swerengen and S. C. Weaver, *Am. Ind. Hyg. Assoc. J.*, **1988**, 49, 70.
- [103] H. J. Cohen, D. E. Briggs, and R. P. Garrison, *Am. Ind. Hyg. Assoc. J.*, **1991**, 52, 34.
- [104] N. Vahdat, P. M. Sweargen, and J. S. Johnson, *Am. Ind. Hyg. Assoc. J.*, **1994**, 55, 909.
- [105] N. Vahdat, *Carbon*, **1997**, 35, 1545.
- [106] G. O. Wood, Report LA-UR-00-5268. Los Alamos, NM: Los Alamos National Laboratory, **2000**.
- [107] G. O. Wood, *Carbon*, **2002**, 40, 685.
- [108] M. P. Rowe, K. E. Plass, K. Kim, C. Kurkak, E. T. Zellers, and A. J. Matzger, *Chem. Mater.*, **2004**, 16, 3513.

Chapter 2

Characterizing Vapor Adsorption on Graphitized Carbons at Low Concentrations

Introduction

Graphitized carbons are used extensively as solid supports in gas-liquid chromatography, as stationary phases in gas-solid chromatography [1-5], and as adsorbents in air sampling devices used to characterize indoor and ambient air quality with regard to contamination by volatile organic compounds (VOC) [6-9]. Features that make these non-polar materials attractive for such applications include their high purity, controlled surface area, homogeneous surface morphology, and thermal stability [8].

Our interest in graphitized carbons lies in their potential to serve as adsorbents in miniaturized preconcentration devices for portable and micro-scale gas chromatographic (GC) instruments designed to analyze complex VOC mixtures at low concentrations in the field [10-16]. For such an application it is necessary to minimize the adsorbent mass in order to reduce heating power requirements and injection bandwidths upon thermal desorption, while maintaining sufficient mass to prevent breakthrough of vapors during sample capture. In a series of previous studies, our group has explored various aspects of preconcentration using the non-microporous graphitized carbon blacks Carbopack B (C-B) and Carbopack X (C-X), and several other adsorbents in small packed beds

[12, 13, 17]. Tests of breakthrough volumes as a function of concentration, bed mass, and mixture complexity have been performed, and multi-bed preconcentrators have been successfully implemented in prototype GC instruments [15, 16, 18]. Yet, a detailed study of the adsorption isotherms of target VOCs was never undertaken.

The multi-adsorbent preconcentrator configurations used in these instruments are similar to those used in standard methods for sampling ambient and indoor air for trace-level contaminants, except that the quantities of adsorbents used are vastly smaller [9]. Surprisingly, despite the widespread use of graphitized carbons as air sampling media in these methods, the adsorption behavior of VOCs on these materials at the low- and sub-parts-per-billion (v/v) concentrations typically encountered in ambient- and indoor-air quality monitoring has not been explored. Rather, most fundamental studies focus on concentrations in the ppm range and above [19-23]. Furthermore, the number of VOCs whose adsorption isotherms have been characterized on such adsorbents is but a small fraction of those commonly found as air pollutants in ambient and indoor environments [20-23].

In this article we present data on the adsorption of 17 VOCs on C-X and/or C-B at air concentrations in the ppb-range (surface coverages $\ll 1 \mu\text{mole}/\text{m}^2$), and results of attempts to fit the data to the Dubinin-Radushkevich (DR) model. With a few exceptions, the fit is found to be quite poor. However, a bimodal data distribution is consistently observed in DR plots of the remaining adsorbate-adsorbent pairs, and fitting the data to two separate DR models for each of the two different concentration ranges (or surface coverages) leads to acceptable correlations in most cases. This, in turn, yields two values of the characteristic adsorption energy, E_o , for each pair. Results are considered in light

of the volatility and polarity of the vapors, the structures of the adsorbents, and differences in the importance of adsorbate-adsorbent and adsorbate-adsorbate interaction strengths at different levels of surface coverage. The implications of these findings for the design of micropreconcentrators are considered.

Model Descriptions

The Modified Wheeler model has often been used to describe the breakthrough of VOCs in packed adsorbent beds as a function of the critical design and operating variables [24-25]. The most common mathematical form of the Wheeler Model is given in Equation 2.1:

$$V_b = \frac{W_e W_B}{C_0} \left[1 - \frac{\rho_B Q}{k_v W_B} \ln \left(\frac{C_0}{C_x} \right) \right] \quad (2.1)$$

where V_b is the breakthrough volume (L) evaluated at some predetermined fraction of the challenge concentration, W_e the equilibrium adsorption capacity (g/g), W_B is bed mass (g), C_0 is the challenge concentration (g/L), C_x is the concentration downstream from the bed at which V_b is evaluated (g/L), k_v is the kinetic rate coefficient (min^{-1}), ρ_B is the packed-bed density g/mL, and Q (L/min) is the volumetric flow rate. By convention, V_b is usually evaluated at the point in time where $C_x/C_0 = 0.1$.

In order to use the Wheeler Model in a predictive manner, it is necessary to obtain independent estimates of W_e (and k_v). Among the theoretical models developed to describe W_e , the DR model is perhaps the most popular [21]. It is presented in its linearized form in Equation 2.2:

$$\ln W_e = \ln(V_o \rho_L) - \left[\left(\frac{RT}{\beta E_o} \right) \ln \left(\frac{p_{sat}}{p} \right) \right]^2 \quad (2.2)$$

where V_o is the micropore volume (mL/g), ρ_L is the density of the adsorbate in its liquid form (g/mL), R is the ideal gas constant, T is temperature (K), β is an affinity coefficient, E_o is the so-called characteristic energy (kJ/mole), p is the partial pressure of the vapor to which the adsorbent is exposed, and p_{sat} is the saturation vapor pressure of the adsorbate at the temperature of the test. A plot of $\ln W_e/\rho_L$, which is an expression for the amount of vapor uptake in terms of its condensed volume, versus $\ln^2 p_{sat}/p$, which is inversely related to the vapor concentration, permits estimates of E_o and V_o from the slope and y-intercept, respectively (note: values of β are generally derived from published polarizability data; see below).

Among the useful features of the DR model is its portrayal of the adsorption capacity in terms of variables specific to the adsorbing vapor (ρ_L , p , p_{sat}), the adsorbent (V_o), and their interaction (βE_o). The affinity coefficient, β , is used as a rudimentary means of differentiating the inherent adsorbent affinity of one adsorbate from another. It is most commonly defined as the ratio of the polarizability of the vapor of interest to that of benzene, which serves as a reference vapor [26]. Accordingly, E_o values derived for all adsorbates from the regression analysis described above are effectively normalized to that of benzene, and it is assumed implicitly that polarizability differences, alone, account for the differences in the characteristic energy of adsorption among different adsorbates. This implies that E_o values derived from Equation 2.2 for all vapors should converge to

approximately the same value (i.e., that for benzene). A review of reports where multiple vapors were evaluated on the same adsorbent reveals that this is, at best, only approximately the case [21-23, 27, 29, 30].

The DR model was originally developed to describe the adsorption of gases and vapors on microporous carbons [31], and it has been used to describe adsorption on other microporous materials as well [32]. For materials such as the graphitized carbons examined here, which lack microporosity, the V_o term loses its physical meaning. The Dubinin-Radushkevich-Kaganer (DRK) model is a derivative of the original DR model that is often used to describe adsorption on nonporous solids:

$$N_a = N_{am}(DRK) \exp \left[- \left(\frac{RT}{\beta E_o} \right)^2 \ln \left(\frac{p}{p_{sat}} \right)^2 \right] \quad (2.3)$$

where N_a is the amount adsorbed (mmol/g) and N_{am-DRK} is the monolayer capacity (mmol/g). Thus, N_{am-DRK} replaces V_o and it is typically evaluated by extrapolation from data collected at vapor concentrations $> 0.1p_{sat}$, where the surface coverage starts to approach a full monolayer [20, 21]. For the current study, the concentrations and surface coverages are far below such levels, rendering the validity of any extrapolations less reliable. For this reason, and since our interest lies primarily in evaluating E_o and W_e values for the VOCs tested, we have elected to use the original DR expression (i.e., Equation 2.2) and to disregard the interpretation of the y-intercept.

Reported values of E_o for non-porous carbons derived from isotherm measurements via the DR model are typically in the range of 8-12 kJ/mole for permanent

gases and simple organic molecules [20-21, 30, 33]. These are much lower than those derived for simple organic molecules on microporous carbons (~19-30 kJ/mole), consistent with the notion that micropore-filling entails a greater interaction between adsorbate and adsorbent [33, 34].

Of particular interest in this study is the dependence of E_o on surface coverage, which would be manifested as a deviation from linearity when plotting the relevant quantities from Equation 2.2 [27]. Increases in the slope of the linearized DR plot at higher levels of surface coverage, corresponding to a reduction in E_o , are commonly reported and are rationalized as reflecting a net reduction in adsorption strength accompanying the approach of a full monolayer, as the available adsorption sites on the surface become increasingly occupied [4, 20, 21, 23, 27, 29]. This implies that the adsorbate-adsorbent interactions are replaced by adsorbate-adsorbate interactions and that E_o values reflect the corresponding change in adsorption energy. In many studies, there is a segment of the DR plot in the sub-monolayer region that is sufficiently linear over a sufficiently wide range to permit estimates of E_o from the slope. However, the strength of the correlation used to derive such estimates is often rather low [21, 28, 30, 33] and it has been noted that the determination of the range over which to extract the data for use in the DR model is often subjective [27].

For microporous adsorbents, changes in E_o have been ascribed to the breadth of the distribution of pore sizes and the consequent differences in vapor-adsorbate interaction strengths as pores of different sizes become filled. Accordingly, it was argued that the Dubinin-Astakov model (of which the DR model can be considered a special case), which allows for variations in the exponent of the second term on the right-hand-

side of Equation 2.2, is more appropriate for modeling microporous adsorbents with polydisperse pores [35, 36]. For non-microporous materials, such arguments do not apply, and a generally accepted rationale for differences in characteristic energies derived from DR models for such materials, particularly at very low surface coverage, has not yet emerged.

The data presented in this study were generated over lower vapor concentration ranges than previously reported and include numerous examples where the value of E_o derived from application of the DR model changes systematically over the ranges of concentration and surface coverage considered. An attempt is made to interpret the trends in the data on the basis of adsorbent-adsorbate and adsorbate-adsorbate interaction strengths. Questions are raised about the applicability of the DR model in light of these trends and the wide range of E_o values (i.e., 6-fold at low coverage) derived using the model. Results are considered in the practical context of using the DR model to assist in designing micro-scale preconcentrators for μ GC instrumentation.

Experimental Section

Materials

The vapors used as adsorbates are listed in Table 2-1 along with several relevant physical properties. Collectively, they span a vapor pressure range of $\sim 10^3$ torr and comprise vapors from nine functional-group classes. All compounds were obtained from Aldrich (Milwaukee, WI) at $\geq 99\%$ purity with the exception of d-limonene (97%), 1-hexanal and α -pinene (98%) and were used without further purification.

Samples of C-B (60/80 mesh; specific surface area of 100 m²/g) and C-X (60/80 mesh; specific surface area of 250 m²/g) were obtained from Supelco (Eighty-Four, PA) and sieved to isolate particles with nominal diameters in the range of 112-140 μm. The granules of these adsorbents are irregularly shaped. According to the manufacturer, C-B is non-porous and C-X lacks any microporosity but has mesopores (> 10 nm in diameter) whose collective specific volume is 0.62 cm³/g [37].

Isotherm Collection

For the applications of interest, vapor concentrations are expected to be quite low, so tests focused on concentrations within the range of 10 to 3,600 ppb v/v in air. Expressed in terms of the fraction of the saturation vapor pressure (p/p_{sat}), the concentrations are within the range of 1.7×10^{-7} to 1.2×10^{-3} among the vapors tested. For a given vapor, the concentration range tested spanned a range of ~30-fold to 170-fold and, typically, from 8 to 13 discrete concentrations were tested. Test vapor atmospheres were generated by passing clean, dry air through a fritted bubbler containing the pure liquid compound and diluting the saturated vapor stream with clean, dry air via calibrated mass flow controllers. One flow controller provided a rate of air up to 500 mL/min, with a second providing a flow rate of air up to 50 L/min. The flow rates were varied to achieve the range of concentrations of interest. Vapor concentrations were periodically verified by diverting a portion of the test atmosphere to a gas sampling valve/loop and into a by GC-FID (Model 6890, Agilent, Palo Alto, CA) that was previously independently calibrated by liquid injections.

Previous breakthrough tests with small packed beds of C-B indicate that it does not retain compounds very strongly with vapor pressures greater than about 30 torr [12, 13], in accordance with its relatively low specific surface area. Similar tests with C-X have shown that it retains compounds with vapor pressures as high as 95 torr quite effectively, consistent with its higher specific surface area and finite mesoporosity [13]. This information was used in decisions about which vapors to test on which adsorbents.

Vapor adsorption was measured with a thermogravimetric analyzer (TGA, Pyris 1, Perkin Elmer, Waltham, MA) whose tared sample pan was loaded with C-B or C-X samples weighing between 2 and 5 mg that were pre-conditioned *in situ* by heating under N₂ to 270-300°C for 4.5 hr. The test atmosphere of the vapor was passed through the chamber that houses the sample pan via stainless steel tubing at a flow rate of 0.090 L/min and vented back to the laboratory exhaust hood. For each isotherm, the sample was exposed to a series of discrete concentrations in increasing order, with ~30-60 minutes allowed for equilibration at each concentration. Each subsequent exposure series (isotherm) was preceded by purging with N₂ for ~60 min to eliminate any residual vapors from the system. In addition, after collecting data for each isotherm, the adsorbent sample was heated to 300°C under N₂ for 30 min to remove adsorbed vapors. For most vapor-adsorbent pairs, isotherms were determined in duplicate and the data pooled. The minimum mass change detectable by the instrument is ±0.1µg and the smallest mass change used for construction of the isotherms in this study was 0.3 µg (typically larger). For a 4-mg sample, this corresponds to a minimum measurable W_e value of 75 µg/g. The sample chamber was maintained at 26.6°C ± 0.06°C during vapor exposure. Isotherms of toluene on C-B were collected periodically over the course of the study as a quality

control measure, and the largest relative standard deviation around the average W_e value at a given concentration was 15% (typically < 10%). Isotherms were determined for 11 vapors on C-X and 12 vapors on C-B. Six vapors were tested on both adsorbents.

Results and Discussion

Isotherms

The majority of the 23 isotherms generated are concave toward the concentration axis. However, there are several exceptions or qualifications to this trend. For example, the isotherms for n-octane, d-limonene, and m-xylene on C-B, and for toluene on C-X are linear over a wide range, but deviate from linearity at low concentrations (see below). The isotherms for benzene and 1-butanol on C-B and for butyl acetate and 1-hexanal on C-X are concave down, but exhibit a plateau at moderate-to-high concentrations, beyond which there is no further increase in W_e . Those for butyl acetate on C-B and for 2-butanone and 1-hexanal on C-X have a step-like plateau segment at mid-range concentrations.

The isotherm for m-xylene on C-B (Figure 2-1a), as just mentioned, is linear over most of the range tested, but the W_e values at low concentrations (i.e., < 100 ppb) exhibit positive deviations from the trend observed at higher concentrations. This isotherm is representative of those for a subset of adsorbates exhibiting similar positive deviations at low concentrations on one or the other adsorbent. The isotherm for trichloroethylene on C-X (Figure 2-1b) exhibits the more typical concave-down shape. In this case, however, the W_e values at low concentrations (i.e., < 450 ppb) are smaller than would be expected

by extrapolation of the trend established at higher concentrations, which is also found for numerous vapors on one or the other adsorbent as well.

Since the value of W_e affects the breakthrough volume of an adsorbent-packed preconcentrator (*cf* Equation 2.1), it is useful to examine the range of W_e values in this data set. To this end, we arbitrarily chose as benchmarks the values of W_e at 50 ppb and 1,000 ppb for each adsorbate-adsorbent pair (evaluated, by interpolation or extrapolation, using the most accurate DR model) and have listed these in Tables 2-2 and 2-3 for C-B and C-X, respectively. Values on C-B range from 10 to 290 $\mu\text{g/g}$ at 50 ppb and from 260 to 2050 $\mu\text{g/g}$ at 1000 ppb, while those on C-X range from 17 to 1400 $\mu\text{g/g}$ at 50 ppb and from 300 to 7030 $\mu\text{g/g}$ at 1000 ppb. One important implication of these results in the context of the Wheeler Model is that the quantity W_e/C_o is not constant over this concentration range, meaning that extrapolation of W_e values determined at high concentrations down to lower concentrations will incur large errors in expected values of V_b . Both positive and negative deviations occur among the cases studied here.

W_e values for the less volatile adsorbates are generally larger than those for the more volatile adsorbates on a given adsorbent, and those on C-X are generally higher than those on C-B, consistent with the higher specific surface area and the mesoporosity of the former adsorbent. This is most clearly illustrated by comparing W_e values for the six adsorbates tested on both adsorbents (marked with asterisks in Table 2-2), for which the ratio of W_e on C-X to that on C-B ranges from 1.3 - 23 at the 1,000 ppb challenge concentration. Lower ratios are observed for the more polar vapors butyl acetate, 1-hexanal, and 1-butanol, reflecting their weak interactions with both adsorbents.

Benzene, trichloroethylene, 1-hexanal, and 1-butanol exhibit quite low W_e values on C-B even at 1,000 ppb (i.e., $< 500 \mu\text{g/g}$), apparently due either to their volatility or polarity, and all but trichloroethylene exhibit a plateau in W_e at high concentrations on one or the other adsorbent as a further indication of relatively weak interactions. Butyl acetate on C-B and 2-butanone on C-X also give very low W_e values and were noted above to give non-monotonic isotherms.

Characteristic energies from the DR model

Initial attempts to fit the isotherm data to Equation 2.2 entailed the regression of $\ln(W_e/\rho_L)$ values onto $(\ln p_{sat}/p)^2$ values. Among the 23 adsorbate-adsorbent pairs tested here, only four combinations could be fit to a single linear regression with an $r^2 > 0.95$ (i.e., toluene/C-B, perchloroethylene/C-B, 1-butanol/C-X, and benzene/C-X). The remaining data showed significant divergence from the expected linear behavior.

Figures 2-2a and b present the linearized DR plots for the isotherms in Figures 2-1a and 1b, respectively. Two linear regions are apparent, with the discontinuity occurring at a surface coverage of 0.36 and 4.1% for Figure 2-2a and b, respectively. Separate linear regressions of the data in each region led to very good fits to the model ($r^2 \geq 0.94$) for these two representative adsorbate-adsorbent pairs.

Evaluating E_o in each region of Figure 2-2a reveals that for the m-xylene/C-B combination, E_o in the low-coverage region is three times higher than E_o in the high-coverage region. In contrast, for the trichloroethylene/C-X combination (Figure 2-2b), the E_o value in the low-coverage region is about 1.7 times *lower* than that in high coverage region. Aside from the four exceptional combinations cited above, all of the adsorbate-adsorbent combinations followed one these two generally ~bi-linear trends.

For about half of these the low-coverage E_o value was higher than the high-coverage E_o value, while for the remaining half the opposite was true.

We refer to combinations that yield a higher E_o at low coverage as Group 1-B and 1-X (for C-B and C-X, respectively) and those yielding a higher E_o at higher coverage as Group 2-B and 2-X. The values of E_o determined by linear regression are presented along with the regression r^2 and the ratios of the E_o values for each pair at low and high coverage in Tables 2-2 and 2-3 for C-B and C-X, respectively. The fit of the data to two separate DR models (Equation 2.2) is generally quite good: the linear regression r^2 was ≥ 0.93 in all but 6 of the 44 cases and was ≥ 0.98 in 22 cases.

Among the exceptions are d-limonene/C-B in the low coverage range, and butyl acetate/C-B and 1-butanol/C-B in the high coverage range. For d-limonene, the regression is based on 4 data points one of which falls slightly below the linear trend line. For butyl acetate/C-B, as mentioned above, there was a plateau at the mid-range concentrations. To retain as many points as possible in the modeling, only the center point was omitted, leading to some deviation from linearity at the higher concentrations. For 1-butanol/C-B the isotherm reaches a plateau at high concentrations, which also produces a plateau at high concentrations in the DR plot. This, in turn, leads to the anomalously high value of E_o and low r^2 value. The E_o value for 1-butanol/C-B at high concentrations is therefore considered unreliable. Note that for 1-hexanal/C-B, the lowest two data points were found to be below the detection limit upon data work-up and so were omitted, leaving only two data points from which to estimate E_o from the DR plot, hence $r^2 = 1$.

For Group 1-B, the low-coverage E_o ranges from 10-23 kJ/mole, the high-

coverage E_o values range from 5-8 kJ/mole, and the ratios (high:low) range from 1.7 to 3.0 (Table 2-2). For Group 2-B, the low-coverage E_o values range from 6-17 kJ/mole and are from 1.2 to 4.8 times smaller than the high-coverage E_o values. The points at which the discontinuities occur in the linearized plots were estimated by interpolation and fall within in the range of 0.36 to 1.9% (16-44 nmole/m²; 2.0-8.7 nL/m²) and 0.46-4.1% (12-55 nmole/m²; 1.1-5.1 nL/m²) for Group 1-B and 1-X, respectively.

For adsorption on C-X, the same trends are observed as for C-B. For Group 1-X the low-coverage E_o values range from 11-39 kJ/mole and are from 1.3 to 4.5 times higher than the corresponding high-coverage E_o values. For Group 2-X the low-coverage E_o values range from 11-32 kJ/mole and are 1.5 to 4 times lower than the corresponding high-coverage E_o values. The points of discontinuity fall in the range of 0.29-1.9% (13-79 nmole/m²; 1.2-11 nL/m²) and 0.46-4.1% (27-190 nmole/m²; 2.5-17 nL/m²) for Group 1-X and Group 2-X, respectively, and are similar, though slightly higher on average, than those for the lower-surface area C-B.

Consistent with the higher specific surface area of C-X, the E_o values are generally higher than those on C-B for both regions [29]. The mesoporosity of this adsorbent may also contribute to higher characteristic energies. For the six vapors tested on both adsorbents, the low-coverage E_o values on C-X are consistently higher than those on C-B. In addition, those vapors in Group 2-X on C-X fall into Group 2-B on C-B, with the exception of benzene which is in Group 2-B but is linear on C-X.

Physical interpretation

Although the vapor concentration ranges over which measurements were

collected here are relatively narrow, the consistent observation of two distinct regions in the DR plots for the majority of adsorbates is noteworthy. Starting with Group 1-B, the E_o values for the low-coverage region range from the more-or-less typical values exhibited by n-decane and α -pinene to the relatively high values exhibited by n-octane and m-xylene. Regardless of the magnitude of this low-coverage E_o value, however, the reduction in E_o between low-coverage and high-coverage regions is about the same for all adsorbates, i.e., ~2-3 fold (Table 2-2). The point of discontinuity varies by about 5-fold. It is higher for the two alkanes, which is accordant with the ability of alkanes to pack more tightly on the adsorbent surface [29], lower for the aromatic m-xylene, accordant with the tendency for aromatics to lie flat on carbon surfaces and therefore not to pack as tightly, and mid-range for the branched cyclic α -pinene and d-limonene.

The most obvious explanation for the two regions with different apparent E_o values is that the C-B surface is energetically heterogeneous; higher-energy sites become filled preferentially at low coverage and give rise to higher values of E_o . Subsequent adsorption occurs at lower-energy sites, yielding correspondingly lower values of E_o . Although graphitization is known to reduce or eliminate such heterogeneity [38], the existence of a small fraction of residual high-energy sites on the C-B is not unreasonable. The low values of surface coverage at which the transition apparent occurs also lend support to this argument. The presence of high-energy sites would also account for why the values of E_o for C-B at low coverage are higher than expected for a non-porous graphitized carbon.

However, some of the trends among the values are puzzling. For example, to the extent that E_o values would be expected to track values of the heats of adsorption (Table

2-1), the value for n-decane should be larger than that for n-octane [34]. By the same token, the value for m-xylene should be higher than that for toluene, but the magnitude of the difference observed here (i.e., ~2-fold) is larger than can be accounted for on the basis of differences in the heats of adsorption alone. One might postulate that the larger values for n-octane and m-xylene reflect some sort of size/shape preference for these vapors relative to the larger or more branched α -pinene, d-limonene, and n-decane. Indeed, molecular-scale gaps created by dislocations in the surface of graphitized carbon blacks have been cited as possible causes of shape-selective vapor sorption at low coverage [39], but it is difficult to reconcile that the ratio of E_o values for n-octane and n-decane is ~2 while that for toluene and m-xylene is ~0.5.

For the Group 1-X vapors (Table 2-3), once again, several of the low-coverage E_o values derived from the DR model are higher than expected for a graphitized carbon. The ratios of high-to-low E_o values are slightly greater than those for the Group 1-B vapors (with the exception of 2-butanone), which can be ascribed to the higher surface area and mesoporosity of the C-X. The points of discontinuity occur at fractional coverages similar to those for the Group 1-B vapors, and that for n-heptane is higher than those for the aromatic and branched hydrocarbons, consistent with the packing trends observed with the Group 1-B vapors. Although the high-coverage E_o values for these vapors are larger, on average, than those for the high-coverage values of the Group 1-B vapors, they are within the range considered typical of vapors adsorbing on graphitized carbons [33]. Thus, these data also support the arguments presented above attributing the reduction in E_o values at higher coverage to surface-energy heterogeneity.

The increases in E_o values at high coverage for the Group 2-B vapors indicates

that additional interactions are involved. Nearly all of the Group 2-B vapors exhibit relatively small values of W_e in both regions of coverage, and several exhibit plateaus in their isotherms at higher concentrations. Included in this group are the two most volatile vapors tested on C-B (i.e., benzene and trichloroethylene) and the three most polar vapors tested on C-B (i.e., butyl acetate, 1-hexanal, and 1-butanol). Increases in volatility and polarity will tend to reduce the magnitude of adsorbate-adsorbent interactions at a given partial pressure and reduce the capacity of the adsorbent for an adsorbate. Indeed, all five of these vapors show very small breakthrough volumes when passed through a bed of C-B [13]. We note also that the points of discontinuity for benzene and trichloroethylene on C-B occur at very low levels of surface coverage (i.e., $\sim 0.4\%$) and that the slopes of the isotherms beyond this point are quite shallow for all Group 2-B adsorbates. At the same time, the low-coverage E_o values for the Group 2-B adsorbates are comparable to those of most of those in Group 1-B, indicating that, while the extent of uptake is low, the adsorbent-adsorbate interaction energies are similar.

The only explanation we can propose to account for the observed trend among the Group 2-B vapors is that, first, there are still high-energy surface sites available and, second, the high-coverage E_o values are increased by virtue of significant contributions from adsorbate-adsorbate interactions for these relatively poorly adsorbed vapors. For the polar vapors, this is supported by their relatively large heats of condensation (Table 2-1). For benzene and trichloroethylene it would seem to be a matter of the relative importance of adsorbent-adsorbate vs. adsorbate-adsorbate interactions, since their heats of condensation are relatively small. We cannot, however, rule out the possibility that the higher E_o values are merely artifacts rather than being physically meaningful; as noted

above, the high-coverage E_o value of 1-butanol is unrealistically high, and results from the nearly invariant values of W_e observed over the high-coverage range.

The DR plots for toluene and perchloroethylene on C-B are linear over the entire concentration range. These vapors are more volatile than those in Group 1-B, less volatile than benzene and trichloroethylene, and less polar than the Group 2-B compounds. Their E_o values are similar to each other and are comparable to the low-coverage E_o values for many of the other vapors tested. The W_e value at 1000 ppb is relatively small for toluene and comparable to those of the Group 1-B vapors for perchloroethylene. However, since perchloroethylene is about twice as dense in its condensed state as most hydrocarbons, the volume it occupies is proportionally smaller. The fractional coverage of perchloroethylene at 1000 ppb is 1.8% and that of toluene is 2.4%, which are relatively high values. Thus, it is possible that the toluene and perchloroethylene DR plots remain linear because not all of the high-energy sites on C-B are filled over the concentration range spanned in the tests for these two adsorbates. Alternatively, whatever reduction in E_o is expected on the basis of surface heterogeneity is made up for by adsorbate-adsorbate interactions to just enough of an extent to retain the same value of E_o in the high-coverage regions for these two adsorbates.

All four vapors in Group 2-X exhibit relatively large values of W_e at higher coverage, in comparison to the values observed for the same vapors on C-B (except n-hexane, which was not tested on C-B). The isotherms for the polar butyl acetate and 1-hexanal plateau at high concentrations, as seen with these vapors on C-B, and the thus larger E_o values at higher coverage could be attributed to an increase in adsorbate-adsorbate interactions. It is curious, however, that 2-butanone does not exhibit the same

behavior, given that it is not only more polar but also more volatile than butyl acetate. The increase in E_o for the volatile n-hexane can be rationalized by the same arguments raised in regard to benzene and trichloroethylene on C-B. Given the large W_e values for trichloroethylene on C-X and the similarity in the high-coverage E_o values for trichloroethylene on C-B and C-X, it is difficult to argue that the increase in E_o at high coverage arises from an increase in adsorbate-adsorbate interactions. Thus, we are at a loss to explain the behavior of trichloroethylene on C-X. For benzene and 1-butanol on C-X, arguments similar to those for toluene and perchloroethylene on C-B can be made to explain the constant value of E_o over the entire concentration range.

Practical implications

The primary implications of these results for the design of a micro-preconcentrator relate to predicting the amount of adsorbent material required for quantitative capture of vapors and, thereby, to the size of the device required to contain the adsorbent bed. One scenario considered in this context was that estimates of W_e would be derived at higher concentrations and extrapolated to lower concentrations. Given the dearth of data on adsorption at challenge concentrations in the low-ppb range, this seemed like a reasonable hypothetical case to consider. In the case of Group 1-X and 1-B vapors, using the DR model for the data at higher concentrations (high-coverage regions) to predict W_e at the lower concentrations consistently underestimates the measured values, with errors ranging from -11 to -88% (average = -64%) as shown in Tables 2-2 and 2-3. Although such estimates might be viewed as conservative because

they would insure sufficient capacity, as discussed above there is a cost in terms of power and injection band broadening to packing too much adsorbent material in the device.

For the Group 2-B and 2-X vapors a single-energy DR model derived from data at higher concentrations would overestimate W_e values at lower concentrations by 13-214% (Tables 2-2 and 2-3). This would lead to less mass than necessary being packed into the device, with the associated risks of early breakthrough and a negative bias in the analysis.

Improvements in the accuracy of W_e estimates are apparent from the errors shown when using the dual-region DR models, which range from 3-30% (avg = 7%). Of course, these projections must take into consideration the suitability of the adsorbent for the vapors of interest. As discussed above, for the vapors in Group 2-B and some of those in Group 2-X the W_e values are probably too small to expect sufficient breakthrough volumes for practical use.

Considered more generally, the predictive value of these DR models is called into question. For one thing, a separate model is required for each adsorbate -- values of E_o at low coverage span a 6-fold range and at high coverage span a 5-fold range (excluding 1-butanol on C-B). Theoretically, these E_o values should all be equivalent to that for benzene. This suggests either that the model is not applicable to estimating adsorption in the low concentration range examined here or that β does not capture all of the factors affecting the differential affinities for the adsorbent surface among these vapors. In any case, it is not possible, *a priori*, to select an appropriate value of E_o or to anticipate the direction and magnitude of the change of E_o with concentration or surface coverage. Although, in general, well-adsorbed vapors exhibited a reduction in E_o with increasing

coverage, the number of exceptions to this trend found in this data would render any predication moot.

Conclusions

This study has examined in detail the adsorption of multiple vapors on graphitized carbons in the context of the DR model at concentrations relevant to many environmental monitoring applications (i.e., ppb v/v). Systematic changes in the characteristic adsorption energy, E_o , as a function of challenge concentration (surface coverage) in this range were revealed in most of the cases considered. The observed trends in E_o values can be rationalized qualitatively as arising from differences in adsorption-site energies or the relative contributions of adsorbate-adsorbent vs. adsorbate-adsorbate interactions with surface coverage. However, mitigating factors that were identified include the volatility and polarity of the adsorbate, the extent of vapor uptake by the adsorbent as well as the shape of the isotherm. Satisfactory explanations for the observed trends were not possible in all cases.

From a practical standpoint, the results found here suggest that the utility of the DR model for predicting adsorption capacity is quite limited. The wide range of E_o values derived from the isotherms precludes the extrapolation of values to other vapors and the varying nature of the change in E_o with surface coverage precludes extrapolation outside of the measured concentration range.

Although compounds from several different functional groups classes spanning a fairly wide range of vapor pressures were examined here, the data set is finite and the trends observed raise questions that might be better addressed by a more systematic set of

test compounds, such as homologous alkanes, aromatics or oxygenates. Regardless, it would seem prudent to seek alternative models for the purposes of designing and predicting the performance of adsorbent micropreconcentrators for microanalytical system applications.

Table 2-1. Physical properties of the compounds tested as adsorbates.^a

Adsorbate	p_{sat} (torr)	β	ρ_L (g/cm ³)	ΔH_c (kJ/mol)	Adsorbent
n-hexane (HEX)	151	1.1	0.661	31.6	C-X
2-butanone (MEK)	95	0.79	0.800	34.8	C-X
benzene (BEN)	95	1.0	0.877	33.8	C-X, C-B
isooctane (IOC)	49	1.5	0.688	35.1	C-X
trichloroethylene (TCE)	47	0.97	1.46	34.5	C-X, C-B
n-heptane (HEP)	46	1.3	0.680	36.6	C-X
toluene (TOL)	28	1.2	0.867	38.0	C-X, C-B
2,5-dimethylfuran (DMF)	25	1.1	0.888	31.8	C-X
perchloroethylene (PCE)	18	1.2	1.62	39.7	C-B
n-octane (OCT)	14	1.5	0.699	41.5	C-B
butyl acetate (BAC)	12	1.2	0.883	43.9	C-X, C-B
1-hexanal (HXL)	11	1.1	0.834	42.5	C-X, C-B
m-xylene (XYL)	8.3	1.4	0.860	42.7	C-B
1-butanol (BOH)	6.7	0.84	0.810	52.4	C-X, C-B
α -pinene (PIN)	4.8	1.7	0.854	44.6	C-B
d-limonene (LIM)	2.0	1.7	0.841	39.4	C-B
n-decane (DEC)	1.4	1.8	0.727	51.4	C-B

^a p_{sat} : vapor pressure; β : affinity coefficient; ΔH_c : enthalpy of condensation [40-44].

Table 2-2. Results derived from fitting data for Carbo-pack B to the DR model.

Adsorbate	E_o (kJ/mole) ^a		ratio ^b	area (%)	discontinuity ^c mass, (µg/g)	W_e (µg/g) ^d		modeling error (%) ^f	
	low coverage	high coverage				50 ppb	1000 ppb	single DR	dual DR
<i>Group 1-B</i>									
OCT	19 (0.99)	8.5 (0.96)	2.3	2.4	490	290	1200	55	4.7
XYL	24 (0.94)	7.2 (0.99)	3.3	0.36	170	150	1100	87	2.5
PIN	11 (0.99)	6.5 (0.99)	1.7	1.3	460	150 ^e	1100	70	9.0
LIM	15 (0.88)	6.2 (0.99)	2.4	1.2	330	230	2100	11	2.4
DEC	10 (0.95)	5.3 (0.97)	1.8	3.1	630	290	1700	84	15
<i>Linear</i>									
PCE	10 (0.99)					76 ^e	1900	6.6	
TOL ^g	12 (0.99)					76 ^e	680	5.0	
<i>Group 2-B</i>									
BEN ^g	11 (0.97)	27 (0.95)	0.42	0.38	180	37 ^e	260	210	30
TCE ^g	8.2 (0.97)	19 (0.93)	0.42	0.35	160	38 ^e	300	170	8.2
BAC ^g	14 (0.96)	17 (0.87)	0.86	1.3	450	220 ^e	530	33	7.5
HXL ^g	8.1 (1.0) ^f	18 (0.98)	0.44	0.75	300	11 ^e	420	13	10
BOH ^g	17 (0.99)	83 (0.01)	0.21	0.64	400	43 ^e	400	84	3.7

^a r^2 values from the linear regressions used to calculate E_o values are shown in parentheses; ^bratio of low:high coverage E_o values; ^csurface coverage at the point of discontinuity between high- and low-coverage regions in terms of fractional surface area and mass; ^dadsorption capacity values determined at vapor concentrations of 50 ppb and 1000 ppb from the DR model; ^evalue determined by extrapolation from higher concentration; ^faverage absolute error in estimating W_e at low coverage using a single DR model derived from the high-coverage data or the dual DR model derived from the data at low coverage; ^gthese vapors were also tested on C-X.

Table 2-3. Results derived from fitting data for Carbo-pack X to the DR model.

Adsorbate	E_o (kJ/mole) ^a		ratio ^b	discontinuity ^c		W_e ($\mu\text{g/g}$) ^d			modeling error (%) ^f	
	low coverage	high coverage		area (%)	mass, ($\mu\text{g/g}$)	50 ppb	1000 ppb	single DR	dual DR	
<i>Group 1-X</i>										
MEK	16 (0.90)	12 (0.88)	1.3	0.29	240	32 ^e	310	88	10	
TOL	32 (0.99)	9.5 (0.99)	3.3	1.9	1800	1400	2800	59	3.3	
IOC	29 (0.94)	6.9 (0.97)	4.2	0.81	710	600	940	71	2.7	
HEP	14 (0.99)	7.5 (0.99)	1.8	2.3	1900	450 ^e	2600	73	5.7	
DMF	29 (0.99)	12 (0.98)	2.3	1.4	1200	420	5500	45	3.2	
<i>Linear</i>										
BEN	13 (0.98)					160 ^e	2700	8.1		
BOH	17 (0.99)					70 ^e	520	7.4		
<i>Group 2-X</i>										
HEX	12 (0.99)	20 (0.99)	0.58	1.3	930	220	1700	110	3.0	
TCE	14 (0.99)	23 (0.99)	0.61	4.1	6200	650 ^e	7000	100	4.0	
BAC	9.1 (0.98)	11 (0.93)	0.83	0.46	620	17 ^e	940	120	5.2	
HXL	12 (0.97)	19 (0.93)	0.67	1.2	1000	490	1600	37	6.5	

^a r^2 values from the linear regressions used to calculate E_o values are shown in parentheses; ^b ratio of low:high coverage E_o values; ^c surface coverage at the point of discontinuity between high- and low-coverage regions in terms of fractional surface area and mass; ^d adsorption capacity values determined at vapor concentrations of 50 ppb and 1000 ppb from the DR model; ^e value determined by extrapolation from higher concentration; ^f average absolute error in estimating W_e at low coverage using a single DR model derived

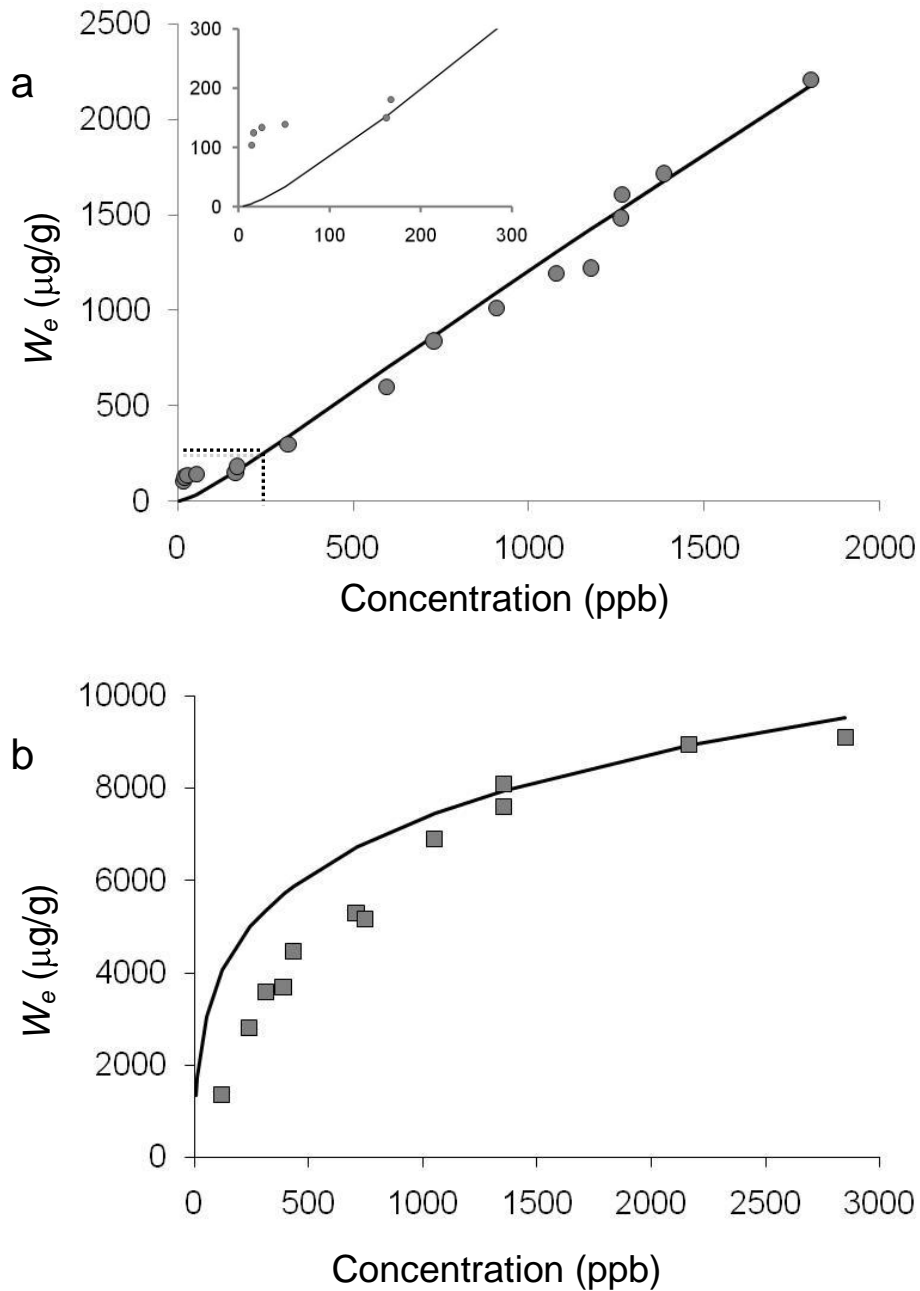


Figure 2-1. Representative adsorption isotherms of a) m-xylene on Carbopack B and b) trichloroethylene on Carbopack X. Solid lines derived from application of the single DR model of the data in the high-coverage range (see Tables 2-2 and 2-3). Inset in a) highlights the error in the low-coverage region for m-xylene.

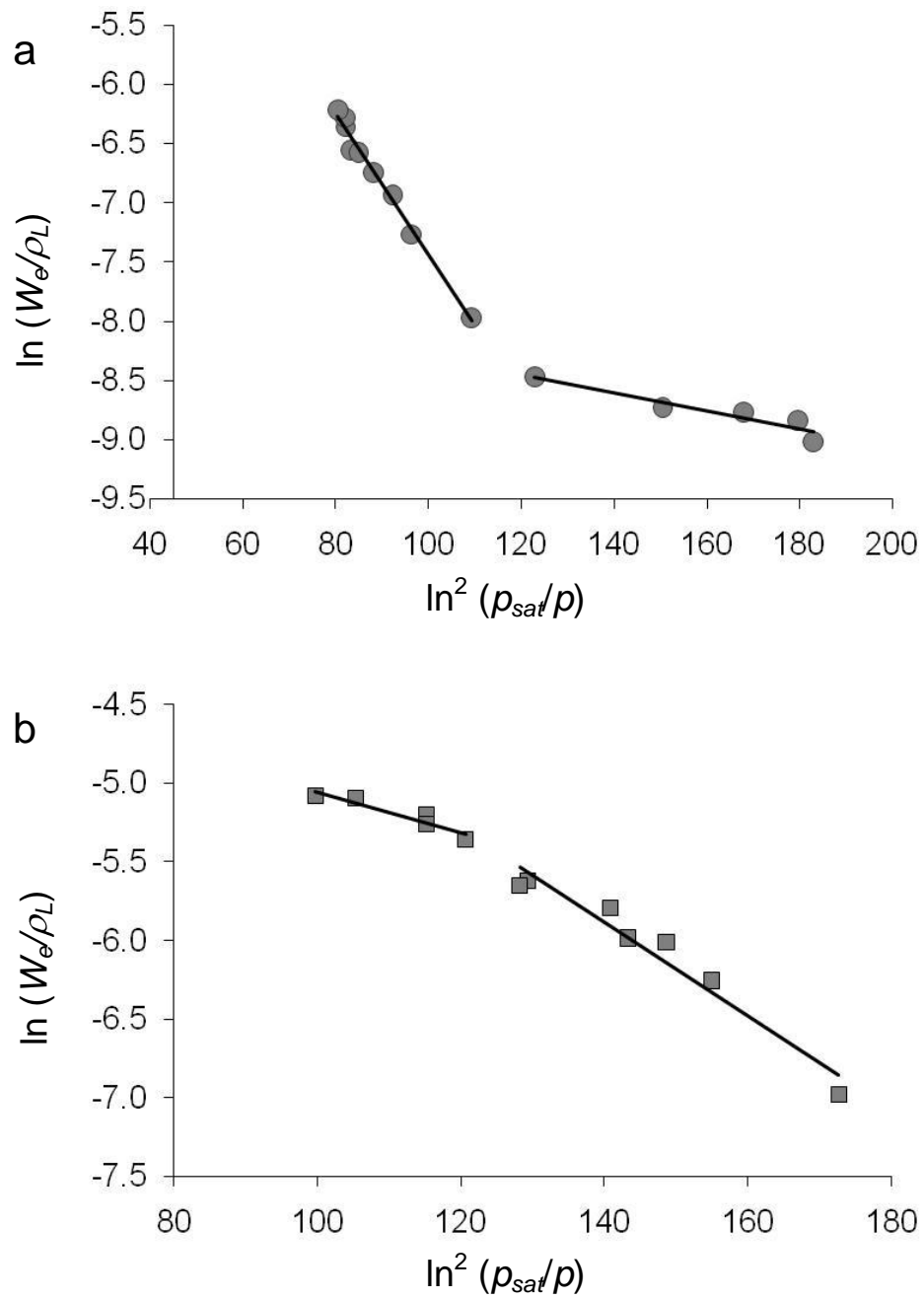


Figure 2-2. Linearized DR plots of a) m-xylene on Carbopack B and b) trichloroethylene on Carbopack X.

References

- [1] F. Bruner, P. Ciccioli, and F. Di Nardo, *J Chrom*, **1974**, 99, 661.
- [2] N. V. Kovaleva and K. D. Shcherbakova, *J Chrom*, **1990**, 520, 55.
- [3] F. Bruner, G. Bertoni, and P. Ciccioli, *J Chrom*, **1976**, 120, 307.
- [4] F. Bruner, G. Crescentini, F. Mangani, and L. Lattanzi, *J Chrom*, **1990**, 517, 123.
- [5] R. Leboda, A. Lodyga, and A. Giera, *Mater Chem Phys*, **1997**, 51, 216.
- [6] K. Dettmer and W. Engewald, *Anal Biochem*, **2002**, 373, 490.
- [7] A. R. Mastrogiamomo, E. Pierini, L. Sampaolo, *Chromatographia*, **2000**, 52, 345.
- [8] E. Matisova and S. Skrabakova, *J Chrom A*, **1995**, 707, 145.
- [9] US EPA, TO-17. *Compendium of methods for the determination of toxic organic compounds in ambient air*. Washington, DC, EPA/625/R-96/010b, **1997**.
- [10] W. C. Tian, S. W. Pang, C. -J. Lu, and E. T. Zellers, *J Microelectromech Sys*, **2003**, 12, 264.
- [11] W. C. Tian, H. K. L. Chan, C. -J. Lu, S. W. Pang, E. T. Zellers, *J Microelectromech Sys*, **2005**, 14, 498.
- [12] C. -J. Lu and E. T. Zellers, *Anal Chem*, **2001**, 73, 3449.
- [13] C. -J. Lu and E. T. Zellers, *Analyst*, **2002**, 127, 1061.
- [14] Q. Y. Zhong, R. A. Veeneman and W. H. Steinecker, C. R. Jia, S. A. Batterman, E. T. Zellers, *J Environ Monit*, **2007**, 9, 440.
- [15] C. -J. Lu, W. H. Steinecker, W. C. Tian, M. Agah, J. M. Potkay, M. C. Oborny, J. M. Nichols, M. Agah, J. A. Potkay, H. K. L. Chan, J. Driscoll, R. D. Sacks, K. D. Wise, S. W. Pang, and E. T. Zellers, *Lab on a Chip*, **2005**, 5, 1123.
- [16] C. -J. Lu, J. Whiting, R. D. Sacks and E. T. Zellers, *Anal Chem*, **2003**, 75, 1400.
- [17] W. A. Groves, E. T. Zellers, and G. C. Frye, *Anal Chim Acta*, **1998**, 371, 131.
- [18] Q. Y. Zhong, W. H. Steinecker, and E. T. Zellers, *Analyst*, **2008**, submitted.
- [19] F. Bruner, G. Crescentini, and F. Mangani, *Chromatographia*, **1990**, 30, 565.

- [20] P. J. M. Carrott, M. M. L. Ribeiro Carrott, I. P. P. Cansado, and J. M. V. Nabais, *Carbon*, **2000**, 38, 465.
- [21] D. Hugi-Cleary, S. Wermeille, and F. Stoeckli, *Chimia*, **2003**, 57, 611.
- [22] A. A. Isirikyan and A. V. Kiselev, *J Phys Chem*, **1961**, 65, 601.
- [23] P. J. M. Carrott, R. A. Roberts, and K. S. W. Sing, *Langmuir*, **1988**, 4, 740.
- [24] A. Wheeler and A. J. Robell, *Catalysis*, **1969**, 13, 299.
- [25] P. Lodewyckx, G. O. Wood, S. K. Ryu, *Carbon*, **2004**, 42, 1351.
- [26] K. E. Noll, D. Wang, T. Shen, *Carbon*, **1989**, 27, 239.
- [27] S. A. Dastgheib and T. Karanfil, *J Coll Inter Scie*, **2005**, 292, 312.
- [28] G. O. Wood, *Carbon*, **2001**, 39, 343.
- [29] F. Rouquerol, J. Rouquerol, K. Sing, *Adsorption by powders and porous solids*, Academic Press, Oval Road, London: **1999**.
- [30] A. Andreu, H. F. Stoeckli, and R. H. Bradley, *Carbon*, **2007**, 45, 1854.
- [31] F. Stoeckli, *Carbon*, **1998**, 36, 363.
- [32] G. O. Wood, *Carbon*, **1992**, 30, 593.
- [33] F. Stoeckli, A. Guillot, A. M. Slassi, and D. Hugi-Cleary, *Carbon*, **2002**, 40, 211.
- [34] N. N. Avgul and A. V. Kiselev, *Chemistry and Physics of Carbon*, P. L. Walker, Jr., Ed., Marcel Dekker, NY, 1970, in pp. 2-115.
- [35] P. Pendleton and C. Zettlemoyer, *J Coll Interface Scie*, **1984**, 98, 439.
- [36] H. F. Stoeckli, *J Coll Interface Scie*, **1977**, 59, 184.
- [37] D. Vitkuske, *The Reporter*, **2005**, 23.1, 3.
- [38] K. S. W. Sing, *Carbon*, **1994**, 7, 1311.
- [39] A. Derkaui, A. V. Kiselev, and B. V. Kuznetso, *J Chem Soc Fraaday Trans I*, **1985**, 81, 1685

- [40] D. R. Lide, editor. *Physical Constants of Organic Compounds*, in CRC Handbook of Chemistry and Physics. Internet Version 2007, (87th Edition), Taylor and Francis, Boca Raton, FL.
- [41] S. P. Verevkin, E. L. Kranykh, T. V. Vasiltsova, B. Koutek, J. Doubsky, and A. Heintz, *Flued Phase Equilibria*, 2003, 206, 331.
- [41] A. Hazra, D. Dollimore, and K. Alexander, *Thermochimica Acta*, **2002**, 392, 221.
- [43] S. P. Verevkin and F. W. Welle, *Structural Chemistry*, **1998**, 9, 215.
- [44] A. Xuwu, H. Riheng, W. Fu, W. Mali, and X. Yongkuang, *Acta Phys –Chim Sin*, **1987**, 3, 668.

Chapter 3

Kinetic Factors Affecting the Performance of a Microfabricated Vapor Preconcentrator

Introduction

The limited sensitivity and selectivity of stand-alone microsensors and microsensor arrays preclude their use for quantitative analysis of vapor mixtures at the low concentrations required for most occupational and environmental health, biomedical, and homeland security applications, where field determinations are of greatest value [1]. However, by integrating microsensor arrays with upstream components designed to preconcentrate and separate the components of vapor mixtures prior to detection, useful microsystems can be realized [1]. Prototype micro gas chromatographs (μ GC) incorporating such devices/modules have been shown capable of determining the components of mixtures of organic vapors at low concentrations [1-7].

Most vapor preconcentrators rely on partitioning of airborne VOCs between the air and a granular solid or a rubbery polymeric sorbent material deposited within the device. Vapors accumulate in, or on, the sorbent and are subsequently thermally desorbed into a smaller volume of air for detection by a downstream detector. If the quantity of the sorbent used is small, only a fraction of the mass of vapor(s) in the air sample passed through the device is captured. Assuming that sorption equilibrium is

established between the concentration of the vapor in the air and in(on) the sorbent and that the partition coefficient is constant, the mass retained in the sorbent will be proportional to the air concentration and quantitative analysis is possible with proper calibration [8]. With larger amounts of adsorbent material it is possible to remove the entire quantity of vapor(s) from the sample stream. The exhaustive trapping provided by the latter design leads to much higher preconcentration factors as long as the device can be heated rapidly enough to desorb the trapped vapors into a small volume [9-13].

In conventional applications of preconcentrators, relatively large adsorbent beds are employed and vapors are thermally desorbed onto a smaller adsorbent or cryogenic focusing device prior to analysis, typically by gas chromatography. This serves to reduce the width of the injected band, which is desirable for maximizing chromatographic separation of the mixture components. Since most miniaturized preconcentrators are implemented without downstream focusers, we prefer the term ‘preconcentrator/focuser’ (PCF) which highlights the dual function of such devices, as well as the tradeoffs required for optimizing performance [9-13].

The majority of reports on miniature and microfabricated vapor PCFs [9-27] describe devices that rely on equilibrium sorption [14-25]. This reflects a priority being placed on small size and rapid, low-power heating rather than high capacity. As a result, the preconcentration factors achieved are generally quite low, ranging from ~10-200. With the exception of the μ PCF described in [24, 25], details supporting the design features of these types of devices have not been reported, and none of the published studies examined the effects of operating variables such as the sampling flow rate and vapor concentration on performance.

Efforts in our laboratory to develop PCFs for multi-vapor analysis have focused exclusively on devices designed for exhaustive trapping, and include adsorbent-filled glass or metal capillaries (cPCF) with wrapped-wire heaters [10, 11, 26] and adsorbent-filled single- and multi-stage MEMS devices (μ PCF) relying on bulk heating [9, 12, 13]. Multi-stage PCFs capable of capturing and efficiently desorbing up to >40 vapors spanning a wide range of volatility have been developed that are capable of producing preconcentration factors >5000 [9, 10].

In devices designed for exhaustive trapping, the dynamic adsorbent-bed capacity is the performance criterion that governs the minimum size of the PCF. It is affected by both thermodynamic and kinetic factors. Thus, a certain minimum mass of adsorbent is required, which depends on the adsorbent type and the nature, number, and concentrations of vapors in the sample stream that are partitioning onto the adsorbent surface. In addition, the rates of mass transfer are important both in the uptake of vapors from the sample stream and the release of those vapors during thermal desorption. The dynamic capacity is typically determined by continuously drawing a sample of vapor in air through the PCF and monitoring downstream for the appearance of breakthrough. The breakthrough volume, V_{b-x} , or the breakthrough time, t_{b-x} , is used as the measure of dynamic capacity and is defined as the volume (or time) required to observe some pre-set fraction, x , of the inlet vapor concentration (e.g., 10%) downstream from the PCF.

Model Descriptions

In all of our previous studies, we have used the modified Wheeler Model as a guide for designing our devices and assessing their performance. This model relates

several important PCF design and performance parameters to the V_b or t_b of a granular adsorbent bed under a continuous vapor challenge [10, 28, 29]:

$$V_b = \frac{W_e W_b}{C_o} \left[1 - \frac{1}{k_v \tau} \ln\left(\frac{C_o}{C_x}\right) \right] \quad (3.1)$$

$$t_b = \frac{\rho_b W_e}{\varepsilon C_o} \left[\tau - \frac{1}{k_v} \ln\left(\frac{C_o}{C_x}\right) \right] \quad (3.2)$$

where V_b is in liters, t_b is in minutes, W_e is the (kinetic) adsorption capacity (adsorbate mass/adsorbent mass), W_b is the packed-bed mass (g), $\tau = \varepsilon W_b / (\rho_b Q)$ is the bed residence time (min), ε is interparticle porosity, ρ_b is the adsorbent bed density, Q is the volumetric flow rate (cm^3/min), k_v is the kinetic rate constant (min^{-1}), C_o is the inlet concentration (g/cm^3), and C_x is the outlet concentration (g/cm^3).

This model predicts a non-linear decrease in V_{b-x} and a linear decrease in t_{b-x} with decreasing τ . The critical bed residence time, τ_c , corresponding to the point where V_{b-x} (or t_{b-x}) = 0, represents the theoretical limit to miniaturization of the PCF. That is, for a given value of Q , this defines the minimum volume of the PCF: when $\tau = \tau_c$ some fractional breakthrough will occur immediately after sampling and quantitative analysis is compromised. By the same token, for given PCF size, this determines the maximum flow rate, Q_c .

The quantity $W_e W_b / C_o$ is the volume of air, V_i , containing the vapor at C_o that is required to achieve thermodynamic equilibrium of the vapor between the air and the adsorbent. Since the adsorption efficiency, $1 - [\ln(C_o/C_x)/k_v \tau]$, is generally ≤ 1 , V_b is

generally $\leq V_t$. The quantity $\ln(C_o/C_x)/k_v\tau$ represents the fractional unused bed capacity. The apparent decrease in V_b as C_o increases is partially offset by an increase in W_e with C_o , which is often assumed to be proportional at low concentrations but is not necessarily so [30].

The effect on performance of operating at different values of Q and τ can be considered in light of Equations 3.1 and 3.2. Increasing Q leads to a proportional decrease in the instrument duty cycle (sampling duration), which is desirable. But this also leads to a decrease in τ and in the efficiency of adsorption, causing a decrease in V_b . For high Q values (approaching τ_c), the V_b decreases sharply with increasing Q . As Q is reduced, the bed becomes more efficient and V_b becomes less dependent on Q , asymptotically approaching a limiting value corresponding to V_t . Increasing W_b at a specific value of Q leads to a proportional increase in τ and a similar approach of V_b to V_t .

Applying Equations 3.1 or 3.2 for predicting performance requires determinations of the variables W_e and k_v for a given adsorbent-vapor pair. The former can be determined as a function of vapor concentration by gravimetric methods [35] or by running a series of breakthrough tests at different bed masses or flow rates. The latter variable is more difficult to determine because it depends on the dynamics of mass transfer within the adsorbent bed [29, 31-35]. Since k_v has no theoretical definition it must be determined empirically. Authors have examined k_v as a function of linear velocity, v_L (cm/sec) and particle diameter, d_p (cm), resulting in an empirical correlation for k_v :

$$k_v = 13.3\beta^{0.33}v_L^{0.7}d_p^{-1.5}\left(\frac{W_e}{MW}\right)^{0.5} \text{ sec}^{-1} \quad (3.3)$$

where β is the affinity coefficient of the Dubinin Radushkevich Isotherm model (given as a ratio of the molar polarizability of the analyte to the molar polarizability of a reference, benzene) and MW is the molecular weight (g/mole) [35]. The coefficient is purely empirical with no theoretical dependence [35]. Once k_v and W_e are determined, the effects of changes in Q (or τ) can then be determined.

Obviously, increasing the mass of adsorbent and/or decreasing the flow rate maximizes the breakthrough volume. However, increasing the adsorbent mass increases the pressure drop across the bed and may also increase the desorption bandwidth due to heat transfer limitations, increased dead volume, and residual adsorptive interactions of desorbing vapors as they are swept through the bed. Increasing the cross sectional area of the bed at constant W_b can reduce the pressure drop significantly [36], with no effect on τ or V_b . This, in turn, may allow a higher Q to be attained with a miniature pump, but, as discussed above, increases in Q will decrease V_b and t_b .

In an extension of the work of Lu et al. [10, 11] and Tian et al. [9, 12] this article describes the first systematic study of the effect of flow rate on the dynamic retention capacity of a μ PCF packed with a commercial graphitized carbon, Carbopack X (C-X). The μ PCF is challenged with two vapors that span the useful range of retention capacity for the adsorbent [11]. The vapor concentrations tested are an order of magnitude lower than those tested in previous studies and, therefore, are more relevant to those expected in most potential applications. An emphasis is placed on examining bed residence times approaching critical values. A conventional capillary PCF (cPCF) containing the same adsorbent material is tested in parallel. Empirical models of the k_v are derived and assessed for both devices and both vapors. Modeled values of k_v are combined with

independent estimates of W_e for the purposes of comparing experimental values of V_{b-10} to those determined using the modified Wheeler Model.

Experimental

Devices and Materials

The upper and lower sections of the μ PCF were fabricated from separate double-polished Si wafers. Deep-reactive-ion-etching (DRIE) was used to form 3 rectangular cavities in the lower section of the device to accommodate up to 3 different adsorbent materials. A Ti/Pt resistive temperature device (RTD) was evaporated onto the backside of this lower section. The upper section serves to cap the device and has two circular DRIE ports at each end that accept fused-silica capillaries for connection to upstream and downstream components. After the addition of adsorbent material to the lower section (see below), the two sections were sealed by Au-Au thermal-compression bonding at 400 °C. Details of device fabrication have been published elsewhere [13].

The overall dimensions of the μ PCF are 11mm \times 4mm \times 1mm. Each cavity is 2.58 mm wide and 450 μ m deep (cross sectional area = 0.0116 cm²). The lengths of the cavities were intentionally varied to accommodate different quantities of adsorbent materials having different specific surface areas for the purposes of preconcentrating vapors spanning a wide range of vapor pressures – the masses and corresponding cavity volumes were determined by extrapolation from a series of experimental measurements described in [9, 11]. Thus, the cavity lengths are 4.3, 2.4, and 1.6 mm, respectively, and the corresponding cavity volumes are 4.4, 2.5, and 1.6 mm³, respectively (Figure 3-1a).

In order to characterize an adsorbent material it must be tested individually with

individual vapors. Among the adsorbents we have found useful in previous studies is Carbopack X (C-X), which is a graphitized carbon available commercially as an irregularly shaped granular solid in different mesh sizes (Supelco, Bellefonte, PA). It exhibits excellent thermal stability and it efficiently captures and subsequently releases organic vapors of moderate polarity with vapor pressures in the range of ~28 to 95 torr [10, 11]. For this study, the first cavity of the μ PCF was charged with a sample of 1.33 mg of C-X (60/80 mesh) that had been passed through a series of sieves to isolate the fraction with nominal diameters in the range of 63-112 μ m (avg. = 87 μ m). In order to avoid problems arising from static charge accumulation, the pre-weighed sample of C-X was suspended in isopropanol and transferred to the μ PCF cavity by syringe. After allowing the solvent to evaporate the upper and lower sections of the μ PCF were sealed as described above [9]. Fused silica capillaries (430 μ m o.d., 320 mm i.d.) were attached in the flow ports with three layers of polyimide sealing resin.

The μ PCF was inverted and mounted in a 16-pin hybrid carrier package (Figure 3-1b). Connections to the heater pads on the device were made with soldered wire and four connections to the RTD were made with Al wire bonds. Holes drilled through the floor of the package accommodated the fused silica inlet/outlet capillaries emanating from the device. For mechanical support each capillary was epoxied to the package, and a 1 mm thermal isolation gap maintained between the device and the package.

The cPCF was constructed by packing a 5-cm section of thin-wall Inconel (1.59-mm o.d., 1.35-mm i.d., cross sectional area = 0.01431 cm²) with 1.35 mg of C-X that had been passed through sieves to isolate the fraction with nominal diameters in the range of 112-140 μ m (note: the fraction used was inadvertently larger than that used in

the μ PCF). The adsorbent was drawn into the tubing under vacuum and was retained in place by small pieces of stainless steel mesh and silanized glass wool [10, 11]. The bed occupied a length of \sim 4 mm and was located within 1-cm of the distal end of the tubing to minimize the downstream dead volume. A thin sleeve of polyimide (Microlumen, Tampa, FL) was placed around the packed section of the tube and a fine-wire type-K thermocouple was placed against the tube and held in place with another thin polyimide sleeve. A length of varnished Cu wire, used to resistively heat the adsorbent bed following each test, was then coiled tightly around this assembly to create a heated length that extended beyond the length of the adsorbent bed (Figure 3-1c).

Breakthrough Testing

Test atmospheres containing 110 ppb of either benzene or toluene in clean, dry air were created in 10-L Tedlar bags by serial dilution. Breakthrough volumes were determined by drawing the challenge concentration through the preconcentrator using a vacuum pump (UN86KTDC, KNF Neuberger, Trenton, NJ). A charcoal scrubber was placed in-line to protect the pump from vapors. At 1-min intervals an aliquot of the outlet stream was directed into a GC with flame-ionization detector (GC-FID, Model 6890, Agilent Technologies, Palo Alto, CA) via a six-port valve equipped with a 250- μ L gas sampling loop. The flow rate was measured, using a primary flow standard, and a rotameter was adjusted to achieve the desired flow rate. The column oven temperature was adjusted to give a retention time of 0.5-0.8 min. Peak integration was performed at the conclusion of each experiment using GRAMS32 (Version 6.0- Thermo-Scientific, Pittsburg, PA).

Breakthrough curves (C_x/C_o vs. volume) were generated in duplicate for Q and τ values ranging from 4-28 mL/min and 5-35 msec, respectively. Values of t_{b-10} and V_{b-10} were determined at $C_x/C_o = 0.1$ directly or by (linear) interpolation between the two nearest data points. The flow rate was measured at the end of every breakthrough curve with a soap bubble flow meter and the challenge concentration was measured prior to and at the end of every breakthrough determination. Concentrations were verified by comparison of FID peak areas to those generated by injection of a series of benzene and toluene solution standards generated in CS_2 that spanned the range of injection masses covered during the breakthrough tests. The preconcentrators were preconditioned by heating under N_2 for four hours at $200^\circ C$. Subsequently, after each experiment the adsorbent was regenerated under a flow of N_2 of ~ 20 mL/min by heating the device under test to $200-300^\circ C$ for 30 min to desorb the vapor.

Results and Discussion

Breakthrough Volumes

Figure 3-2 presents breakthrough curves for benzene and toluene measured at two different sample flow rates with the cPCF. The shapes are typical, with a relatively gradual initial increase in C_x at the smaller sample volumes (less than V_{b-10}) followed by a rapid rise in C_x and then a gradual approach to C_o . The V_{b-10} values at all flow rates are significantly smaller for benzene than for toluene. As discussed below, this is because the W_e and k_v values for benzene are both lower than those for toluene (Table 3-1). The selection of these two vapors, as mentioned in the Experimental Section, was made on the basis of previous test results that showed benzene to be one of the most volatile vapors

for which C-X exhibits a practically useful retention capacity and that toluene is one of the least volatile vapors retained by C-X that can also be released with high efficiency upon thermal desorption [11].

Over the range of flow rates examined the V_{b-10} (and t_{b-10}) values span a 5-fold and 7-fold range for benzene and toluene, respectively, with the cPCF. Similar ranges of V_{b-10} (and t_{b-10}) are spanned for these vapors with the μ PCF, although the values of V_{b-10} (and t_{b-10}) at a given flow rate are consistently lower for the μ PCF, as illustrated by the representative data in Figure 3-3. This relationship holds for all flow rates tested and reflects the longer bed residence time, at a given flow rate, for the cPCF. This, in turn, reflects the lower packing density and larger interparticle volume in the cPCF. Replicate determinations of V_{b-10} gave relative standard deviations of $< 15\%$ in all cases ($n = 2-5$). Thus, despite being packed with nearly identical masses of C-X, the dynamic retention capacity of these two devices as a function of flow rate differs.

Figure 3-4 presents the dependence of the breakthrough time on the bed residence time for both vapors on both devices. As shown, the t_{b-10} values for both vapors vary in direct proportion ($r^2 > 0.93$) to τ for both devices, consistent with Equation 3.2. The slopes of the lines in Figure 3-4 are expected to differ between devices and between vapors because the relationship between τ and t_{b-10} depends on vapor-specific variables (i.e., W_e and C_o) as well as device-specific variables (i.e., ρ_b and ε) (note, however, that for this study differences in C_o for a given vapor are expected to be $< 5\%$, which reflects the precision with which replicate test atmospheres could be produced).

Estimates of the kinetic W_e values (W_{e-k}) derived from the slopes of the lines in Figure 3-4 are 3-fold and 12-fold smaller than the thermodynamic W_e values (W_{e-th}) for

toluene and benzene, respectively, as shown in Table 3-1. These differences can be explained by the low efficiency of the bed over the range of flow rates examined. Substituting the values of W_{e-th} together with experimental V_{b-10} values into Equation 3.1 permits the determination of the range of adsorption efficiencies over the range of flow rates tested. The maximum efficiency values listed in Table 3-1, evaluated at the lowest flow rate (longest τ), are approximately 40% for toluene and 10% for benzene and reflect the fraction of the total retention capacity actually being used. The low values are consistent with the fact that testing was conducted over a range of t values that are within a factor of 10 of τ_c (see below). The much lower efficiency range for benzene relative to toluene can be ascribed to its lower k_v values in both devices. The k_v values listed in Table 3-1 were evaluated at $\tau=50$ msec via Equation 3.1 (using W_{e-th}) and show that the ratio of k_v for toluene to that for benzene ranges from 1.4-1.7, which is sufficient to account for the ~4.5-fold difference in efficiencies for the two vapors on both devices. The combination of a lower W_{e-k} and lower k_v is what causes the V_{b-10} and t_{b-10} values for benzene to be so much lower than those for toluene.

The x-axis intercepts in Figures 3-4 give the values of τ_c listed in Table 3-1. With the μ PCF, τ_c is 7-9 msec for both vapors, which corresponds to $Q_c = 12-16$ mL/min. With the cPCF, τ_c is 4-5 msec for both vapors ($Q_c = 35-40$ mL/min). The difference in τ_c between devices arises from the differences in packing density and interstitial volume, despite the similar bed masses used. The Q_c values represent the upper limits on the sampling flow rate that can be tolerated without risk of immediate breakthrough. As discussed below, operation well below these values is advisable to reduce the dependence of V_{b-10} on Q .

This is apparent by reference to Figure 3-5, which shows the relationship between τ and V_{b-10} . As shown, as τ approaches τ_c the rate of change in V_{b-10} increases sharply. For toluene with the μ PCF, for example, below $\tau \cong 15$ msec ($Q > 5$ mL/min), a 50% decrease in τ results in about a 40% decrease in V_{b-10} , while at longer τ values a 50% decrease in t results in only about a 15% decrease in V_{b-10} . A similar, though somewhat less sharp dependence of V_{b-10} on τ is observed with benzene (Figure 3-5b). These curves illustrate quite clearly the tradeoff between sampling rate and dynamic retention capacity with small adsorbent-packed preconcentrators that rely on exhaustive trapping.

Device Modeling

In order to use the Wheeler model for predicting device performance, it is necessary to have independent estimates of W_e and k_v . Values of W_{e-th} can be obtained from gravimetric measurements at the concentrations of interest. The empirical model represented by Equation 3.3 was explored in an attempt to derive a means of estimating k_v . Experimental values of k_v were calculated from Wheeler model (Equation 3.1) over the range of flow rates (bed residence times). As shown in Equation 3.3, k_v is dependent on linear velocity, particle diameter, W_e , the affinity coefficient from the Dubinin-Radushkevich isotherm equation, and molecular weight. By plotting the values of k_v vs. v_L , the data can be fit to a power regression of the form $k_v = m v_L^n$, where

$$m = C\beta^{0.33}d_p^{-1.5}\left(\frac{W_e}{MW}\right)^{0.5} \quad (3.4)$$

where C is a fitting parameter. From the regressions for toluene, the following two equations give the best fit for the cPCF and μ PCF, respectively:

$$k_v = 4.3\beta^{0.33} d_p^{-1.5} v_L^{0.85} \left(\frac{W_e}{MW} \right)^{0.5} \quad (3.5a)$$

$$k_v = 3.1\beta^{0.33} d_p^{-1.5} v_L^{0.74} \left(\frac{W_e}{MW} \right)^{0.5} \quad (3.5b)$$

Similarly, for benzene the following two equations give the best fit for the cPCF and μ PCF, respectively:

$$k_v = 3.5\beta^{0.33} d_p^{-1.5} v_L^{0.97} \left(\frac{W_e}{MW} \right)^{0.5} \quad (3.6a)$$

$$k_v = 2.2\beta^{0.33} d_p^{-1.5} v_L^{0.97} \left(\frac{W_e}{MW} \right)^{0.5} \quad (3.6b)$$

The regressions for toluene and benzene yielded r^2 values of >0.97 for both devices. Attempts to merge these data across vapors or devices led to regression models with r^2 values < 0.9 , which did not permit accurate enough estimates of k_v . Thus, while both devices and both vapors could be fit to empirical models having the same form as that found in the work of Wood and Lodewyckx [35], the form of the model is not as general as suggested by their work. For toluene, we observed larger k_v values and a larger

exponent for the linear velocity for the μ PCF. Rehrmann and Jonas made a similar observation with devices containing smaller particle diameters, that is to say that smaller particle diameters lead to smaller linear velocity dependencies (smaller exponents) [25]. Since the μ PCF has a smaller particle diameter than the cPCF, even though the particle diameter is accounted for in Equation 3.6 and 3.7, the effect is still seen in the linear velocity term. The difference in exponents, that is, $v_L^{0.74}$ for the μ PCF vs. $v_L^{0.85}$ for the cPCF precludes the use of a single equation for modeling.

For benzene, the differences in breakthrough volume result in different equations of k_v . When examining V_{b-10} vs. τ , there are much larger differences between the μ PCF and the cPCF. In fact, the values of V_{b-10} for the μ PCF are nearly two-fold smaller. We hypothesize that the adsorbent may have shifted by this point in the study and that some channeling of flow may have occurred in these tests. Since the breakthrough volumes for the μ PCF are so much lower than those for the cPCF, the resulting equation has a lower coefficient, C .

Unlike toluene, similar dependences on v_L are observed for benzene with the two devices, despite the differences in particle diameter. In fact, benzene has a more nearly linear dependence on velocity. This may be an artifact of having spanned a shorter range of linear velocities. Rather than ranging from 10-60 cm/sec, as the case with toluene, the velocity ranges from 10-40 cm/sec for benzene. The smaller values of V_{b-10} and W_e correspond to an increase in the significance of the first term of Equation 3.1 in the calculation of V_b [27]. Determination of V_b from the Wheeler model is achieved by subtracting the k_v term from the W_e term (Equation 3.1). Since benzene has smaller values of W_e , a smaller first term ($W_e W_b / C_o$) results. Because of this, when the second

term, containing l/k_v is subtracted, a larger change is observed when compared to subtracting the same l/k_v term from a first term that is nearly four times larger, as the case with toluene. With benzene, a 25% increase in k_v results in a 13% decrease in V_b . On the other hand, with toluene, a 25% increase in k_v results in only a 7% decrease in V_b , nearly half that of benzene. This shows that the same change in k_v between benzene and toluene lead to larger differences in V_b , which in turn makes benzene more sensitive to the k_v calculations.

Using the equations for k_v , Wheeler model descriptions were determined for both vapors and both devices. The results are shown as the solid lines in Figure 3-5a and b. Since a separate equation was used for each vapor and each device a nearly perfect fit is obtained.

Conclusions

With longer bed residence times, the breakthrough volume shows less dependence on changing bed residence times (flow rates) and becomes nearly independent of bed residence times if they are long enough. However, at bed residence times shorter than 15 msec, an increased dependence on bed residence time is observed. In this region, quantitative trapping can still be achieved, but small changes in flow rate can greatly impact the resulting breakthrough volume. At the extreme, the critical bed residence time is approached as which point breakthrough occurs immediately. If operation with flow rates at or beyond this point is desired, additional adsorbent mass is required to achieve trapping. In this instance, the additional mass would require additional power to thermally desorb the trapped vapors. Also, the extra mass is likely to increase the

injection band resulting from desorption and will negatively impact the ultimate separation and detection of trapped vapors. Additionally, including extra mass in a μ PCF is likely to require a re-design of the devices, which, for microfabricated devices can be costly. Therefore it is not recommended to exceed the critical bed residence time.

As bed residence times decrease, the efficiency of the adsorbent bed decreases. While both devices lack efficiency overall, the decrease in efficiency as bed residence decrease is still apparent. The efficiency of toluene adsorption is highest (nearest 100%) at the longest bed residence times and was found to be 42%. However, near the critical bed residence time, the efficiency drops to 5%. Likewise the efficiency of benzene adsorption is highest, 10%, for the longest bed residence times, but drops to 3% near the critical bed residence time. This further demonstrates that operating at higher flow rates (shorter bed residence times) decreases the efficiency of the adsorbent bed. Typically, when designing μ PCFs for use in microanalytical instruments, the maximum flow rate obtainable is desired to maximize the sample volume while minimizing the time it take to collect the given sample. However, as just described, the maximum flow rate is not necessarily the ideal case since the efficiency decreases as flow rate increases, dropping to zero at the extreme.

Ideally, a single equation of k_v would fit both devices and both vapors. However, due to the sensitivity of benzene V_b to calculations of k_v , this was not a viable option. When a single equation for both vapors was used to describe the Wheeler model curve, errors were in excess of 75% for benzene. This means that using the Wheeler model to predict breakthrough volumes for untested vapors is not feasible as originally hoped because a different equation for k_v is required for each vapor. In order to predict

breakthrough volumes, values of W_e and k_v must still be determined independently, which still involves an array of breakthrough volume determinations.

Additionally, when using the linearized Wheeler model to determine W_e from a series of breakthrough volume determinations, the result is not as reliable as when W_e is determined gravimetrically. While toluene revealed errors of only 10%, benzene estimations from the Wheeler model yielded errors in excess of 70%. The vast difference in errors between two demonstrate the unreliability of W_e determinations from the Wheeler model alone. Therefore, when using the Wheeler model for breakthrough volume predictions, it is not recommended that the linear Wheeler model be used to determine W_e values.

Wheeler model description were found for all four cases, but with errors of 5-18%. At longer bed residence times, a 20% error may not impact the breakthrough volume as much, since a 50% increase in flow rate results in only a 10-20% decrease in breakthrough volume, but a 20% error at flow rates near the critical bed residence times can lead to significant decreases in adsorbent bed efficiency and non-quantitative trapping, since in that region, the same 50% increase in flow rate results in nearly a 50% decrease in breakthrough volume. Operation in this range of flow rates should be avoided to maximize the efficiency of the preconcentrator .

Table 3-1. Values of relevant variables and performance metrics of the μ PCF and cPCF.

Vapor/device	W_{e-th}^a ($\mu\text{g/g}$)	W_{e-k}^b ($\mu\text{g/g}$)	W_{e-th}/W_{e-k} ---	τ_c^c (msec)	Q_c (mL/min)	Efficiency ^d (%)	k_v^e (sec^{-1})	Model Deviation ^f (%)
Toluene cPCF	1500	580	2.7	4	40	36	73	12
μ PCF	1500	520	2.9	7	16	44	81	20
Benzene cPCF	410	33	12	5	35	12	50	11
μ PCF	410	31	12	9	12	7.9	48	23

^aThermodynamic W_e value were determined gravimetrically (see Chapter 3); ^b Kinetic W_e value determined from the slopes of the plots in Figure 3-4 via Equation 3.2; ^ccritical bed residence time obtained from the x-intercept of Figure 3-4; ^dMaximum efficiency calculated at 49 and 51 msec for the cPCF and μ PCF with toluene, respectively, and 50 (extrapolated from Equation 3.6a) and 52 msec for the cPCF and μ PCF with benzene, respectively; ^e k_v values corresponding to the maximum efficiency; ^fAbsolute errors from comparison V_{b-10} values determined from the Wheeler model correlation and experimentally determined V_{b-10} values.

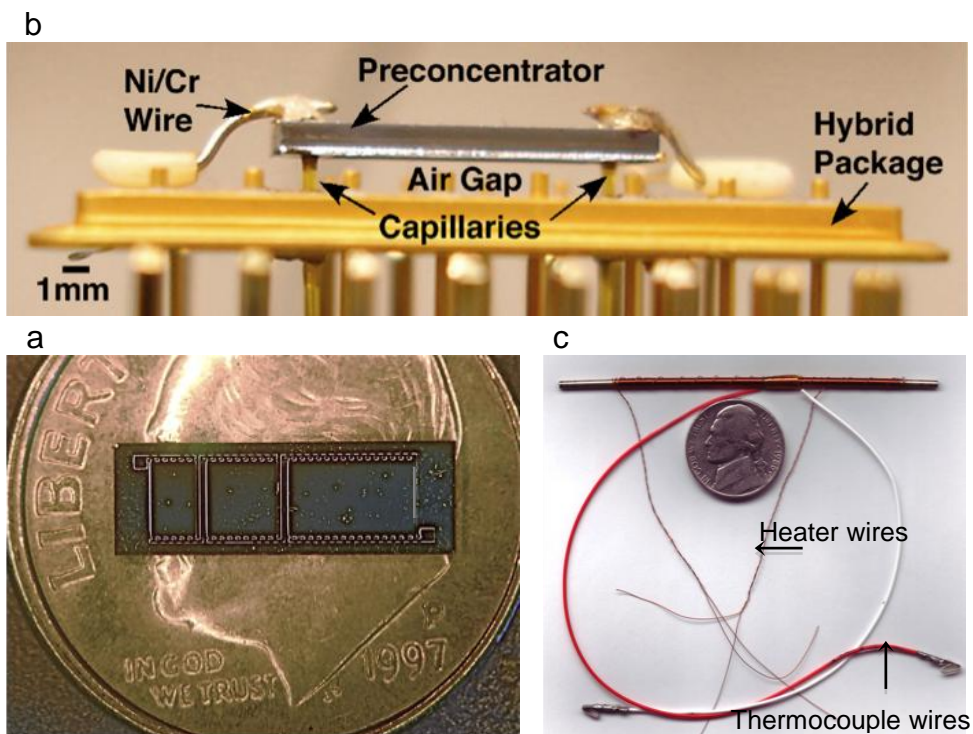


Figure 3-1. Pictures of a) inner cavities of the μ PCF on a dime, b) the multi-stage μ PCF in the testing package, and c) the cPCF with a wrapped heater and thermocouple with a nickel for size (clockwise from bottom left).

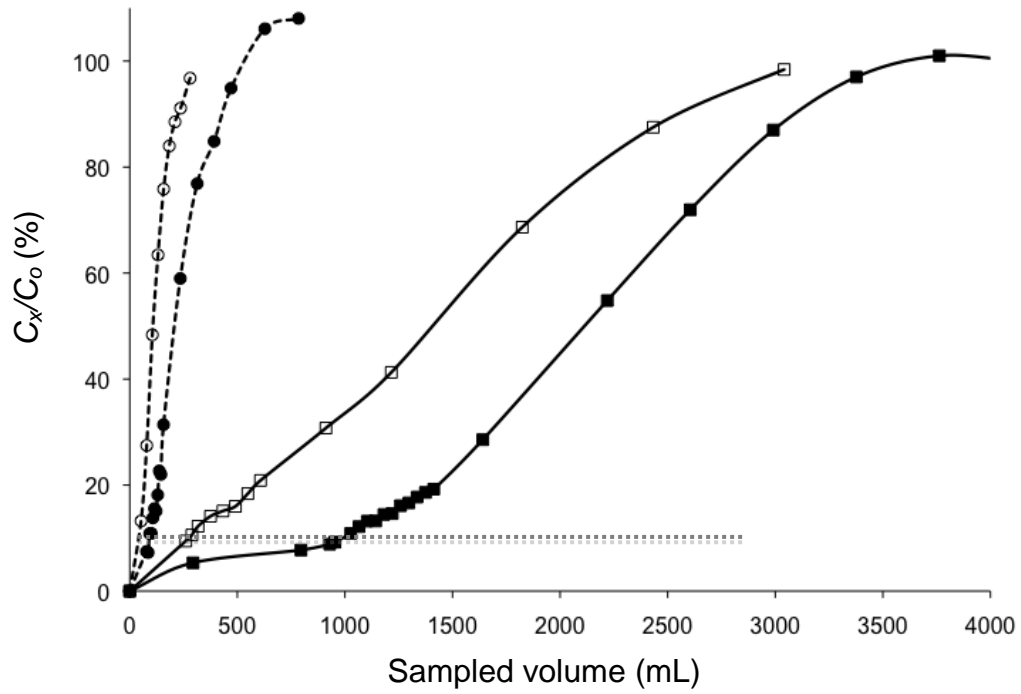


Figure 3-2. Breakthrough curves for toluene (squares) and benzene (circles) are shown for the longest (filled symbols) and shortest (open symbols) bed residence times, τ . The dashed line at $C_x/C_o=10\%$ is used to determine V_{b-10} for each curve. As shown, V_{b-10} decreases with decreasing τ .

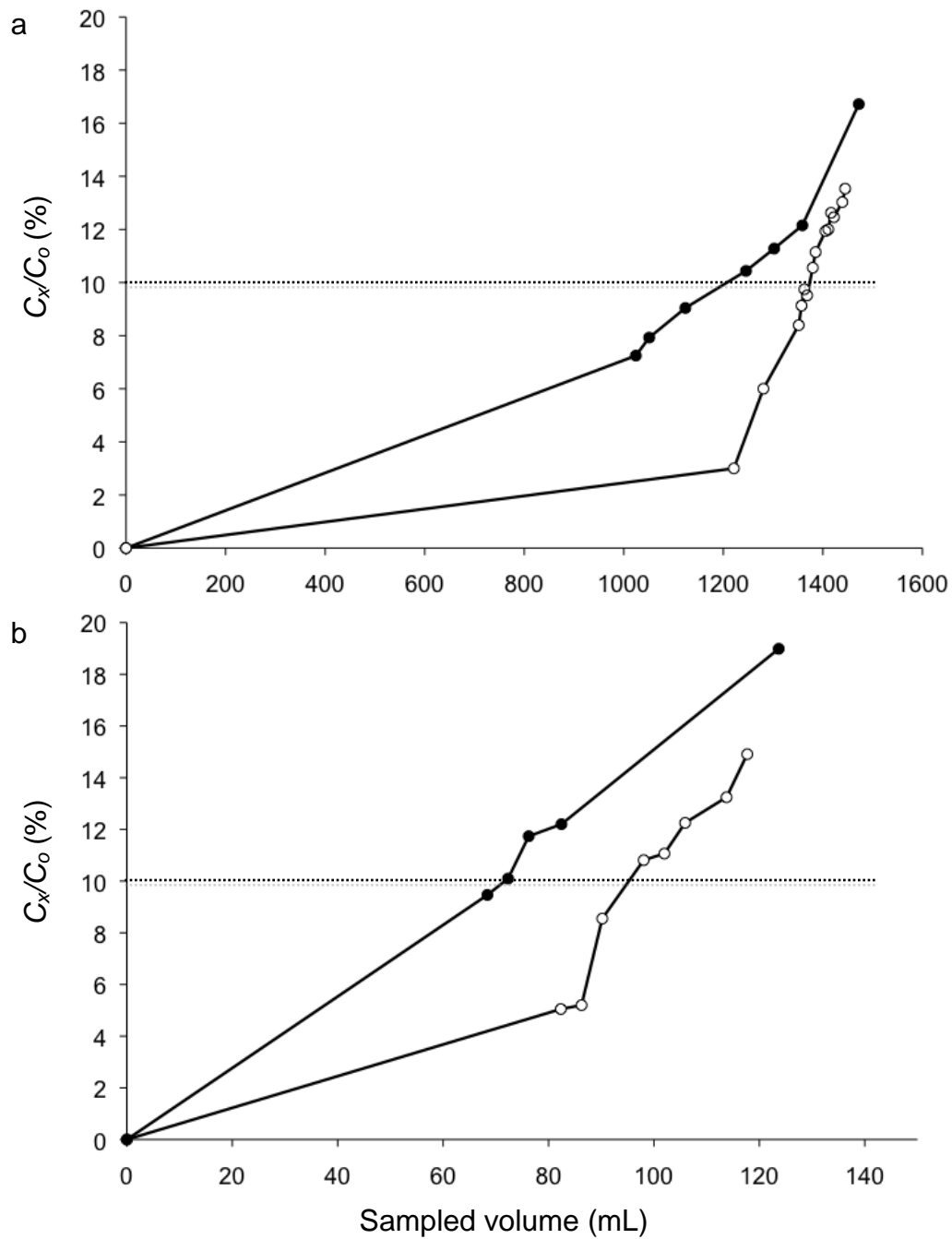


Figure 3-3. Breakthrough curves for a) toluene at 5 mL/min and b) benzene at 4 mL/min are shown to compare the difference in V_{b-10} for the cPCF (open symbols) and the μ PCF (filled symbols)

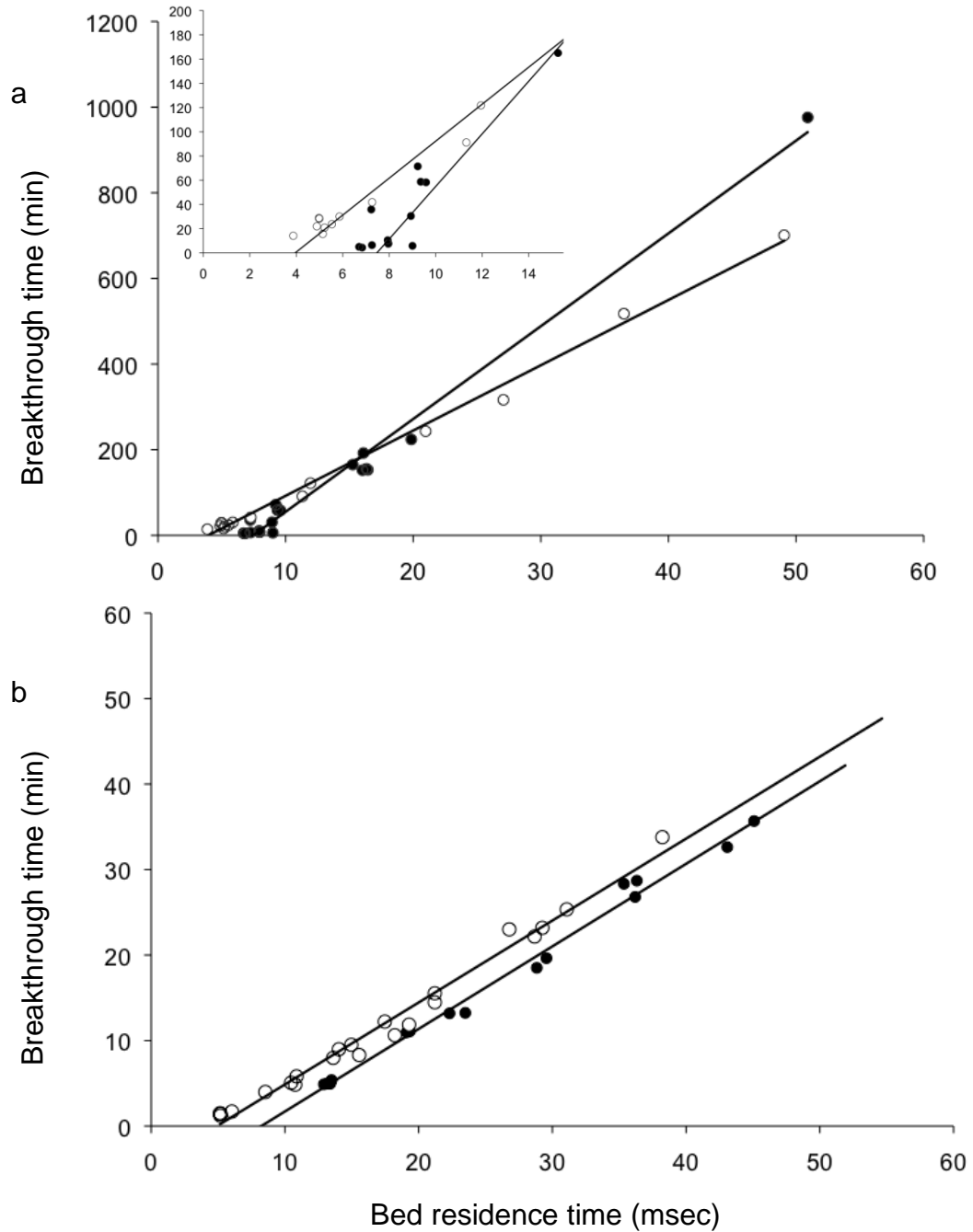


Figure 3-4. Linear plots of breakthrough time vs. bed residence time from the Wheeler model for a) toluene and b) benzene for the μ PCF (filled symbols) and the cPCF (open symbols). Similar slopes are observed for both devices, as expected, due to similar W_e , C_o , and ρ_B values.

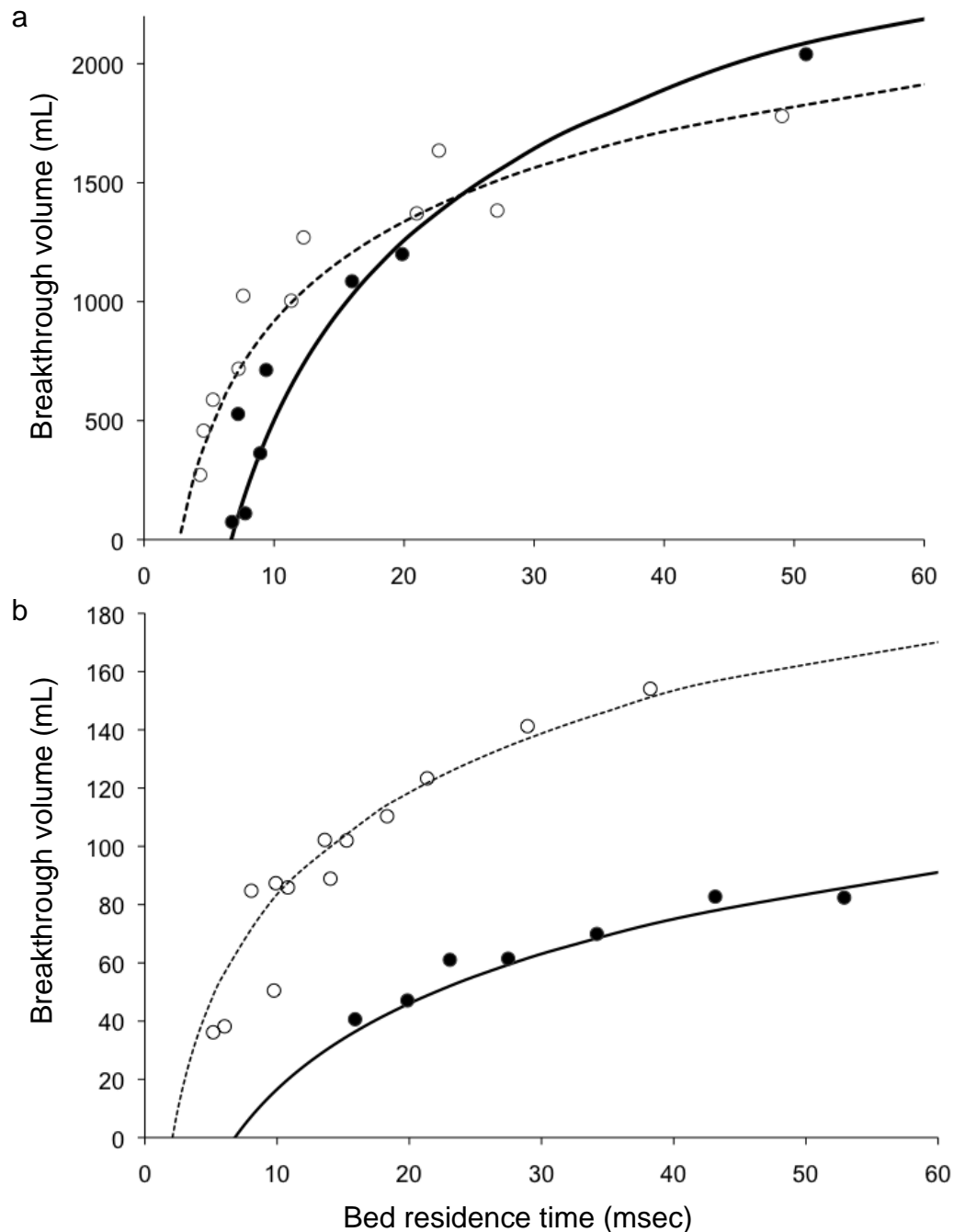


Figure 3-5. Breakthrough volume vs. bed residence time curves for a) toluene and b) benzene on the μ PCF (filled symbols) and the cPCF (open symbols). The solid lines show the Wheeler model description for the μ PCF using W_e values determined from gravimetric analysis and k_v values determined from the equation found when plotting k_v vs. linear velocity. The dashed lines show the Wheeler model description for the cPCF, determined in the same way as the μ PCF.

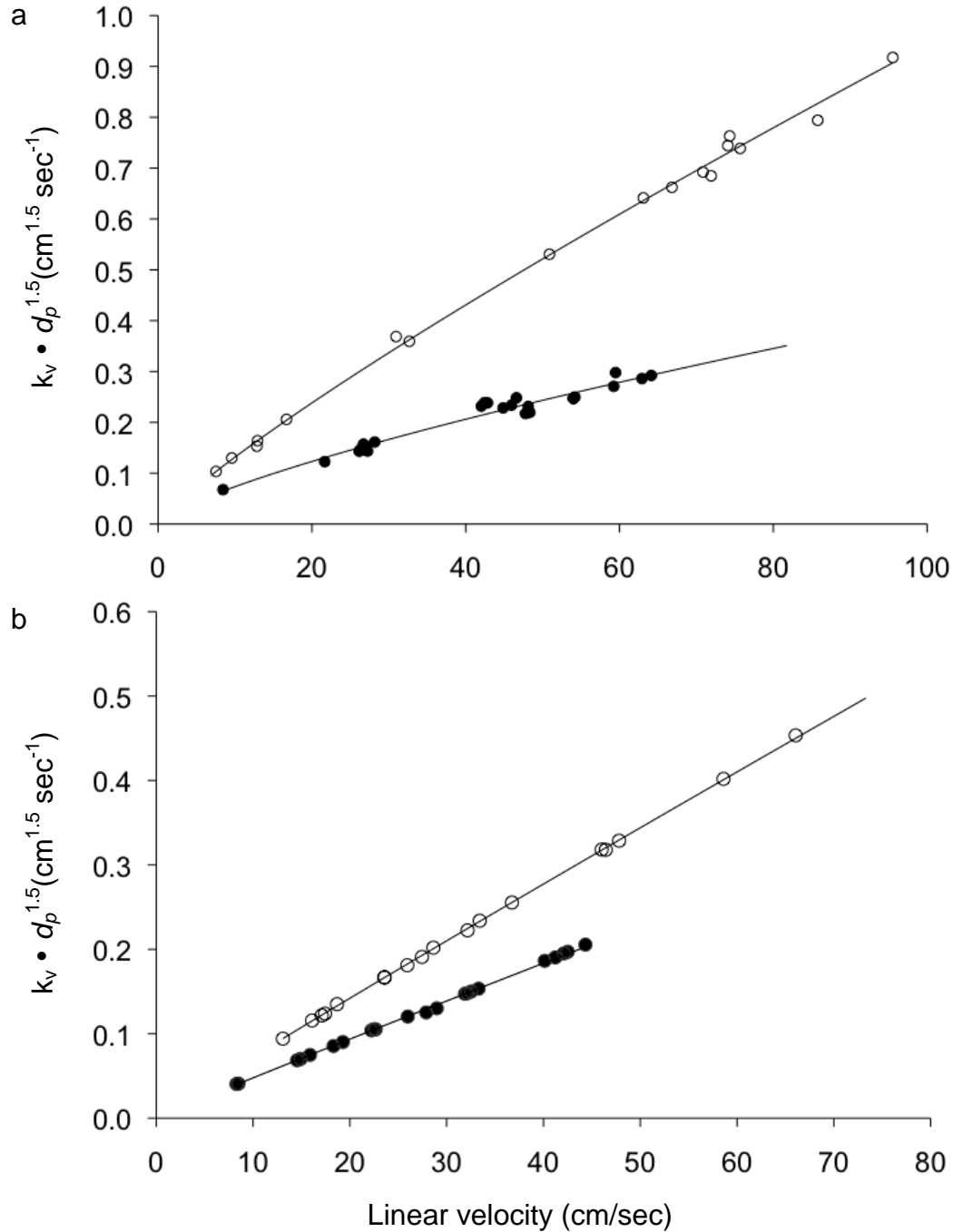


Figure 3-6. Curves reflecting the dependence of k_v on linear velocity are shown for a) toluene and b) benzene for the cPCF (open symbols) and the μ PCF (filled symbols). Accounting for particle diameter as part of the dependent variable does not result in coalescing curves and therefore separate equations of k_v for each device and vapor are required.

References

- [1] C. -J. Lu, W. H. Steinecker, W. -C. Tian, M. C. Oborny, J. M. Nichols, M. Agah, J. A. Potkay, H. K. L. Chan, J. Driscoll, R. D. Sacks, K. D. Wise, S. W. Pang, and E. T. Zellers, first-generation hybrid MEMS gas chromatograph, *Lab on a Chip*, 5 (2005) 1123-1131.
- [2] E. T. Zellers, S. Reidy, R. Veeneman, R. Gordenker, W. Steinecker, G. R. Lambertus, H. Kim, J. Potkay, M. P. Rowe, Q. Zhong, C. Avery, H. Chan, R. Sacks, K. Najafi, K. Wise, An integrated micro-analytical system for complex vapor mixtures, *Proc. 2007 Solid-State Sensor and Actuator Conf.-Transducers 07*, Lyon, France, 2007, pp. 2091 - 2094.
- [3] P. R. Lewis, R. P. Manginell, D. R. Adkins, R. J. Kottenstette, D. R. Wheeler, S. S. Sokolowski, D. E. Trudell, J. E. Byrnes, M. Okandan, J. M. Bauer, R. G. Manley, and G. C. Frye-Mason, Recent advancements in the gas-phase MicroChemLab, *IEEE Sensors J.*, 6 (2006) 784-795.
- [4] S. C. Terry, J. H. Jerman, and J. B. Angell, Gas-chromatographic air analyzer fabricated on a silicon-wafer, *IEEE Trans. Electron Dev.*, 26 (1979) 1880-1886.
- [5] C2V Concept to Volume, accessed online, <http://www.c2v.nl>
- [6] A. de Mello, On-chip chromatography: the last twenty years, *Lab on a Chip*, 2 (2002) 48N-54N.
- [7] SLS Micro Technology, accessed online, <http://www.sls-micro-technology.de>
- [8] B. Egorov, M. J. O'Hara, and J. W. Grate, Equilibration-based preconcentrating minicolumn sensors for trace level monitoring of radionuclides and metal ions in water without consumable reagents *Anal. Chem.*, 78 (2006) 5480-5490.
- [9] W. C. Tian, H. K. L. Chan, C. J. Lu, S. W. Pang, and E. T. Zellers, Multiple-stage microfabricated preconcentrator-focuser for micro gas chromatography system, *J. Microelectromech. Sys.*, 14 (2005) 498-507.
- [10] C.-J. Lu and E. T. Zellers, A dual-adsorbent preconcentrator for a portable indoor-VOC microsensor system, *Anal. Chem.*, 73 (2001) 3449-3457.
- [11] C.-J. Lu, E. T. Zellers, Multi-adsorbent preconcentration/focusing module for portable-GC/microsensor-array analysis of complex vapor mixtures, *The Analyst*, 127 (2002) 1061-1068.
- [12] W. C. Tian, S. W. Pang, C. J. Lu, and E. T. Zellers, Microfabricated preconcentrator-focuser for a microscale gas chromatograph, *J. Microelectromech. Sys.*, 12 (2003) 264-272.

- [13] H. K. L. Chan, S. W. Pang, R. A. Veeneman, E. T. Zellers, and M. Takei, Microfabricated preconcentrator for quantitative analysis of low concentration volatile organic compounds, Proc. 2005 Solid-State Sensor and Actuator Conf.-Transducers-05, Seoul, Korea, 2005, pp. 2091 - 2094.
- [14] E. T. Zellers, M. Morishita, and Q.-Y. Cai, Evaluating porous-layer open-tubular capillaries as vapor preconcentrators in a microanalytical system, Sens. Actuators B, 67 (2000) 244-253.
- [15] I. Ciucanu, A. Caprita, A. Chiriac, and R. Barna, Helical sorbent microtrap for continuous sampling by a membrane and trap interface for on-line gas chromatographic monitoring of volatile organic compounds Anal. Chem., 75 (2003) 736-741.
- [16] J. W. Grate, N. C. Anheier, and D. L. Baldwin, Progressive thermal desorption of vapor mixtures from a preconcentrator with a porous metal foam internal architecture and variable thermal ramp rates Anal. Chem., 77 (2005) 1867-1875.
- [17] S. Mitra and C. Yun, Continuous gas chromatographic monitoring of low concentration sample streams using an on-line microtrap J. Chrom. A, 648 (1993) 415-421.
- [18] C. Feng and S. Mitra, Two-stage microtrap as an injection device for continuous on-line gas chromatographic monitoring, J Chrom A, 805 (1998) 169-176.
- [19] M. Kim and S. Mitra, J. Chrom.A, A microfabricated microconcentrator for sensors and gas chromatography, 996 (2003) 1-11.
- [20] I. Voiculescu, R. A. McGill, M. E. Zaghoul, D. Mott, J. Stepnowski, S. Stepnowski, H. Summers, V. Nguyen, S. Ross, K. Walsh, and M. Martin, Micropreconcentrator for enhanced trace detection of explosives and chemical agents, IEEE Sensors J., 6 (2006) 1094-1104.
- [21] M. Martin, M. Crain, K. Walsh, R. A. McGill, E. Houser, J. Stepnowski, S. Stepnowski, H.-D. Wu, and S. Ross, Microfabricated vapor preconcentrator for portable ion spectroscopy, Sens. Actuators B, 126 (2007) 447-454.
- [22] C. E. Davis, C. K. Ho, R. C. Hughes, and M. L. Thomas, Enhanced detection of m-xylene using a preconcentrator with a chemiresistor sensor, Sens. Act. B., 104 (2005) 207-216.
- [23] R. P. Manginell, G. C. Frye-Mason, R. J. Kottenstette, P. R. Lewis, and C. C. Wong, Microfabricated planar preconcentrator, Technical Digest Solid-State

Sensor and Actuator Workshop, Hilton Head, SC, 2000, Transducer Research Foundation, Cleveland, pp. 179-182.

- [24] P. R. Lewis, R. P. Manginell, D. R. Adkins, R. J. Kottenstette, D. R. Wheeler, S. S. Sokoloswki, D. E. Trudell, J. E. Byrnes, M. Oandan, J. M. Bauer, R. G. Manley, G. C. Frye-Mason, "Recent advances in the gas-phase MicroChemLab," *IEEE Sens J*, 6 (2006), 784-795.
- [25] R. P. Manginell, S. Radhakrishnan, M. Shariati, A. L. Robinson, J. A. Ellison, R. J. Simonson, Two-dimensional modeling and simulation of mass transport in microfabricated preconcentrators, *IEEE Sensors J*. 7 (2007) 1032-1041.
- [26] W. A. Groves, E. T. Zellers, and G. C. Frye, Analyzing organic vapors in exhaled breath using a surface acoustic wave sensor array with preconcentration: selection and characterization of the preconcentrator adsorbent, *Anal. Chim. A.*, 371 (1998) 131-143.
- [27] B. Bae, J. Yeorni, R. Masel, M.A. Shannon, A five-microvalve fully integrated preconcentrator, *IEEE Sensors J.*, 1-3 (2007) 1353-1356.
- [28] A. Wheeler and A. J. Robell, Performance of fixed-bed catalytic reactors with poison in feed, *J. Catalysis*, 13 (1969) 299.
- [29] L. A. Jonas, Y. B., Tewari, and E. B. Sansone, Prediction of adsorption rate constants of activated carbons for various vapors, *Carbon*, 17 (1979) 345-349.
- [30] R. A. Veeneman and E. T. Zellers, Characterizing vapor adsorption on graphitized carbons at low concentrations, *Carbon*, submitted.
- [31] L. A. Jonas and J. A. Rehrmann, Rate of gas adsorption by activated carbon, *Carbon* 12 (1974) 95-101.
- [32] J. A. Rehrmann and L. A. Jonas, Dependence of gas adsorption rates of gas adsorption rates on carbon granule size and linear flow velocity, *Carbon* 16 (1978) 47-51.
- [33] G. O. Wood and J. F. Stampfer, Adsorption rate coefficients for gases and vapor on activated carbons, *Carbon* 31 (1993) 195-200.
- [34] P. Lodewyckx and E. F. Vansant, Estimating the overall mass transfer coefficient k_v of the Wheeler-Jonas equation: A new and simple model, *Am. Ind. Hyg. Assoc. J.* 61 (2000) 501-505.

- [35] G. O. Wood and P. Lodewycky, An extended equation for rate coefficients for adsorption of organic vapors and gases on activated carbons in air-purifying respirator cartridges, *Am. Ind. Hyg. Assoc. J.* 64 (2003) 646-650.
- [36] Stanek, V. *Fixed Bed Operations: Flow Distribution and Efficiency*, Ellis Horwood: New York, 1994; Chapter 3.

Chapter 4

Wheeler Model Predictions of Binary Mixture Breakthrough Volumes on a Miniature Preconcentrator Filled with Graphitized Carbon

Introduction

Field-portable gas chromatographs (GC) designed for on-site determinations of multiple volatile organic compounds (VOC) have been commercially available for nearly 40 years [1], and the first “microGC” (μ GC) was reported about 30 years ago [2]. Since then, numerous advances have been made to reduce the size and power requirements while improving the sensitivity, selectivity, and reliability of measurements obtained with such instruments [3-6]. The ability to separate the components of VOC mixtures by passage through a chromatograph column and to detect each component separately is the most useful aspect of such instruments, and arguably the reason why they have been of such value in field assessments of airborne VOCs. However, in many applications, the levels at which VOCs must be detected are much lower than the detection limits of commonly used GC detectors. This, in turn, has led to use of adsorbent preconcentrators as integral components of such instruments.

Preconcentrators generally fall into two categories: those relying on equilibrium partitioning of VOCs into/onto a sorbent, in which only a fraction of the mass of each VOC in the sample stream is retained [7-17]; and those relying on exhaustive capture via

adsorption onto a granular solid, in which the entire mass of each VOC present in the sample stream is retained [18-23]. Subsequent rapid thermal desorption yields an injection band that is presented to the inlet of the separation column. In contrast to bench-scale GCs that employ an intermediate focusing stage between the preconcentrator and the column, most field GCs try to minimize the size of the preconcentrator so that it can serve as both a preconcentrator and a focuser. For this reason, the term ‘preconcentrator/focuser’ (PCF) is more appropriate.

While many of these studies challenge the preconcentrators with mixtures [8, 9, 13-17, 21-23], only a few that examine the factors affecting preconcentrator performance (adsorbent bed mass, flow rates) in the context of mixtures [18, 19]. The focus of a majority of these studies is demonstrating preconcentration and detection of vapor mixtures, and do not investigate the PCF parameters that contribute to such performance, as in operating flow rate or adsorbent mass [8, 9, 13-17]. Lu et al. provide two of the more informative studies determining the breakthrough volumes of designated vapors in the presence of up to 43 other vapors [18, 19]. Their first study examined PCF performance as a function of adsorbent bed mass for a 7-vapor mixture [18]. From this study, they determined the optimum amount of adsorbent mass to be included in a PCF and then demonstrated capture, preconcentration, and analysis of a 20-vapor mixture. Their second study extended the analysis to include a 44-vapor mixture [19]. As with their first study, adsorbent bed mass was optimized to demonstrate capture, preconcentration, and analysis of the mixture. However, lacking in both these studies was a similar analysis with a single vapor to show the effect of a mixture on the preconcentration performance. Furthermore since desorption performance was the key

aspect of interest in both these studies the effect of mixtures on either the optimal adsorbent mass or operating flow rate was not shown.

In all the studies examining mixtures on PCFs, none of them demonstrate modeling of binary mixtures. Modeling the breakthrough volume of single vapors has been performed [18-20], but the extension of these model to binary mixtures has not been presented. Because the analysis of mixtures and the performance of the packed beds over a range of flow rates is key in designing the next generation of PCFs, this study extends the analysis of mixtures to determine the kinetic factors (flow rate) affecting PCF performance in the context of binary mixtures. The experimental results are compared against theoretical data modeled using an extension of the Wheeler model used to predict adsorbent bed performance for binary mixtures.

Single Vapor System

When measuring the performance of a packed bed PCF, breakthrough volume is often the most useful metric. The breakthrough volume (V_b) is the volume of contaminated air that can be sampled while maintaining quantitative adsorption. For single vapors on a solid adsorbent bed, the modified Wheeler model can be used to predict V_b as a function of adsorbent bed and operating parameters [25, 26]:

$$V_b = \frac{W_e W_B}{C_0} \left[1 - \frac{1}{k_v \tau} \ln \left(\frac{C_0}{C_x} \right) \right] \quad (4.1)$$

where W_e is the equilibrium adsorption capacity (g/g), W_B is bed mass (g), C_0 is the challenge concentration (g/L), C_x is the pre-determined concentration downstream from

the bed at which point breakthrough occurs (g/L), k_v is the kinetic rate coefficient (min^{-1}), and τ is the bed residence time (min), equal to $\varepsilon W_B / \rho_B Q$ (L/min) where ε is the interparticle porosity, ρ_B mass of adsorbent contained in the volume of the PCF bed (g/cm^3). When applying the Wheeler model to the preconcentrators used here, C_x was 10% of C_0 .

In order to apply the Wheeler model in a predictive manner, W_e and k_v must be determined, and they are often obtained from a series of breakthrough volume experiments where breakthrough volume is plotted against W_B , with the resulting linear regression yielding W_e and k_v from the slope and y-intercept, respectively [27]. Many applications of the Wheeler model use this method to predict breakthrough volumes for untested adsorbent beds [28, 29]. However, once this series of breakthrough experiments have been performed to obtain W_e and k_v , the Wheeler model is no longer needed to predict V_b since it has already been measured.

The data presented here extends his work to examine mixtures on a miniature preconcentrator while varying flow rates and attempts to model this data by applying simple correction factors to data obtained from single vapor analysis. A different approach was used when applying the Wheeler model to single vapors. First, W_e was determined and modeled independently using thermogravimetric analysis and the Dubinin-Radushkevich model (DR) [30]. Using experimentally determined W_e values, the Wheeler model was used to calculate k_v over the range of flow rates. By inputting operating parameters (C_0 , τ), preconcentrator parameters (W_b) and experimentally determined V_b , k_v can be calculated from Equation 4.1. Plotting the calculated k_v values

vs. linear velocity allows verification of the Lodewyckx and Wood empirical correlation for k_v :

$$k_v = 13.3\beta^{0.33}v_L^{0.7}d_p^{-1.5}\left(\frac{W_e}{MW}\right)^{0.5} \text{ sec}^{-1} \quad (4.2)$$

where β is the affinity coefficient taken from the DR model, v_L is the linear velocity (cm/sec), d_p is the particle diameter (cm), and MW is molecular weight (g/mole) [31, 32]. Miniature beds (<2 mg) were used in this study, but applications of the Wheeler model, DR model, and the Lodewyckx and Wood correlation have predominately involved larger beds ($\geq 10^4$ -fold larger). Therefore, the verification of their validity was an important step prior to extending the analysis to binary mixtures. A previous study combined the independent determination of W_e and an empirical correlation for k_v similar to that of Equation 4.3 to describe V_b for single vapors on both a μ PCF and capillary PCF over a range of bed residence times, with errors of less than 18% [33]. Using these results, the study was extended to binary mixtures.

Binary Vapor System

The Wheeler model was designed for single vapor analysis only. This is a significant constraint because most applications involve the analysis of complex mixtures. There have been a few studies in which the effect of a second vapor on the values of V_b , W_e , and k_v of the first vapor has been explored [28, 29, 34-42]. Most of these studies rely on performing linear regression with the Wheeler model (as described above) to determine W_e and k_v for both the single vapor and binary vapor analysis [29,

34-37]. For binary mixtures, the measured breakthrough volume (of the mixture) is plotted against the adsorbent mass to determine W_e and k_v for the mixture from the slope and y-intercept, respectively.

In order to successfully apply the Wheeler model, as a predictive tool, to binary mixtures, W_e and k_v for each vapor in the mixture must be determined. Various methods have been proposed to determine W_e for the components of mixtures. Wood provides a review of these methods with analysis of their accuracy [43]. The methods reviewed by Wood include volume exclusion theories, models based on ideal adsorbed solution theory (IAST), adsorption potential theory, the Lewis equation and proportionality methods. The exclusion theories are based on the Dubinin-Radushkevich isotherm equation, with the premise that once vapor has occupied a fraction of the pore volume, that volume is not available for adsorption by a second vapor.

Ideal adsorbed solution theory, adsorption potential theory, and Lewis equation mixture analyses depend both require isotherms to determine the total capacity for the mixture. The adsorption potential theory does not assume additivity of the adsorbed vapors, and the Lewis equation requires knowledge of the partial molar volumes of the adsorbed species. Additionally, the IAST is dependent on the differences in the surface tensions of the adsorbed species, which assumes a higher surface coverage than typically found in application for field-deployable instruments.

Proportionality methods, however, are rather straightforward in their application. For this initial study, the simplest model, the Molar Proportionality Method (MPM), was chosen to determine W_e . The MPM has been used to determine W_e for binary mixtures

with accurate determinations of V_b . MPM allows for calculation of new W_e values based on the mole fraction of the vapors in the challenge sample:

$$W_{e(t)} = x_1 W_{e(1)}^0 + x_2 W_{e(2)}^0 \quad (4.3)$$

where $W_{e(t)}$ is total amount adsorbed in the mixture (g/g), x_1 and x_2 are the mole fractions of components 1 and 2 in the gas phase and $W_{e(1)}^0$ and $W_{e(2)}^0$ are the amounts (g/g) adsorbed by single vapor 1 and 2, respectively, adsorbed when presented individually to the adsorbent (g/g) at the same concentration as the mixture (as determined from separate exposure experiments).

This method has been applied with reasonable success to large-scale adsorbent beds, although determination of the mole fraction whether it is for the gaseous state or the adsorbed state remains a point of disagreement [34, 42, 43]. We opted to use the gaseous mole fraction, calculated from the concentration, in terms of p/p_{sat} :

$$x_i = \frac{(p/p_{sat})_i}{\sum (p/p_{sat})_i} \quad (4.4)$$

where p is the partial pressure of the analyte and p_{sat} is the saturation vapor pressure [34]. This method was applied by both Jonas et al. [34] and Vahdat [42]. Jonas investigated mixtures of carbon tetrachloride/benzene, carbon tetrachloride/chloroform, and chloroform/benzene [34]. Vahdat, on the other hand investigated mixtures of acetone/m-xylene, acetone/styrene, and carbon dioxide/water vapor [42]. Both presented studies on

respirator cartridges (>1 g) at relatively high concentrations (>100 ppm), and high flow rates (100 mL/min).

Jonas, however, was the only author to provide an analysis of fit between model-determined W_e values, from the MPM, and experimentally determined W_e values. His experimental W_e values were determined by performing linear regressions on plots of mixture breakthrough volume vs. adsorbent bed mass, which yields W_e for the component in the mixture from the slope. Using the MPM, deviations in values of W_e for all the mixture components were from -10 to +20%. From this analysis, consisting of three different vapor pairs at two mole fractions, no single mixture, vapor pair or mole fraction, yielded better model W_e values (lower deviations) than another. Based on their analysis, they determined the MPM was an appropriate method for determining adsorption capacity for binary mixtures, with the caveat that the results were valid only for the carbon material tested [34]. Vahdat came to a similar conclusion for the vapor pairs he tested [42], although without the statistical analysis.

Determination of k_v for a mixture is only slightly more straightforward. Wood reviewed the mixture breakthrough volume data from six different authors and nine different studies with the goal of determining the effect of co-vapors on the adsorption rate coefficient [28]. These data were collected mostly on respirator cartridges [29, 34-42]. From these studies and his independently collected data, Wood concluded that the effect of mixtures on k_v differs depending on the breakthrough order. Vapors that breakthrough first showed no difference, on average, between k_v in a mixture and k_v for a single vapor (mixture k_v :single $k_v = 1 \pm 0.21$). This is because the rate of adsorption of the first vapor moving through the bed is unaffected by the presence of the second vapor,

which lags behind. Vapors that breakthrough later exhibited an average 15% decrease in k_v (mixture k_v :single $k_v = 0.85 \pm 0.24$). This is only true for vapors with sufficiently different breakthrough volumes, although he did not specify the extent of the difference needed to qualify for this decrease. For vapors with similar breakthrough volumes, the 15% decrease is to be applied to both vapors (mixture k_v :single $k_v = 0.85 \pm 0.16$), regardless of breakthrough order [28]. While Wood provides a simplified method of determining k_v for mixtures, he did observe significant standard deviations and admits to difficulty in determining k_v from linear regressions from breakthrough volume or time.

Since the adsorbent beds of interest for the micro-GCs is $>10^4$ -fold smaller, the applicability of these models has been untested. Furthermore, when breakthrough time vs. bed residence time is used to determine k_v , as the case with many studies, the linear regression assumes k_v to be independent of flow rate, which is not the case. Additionally, none of the studies examined the adsorption of mixtures over a range of flow rates.

Breakthrough volumes were determined for binary mixtures as a function of linear velocity and compared to the results obtained with the individual vapors at the same concentrations. Values of the thermodynamic W_e for the individual vapors were determined gravimetrically (see Chapter 2).

Experimental

Materials

Vapor choices were limited to those with W_e values determined by thermogravimetric analysis and were chosen based on vapor pressure to ensuring capture on the adsorbent bed. Benzene ($p_v=95$ torr, MW=78.11 g/mole), heptane ($p_v=49$ torr,

MW 100.2 g/mole), and toluene ($p_v=28$ torr, MW=92.14) were chosen as test vapors for those reasons. Mixtures of benzene and toluene, and heptane and toluene were chosen to represent varying strengths of adsorbates on the adsorbent of choice. A single adsorbent bed was tested containing Carbopack X (Supelco, Eighty-Four PA), a graphitized carbon commonly used in the preconcentrators developed here (specific surface area 250 m²/g). Prior to use, Carbopack X was sieved to 112-140 μm .

Preconcentrator Construction

The PCF was constructed by packing a 5-cm section of thin-wall Inconel (1.59-mm o.d., 1.35-mm i.d.) with 1.35 mg of Carbopack X that had been passed through sieves to isolate the fraction with nominal diameters in the range of 112-140 μm . The adsorbent was drawn into the tubing under vacuum and was retained in place by small pieces of stainless steel mesh and silanized glass wool [18, 19]. The bed occupied a length of ~4 mm and was located within 1-cm of the distal end of the tubing to minimize the downstream dead volume. A thin sleeve of polyimide (Microlumen, Tampa, FL) was placed around the packed section of the tube and a fine-wire type-K thermocouple was placed against the tube and held in place with another thin polyimide sleeve. A length of varnished Cu wire, used to resistively heat the adsorbent bed following each test, was then coiled tightly around this assembly to create a heated length that extended beyond the length of the adsorbent bed.

Atmosphere Generation

Since air concentrations for the applications of interest are expected to be in the

part-per-billion to part-per-trillion range, challenge concentrations were generated to be around 100 ppb. Benzene and heptane ($\geq 99\%$ from Sigma Aldrich) atmospheres were generated in seasoned Tedlar bags by injecting a volume of liquid solvent into a known volume of clean, dry air to achieve 100 ppm. A 10 mL aliquot was transferred to a second seasoned bag by a gas-tight syringe to yield 100 ppb air concentration of benzene and 90 ppb air concentration of heptane. A seasoned Tedlar bag is achieved by pre-exposing the bag to the vapor atmosphere and purging with clean, dry air until no traces of vapor are detected by FID. Toluene atmospheres were generated by transferring a 10 mL aliquot via a gas-tight syringe from a test atmosphere drawn from a purchased cylinder (Scott Specialty Gases, 101 ppm, 0% relative humidity) into a bag filled with clean, dry air to generate an air concentration of 100 ppb of toluene.

Breakthrough Volumes

Test atmospheres containing 110 ppb of either benzene or toluene in clean, dry air were created in 10-L Tedlar bags by serial dilution. Breakthrough volumes were determined by drawing the challenge concentration through the preconcentrator using a vacuum pump (UN86KTDC, KNF Neuberger, Trenton, NJ). A charcoal scrubber was placed in-line to protect the pump from vapors. At 1-min intervals an aliquot of the outlet stream was directed into a GC with flame-ionization detector (GC-FID, Model 6890, Agilent Technologies, Palo Alto, CA) via a six-port valve equipped with a 250- μ L gas sampling loop. The flow rate was measured, using a primary flow standard, and a rotameter was adjusted to achieve the desired flow rate. The column oven temperature was adjusted to give a retention time of 0.5-0.8 min. Peak integration was performed at

the conclusion of each experiment using GRAMS32 (Version 6.0- Thermo-Scientific, Pittsburg, PA).

Breakthrough curves (C_x/C_o vs. volume) were generated in duplicate for Q and τ values ranging from 4-28 mL/min and 5-35 msec, respectively. Values of t_{b-10} and V_{b-10} were determined at $C_x/C_o = 0.1$ directly or by (linear) interpolation between the two nearest data points. The flow rate was measured at the end of every breakthrough curve with a soap bubble flow meter and the challenge concentration was measured prior to and at the end of every breakthrough determination. Concentrations were verified by comparison of FID peak areas to those generated by injection of a series of benzene and toluene solution standards generated in CS_2 that spanned the range of injection masses covered during the breakthrough tests. The preconcentrators were preconditioned by heating under N_2 for four hours at $200^\circ C$. Subsequently, after each experiment the adsorbent was regenerated under a flow of N_2 of ~ 20 mL/min by heating the device under test to $200-300^\circ C$ for 30 min to desorb the vapor.

Results and Discussion

Single Vapor Analysis

Breakthrough volumes were determined over a range of flow rates corresponding to bed residence times of 5-50 msec for each of the individual vapors in separate test series. Similar relationships between V_b and τ were observed for all three individual vapors as single components, (Figure 4-1). At τ values < 10 msec, there is marked increase in the dependence of V_b on τ . As single vapors, we found breakthrough volumes for benzene to be the shortest, with toluene and heptane exhibiting nearly identical

breakthrough volumes. Benzene was expected to have the shortest breakthrough volume since it has the lowest W_e value. Based on equilibrium W_e values alone, heptane was expected to have smaller breakthrough volumes in comparison to toluene.

Using the breakthrough volumes determined and the W_e values obtained from independent gravimetric analysis, k_v was determined for these vapors. Values of W_e are listed in Table 4-1. An empirical relationship between k_v and linear velocity had been previously established for benzene and toluene on Carbopack X (see Chapter 3), but it had not been established for heptane. The same procedure used for determining k_v as a function of linear velocity for toluene and benzene was used for heptane. For all three vapors models of k_v having the form of Equation 4.2 could be generated. However, each vapor required a separate model (Figure 4-2). The models giving the best fits for k_v for toluene, benzene, and heptane are given in Equations 4.5, 4.6, and 4.7, respectively.

$$k_v = 4.3\beta^{0.33} d_p^{-1.5} v_L^{0.85} \left(\frac{W_e}{MW} \right)^{0.5} \quad (4.5)$$

$$k_v = 3.5\beta^{0.33} d_p^{-1.5} v_L^{0.95} \left(\frac{W_e}{MW} \right)^{0.5} \quad (4.6)$$

$$k_v = 8.4\beta^{0.33} d_p^{-1.5} v_L^{0.73} \left(\frac{W_e}{MW} \right)^{0.5} \quad (4.7)$$

Interestingly, heptane exhibits higher k_v values than toluene, despite having a lower value of W_e . Values of W_e are listed in Table 4-1. However, because nearly identical V_b values

were found for toluene and heptane, k_v must be larger than toluene in order to follow Equation 4.1 with a smaller W_e . The regressions for toluene and benzene yielded r^2 values of >0.97 , but the heptane regression yielded an r^2 of 0.82, indicating a greater degree of scatter in the data. The larger standard deviation in the heptane data may also be contributing to its anomalous behavior, i.e. similar V_b values for a smaller W_e .

We observed the largest k_v values for heptane, and the smallest k_v values for benzene. While the form was approximately the same, there is a range of linear velocity dependences between the three vapors, from $v_L^{0.73}$ for heptane to $v_L^{0.95}$ for benzene. This trend in linear velocity exponents, heptane $<$ toluene $<$ benzene, is the opposite of the trend observed with V_b where heptane $>$ toluene $>$ benzene. Since V_b is essentially $W_e - I/k_v$ (with all other variables in Equation 4.1 being equal), the trends observed between k_v and V_b make sense. W_e is largest for toluene, but yields mid-range k_v values. However, W_e is smallest for benzene, which yields the smallest values of k_v , and the largest values of I/k_v . Since I/k_v is subtracted from an already small W_e term, a smaller V_b results. For heptane, while W_e is smaller than toluene, the amount subtracted (I/k_v) is smaller than what is subtracted for toluene, which results in a larger V_b . While the trend of k_v can be somewhat rationalized, the difference in the dependence of k_v on linear velocity for the three vapors, makes it impossible to accurately fit the data to a single correlation.

Binary mixture analysis

Breakthrough curves for both binary mixtures were generated (Figure 4-3 and 4-4). For this discussion, the naming convention will be as follows: ben/tol (benzene with toluene as the co-vapor), tol/ben (toluene with benzene as the co-vapor), tol/hep (toluene

with heptane as the co-vapor), and hep/tol (heptane with toluene as the co-vapor). When examining the shapes of the breakthrough curves, we observed a quick breakthrough for benzene, which exceeds 100% just as toluene begins to breakthrough (Figure 4-3). This phenomenon is known as roll-up where the later adsorbing vapor displaces the first vapor, causing a temporary increase in the outlet concentration. When toluene is first adsorbing, the concentration of benzene is actually higher than the initial test concentration by 20% since it is being displaced by toluene. This was accounted for when calculating the mole fractions. The same phenomenon was seen with toluene and heptane (Figure 4-4). Toluene exceeds the initial challenge concentration by ~40%. However, since heptane reaches breakthrough prior to the roll-up occurring for toluene, it was not necessary to take this increased concentration into account when predicting 10% V_b .

Toluene exhibits a higher roll-up with heptane than benzene with toluene. This is due to the lower W_e for benzene. Benzene has a W_e value six times lower than toluene and its breakthrough volume is 10 times lower. As toluene begins adsorbing on the PCF, benzene has occupied fewer sites initially, due to its lower W_e value, which leaves less benzene to be displaced by toluene. Heptane and toluene in contrast have more similar W_e values and similar breakthrough volumes as single vapors. Therefore, toluene occupies more sites initially, which yields more toluene for heptane to displace, resulting in a larger roll-up.

When further examining the effect of co-vapors on breakthrough, breakthrough volume was examined as a function of bed residence time, as we did with single vapors [26]. With single vapors, the breakthrough volume of the vapor is dependent on the bed

residence time (Figure 4-1). Like benzene, toluene, and heptane alone, the mixtures exhibit a more distinct decrease in breakthrough volumes at bed residence times shorter than 15 msec. At bed residence times longer than 15 msec, the effect is less noticeable. The decrease in breakthrough volume with decreasing bed residence time is more gradual. For bed residence times longer than 15 msec, a 20% decrease in bed residence times results in only a 10% decrease in breakthrough volume. However, at bed residence times shorter than 15 msec, the same 20% decrease in bed residence time results in 25% decrease in bed residence time. While the general trend stayed the same between single vapors and binary mixtures, the magnitude of the decrease changed when in a mixture. For single vapors, the decrease seen at shorter bed residence times was much larger (50%), in comparison to the mixtures, where the decrease is only 25% [26]. This indicates that in a mixture, bed residence times do not affect the breakthrough volume to the same extent as a single vapor.

Since values had been obtained for k_v for the single vapors, we used previously published correction factors to predict the change in k_v for mixtures. When comparing compounds that breakthrough first in the mixture, it was expected that the k_v would not change, since the vapor interacts with the adsorbent bed as if it is a single vapor [21]. Vapors the breakthrough second, and those that have similar breakthrough volumes are expected to decrease by 15%. We calculated k_v for a moderately chosen flow rate (10 cm/sec, 15 mL/min), using MPM to determine the W_e value for each vapor in the mixture, and then compared the differences. Table 4-1 gives the mole fraction and resulting W_e for each vapor. In the case of ben/tol where benzene was the first compound to breakthrough a ratio of mixture k_v to single k_v was found to be 1.4 (242 and 179 sec⁻¹,

respectively). This increase indicates that the co-vapor does not negatively affect the adsorption rate coefficient. Wood calculated an average ratio of 1.0 for compounds with this breakthrough pattern, although he did see ratios as high as 1.7 [28]. Toluene gave a ratio of 0.86 (187 and 217 sec^{-1} for mixture and single k_v , respectively), which follows the expected 15% decrease in k_v Wood observed for his respirator beds [28].

Toluene and heptane, though, gave results different than expected. According to Wood, k_v was expected to decrease by 15% for both vapors, since they had similar breakthrough volumes as single vapors [28]. However, when comparing the ratios of mixture k_v to single k_v , ratios of 0.86 (186 and 217 sec^{-1}) and 0.99 (345 and 348 sec^{-1}) was obtained for toluene and heptane, respectively. Toluene maintained the expected decrease, but heptane showed no decrease at all. When competing for adsorption sites with toluene, heptane adsorbs more efficiently, as seen with the higher k_v values for heptane as a single vapor, which results in less of an impact of a covapor on the k_v values for heptane. In other words, since heptane is adsorbed more efficiently so a covapor does not affect k_v to the same extent it would vapor less efficiently adsorbed. The implications this has on predicting the breakthrough volume with the Wheeler model is discussed in the next section.

When comparing the order of breakthrough volume, more unexpected results were found. With benzene and toluene, benzene had the shortest breakthrough volume. This is consistent with a larger W_e yielding a higher breakthrough volume [35]. With heptane and toluene, toluene had the shortest breakthrough volume, which was unexpected because toluene has a higher W_e value. However, while the W_e was lower for heptane than toluene at the concentration tested, k_v was much higher. This higher k_v

added significance to the second term of the Wheeler model with in turn decreased the significance of W_e and gave a larger breakthrough volume. Determination of V_b from the Wheeler model is achieved by subtracting the k_v term from the W_e term (equation 4.1). Since heptane has smaller values of W_e , a smaller first term ($W_e W_b / C_o$) results. However, k_v is larger, which when taken in the second term of Equation 4.1 as $1/k_v$ results in a smaller number. Since $1/k_v$ is subtracted, a smaller change is observed when compared to subtracting the same $1/k_v$ term for toluene, which is nearly two-fold larger. So while the order of breakthrough was unexpected based on W_e values, the increase in k_v observed with heptane accounts for this.

Modeling of Binary Mixtures

When modeling mixtures, we applied Equations 4.3 and 4.4 to determine W_e for the binary vapors (Table 4-1). For k_v , we applied correction factors found by Wood: no correction factor is applied for the k_v of compounds with the first breakthrough volume (ben/tol), a 15% decrease is applied to k_v for compounds with longer breakthrough volumes (tol/ben), and a 15% decrease is applied k_v for compounds with nearly identical single vapor breakthrough volumes (tol/hep and hep/tol) [21]. The correction factors were applied to the equation of k_v determined for each vapor (Figure 4-4).

As seen in Figure 4-1, the model underestimates the breakthrough volume over the entire range of bed residence times for ben/tol and hep/tol. On the other hand, the model overestimates the breakthrough volume for tol/ben and tol/hep at bed residence times longer than 13 msec and underestimates the breakthrough volumes at times shorter than 13 msec. From all this, deviations from the experimental data were found to

between -33% and 6%. The standard deviations were high (up to 0.4) but they are well within the ranges published with these methods on respirator cartridges [28, 29, 34-39]. The highest average deviation of -33% was found for ben/tol, although hep/tol was in the same range at -29%. The remainder pairs gave 6% and -10%, for tol/ben and tol/hep, respectively. These values are deceiving, however, since the deviation for the longest bed residence time was 46% for tol/ben and 32% for tol/hep and the shortest bed residence time was -68% for both tol/ben and tol/hep. However, since an average was taken, the deviations across the entire data set are low. The lowest deviations for these pairs were obtained at 16 msec (12%) and 12 msec (16%) for tol/ben and tol/hep, respectively, which correspond to the points where the model switches from underestimating to overestimating. A complete list of range of deviations and standard deviations is given in Table 4-1. The deviations from expected values are also exhibited in calculations of the critical bed residence times.

The Wheeler model was used to calculate the critical bed residence time, the point at which zero breakthrough volume occurs, for both the single vapor and the mixtures. The critical bed residence times were found to be 3 msec for benzene, 2 msec for heptane and 2 msec for toluene as single vapors from the Wheeler model (Figure 4-1). Solving Equation 4.1 for τ with $V_b=0$, the critical bed residence time, τ_c is inversely proportional to k_v :

$$\tau_c = \frac{1}{k_v} \ln \left(\frac{C_0}{C_x} \right) \quad (4.8)$$

Based on this equation, the change in τ_c should track the change in k_v . Based on the

corrections factors applied to k_v , the expected bed residence times were 3 msec for benzene, 4 sec for heptane, and 4 for toluene. With the exception of toluene, τ_c increased as expected from Equation 4.8. The τ_c found for the mixtures exhibited no change for benzene when in a mixture, and lengthened for tol/ben (7 msec), tol/hep (7 msec) and heptane (from 2 mec to 4 msec). The critical bed residence times increased accordingly with the increase in k_v for heptane, but for toluene, in both mixtures, τ_c increased beyond the expected 15%. The only explanation for why this change occurs is it is due to the decrease W_e as well as the decrease in k_v . This, however, implies that τ_c is not solely dependent on k_v as seen in Equation 4.8, but dependent on W_e as well. The deviation from the expected critical bed residence time occurred only for toluene and if τ_c is dependent on W_e as well, one would expect a similar deviation for the other two vapors, and for that there is no explanation.

Practical Implications

The mixture analysis presented here reveals implications of modeling mixtures on miniature adsorbent beds as well as implications of flow rate changes with these small beds. Using the MPM to correct for W_e in mixtures in combination with the correction factors proposed by Wood for respirator cartridges is a poor combination for modeling mixtures on small-bed preconcentrators. The results obtained using these models, based on the single vapor analysis, did not accurately reflect the experimental data. In fact, errors were found to be up to 62% in some flow rate ranges. This means that using single vapor models to predict breakthrough performance of mixtures is not possible.

Additionally, mixtures exhibited a less severe dependence on flow rate (bed

residence time) at bed residence times longer than 15 msec. This means that in a mixture, changes in flow rate are not as detrimental to breakthrough volume analysis as with a single vapor. While flow rate changes do not impact the final breakthrough volume of the mixture to the same extent as a single vapor, the critical bed residence time of the mixture occurs at a longer bed residence time (higher flow rate) than the single vapor. With the exception of benzene, whose critical bed residence time did not change, the critical bed residence time increased by at least 15%. For heptane, τ_c occurs at 4 msec (104 mL/min) in a mixture, whereas the τ_c is 2 msec (190 mL/min) for the single vapor. For toluene, τ_c occurs at 7 msec (50 mL/min) in a mixture vs. 2 msec (190 mL/min) for the single vapor. Operating at these flow rates result in immediate breakthrough and should be avoided. As seen from this analysis, incorporating a second vapor in the flow rate analysis results in increased flow rate limits. It is anticipated that with higher order mixtures this increase in the critical flow rate would increase even further.

For a mixture of toluene and heptane, the flow rate limit would be 50 mL/min to capture both vapor quantitatively. This also means that at 50 mL/min, 1.37 mg of Carbopack X is the critical bed mass, and the critical bed length is 0.36 mm, the dimensions of the bed used in this study. For a mixture of benzene and toluene, the same limits apply in order to capture both vapors, since the critical bed residence time of benzene is actually lower than that of toluene. These represent real limitations in operating and constructing preconcentrators for field-deployable instruments.

Conclusions

This study presented a series of data investigating the effect of binary mixtures on

the breakthrough volume of a PCF. Models that were previously published for mixtures on larger adsorbent beds were applied to the data collected here. The trends observed for single vapors with regard to breakthrough volume and bed residence time were maintained for the binary mixture, although with less dependence of breakthrough volume on bed residence time was observed with the binary mixtures. A greater influence of bed residence time on breakthrough volume was observed for times shorter than 15 msec. The decreased sharpness in the curves suggests that in a mixture, bed residence time is not likely to be the limiting factor. The decrease of breakthrough volume (adsorption capacity) from single vapors to binary mixtures is likely to be a greater factor.

Using the Molar Proportionality Model, W_e was determined for each vapor in the binary mixture based on previously measured W_e values for the single vapors. The binary mixtures examined here resulted in a mole fraction of about 0.5, which when used in the Molar Proportionality Method, decreases the W_e value by 50%. However, in a more complex mixture, the mole fraction is expected to decrease, which will in turn cause a greater decrease in W_e as well.

Since k_v was calculated for single vapors, we were able to use the Wheeler model to determine prediction curves for breakthrough volume versus bed residence time. Using the correction factors Wood observed with k_v for single vapors and k_v for mixtures and the fractioned W_e , the Wheeler model was shown to fit the breakthrough data for mixtures. While the model followed the general trends of the data, the deviations observed between experiment and model were large and demonstrated poor agreement between data and experiment. For this reason, this method is not recommended for predicting the breakthrough volume of binary mixtures. Using single vapor breakthrough

analysis to determine mixture breakthrough, while qualitatively correct does not provide an accurate measure of breakthrough volumes and should be avoided.

Table 4-1. Values of W_e for single vapors and mixtures are given along with the mole fraction used to calculate the W_e for the mixture. The correction factor used for k_v , as well as the errors and standard deviation of the model is also shown.

Vapor/covapor	W_e^a	x_i^b	W_e^c	k_v correction	Error		Stdev ^e
	$\mu\text{g/g}$		$\mu\text{g/g}$		Average	Range	
Benzene/Toluene	410	0.25	110	1.0	-31	-66 - 2.5	0.25
Toluene/Benzene	1500	0.71	1100	0.85	6.5	-68 - 46	0.48
Toluene/Heptane	1500	0.56	860	0.85	-11	-68 - 32	0.41
Heptane/Toluene	790	0.44	340	0.85	-29	19 - 37 ^d	0.076

^a W_e values determined by gravimetric analysis for the single vapors; ^b the mole fraction used to determine the W_e for the mixture; ^c W_e values determined from Equation 4.5 using the mole fraction listed in the second column; ^d values given as absolute value since the entire model underestimated the values of V_b ; ^e standard deviation in the errors.

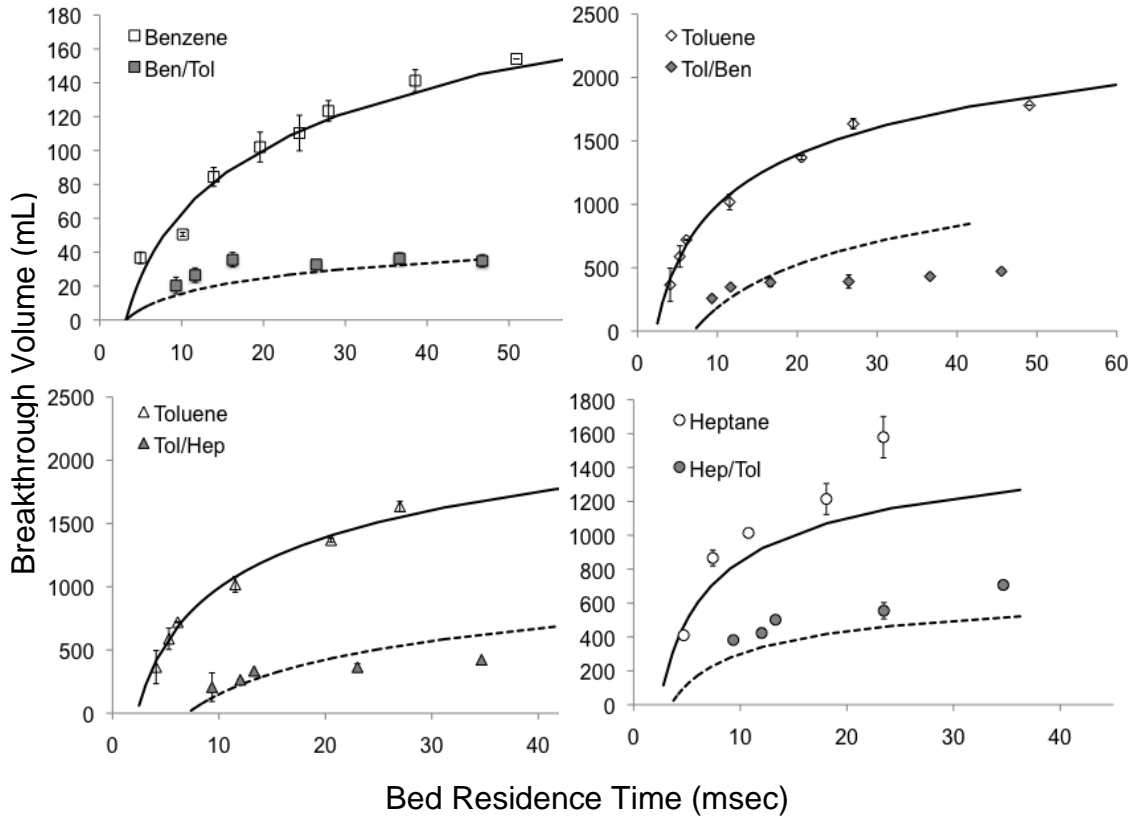


Figure 4-1. Breakthrough volumes over a range of bed residence times for single vapors (open symbols) and binary mixtures (filled symbols). Solid line shows the Wheeler model prediction for single vapors while the dashed line shows the Wheeler model prediction for binary mixtures using Equation 4.5 to determine W_e and Wood's observations for k_v for mixtures.

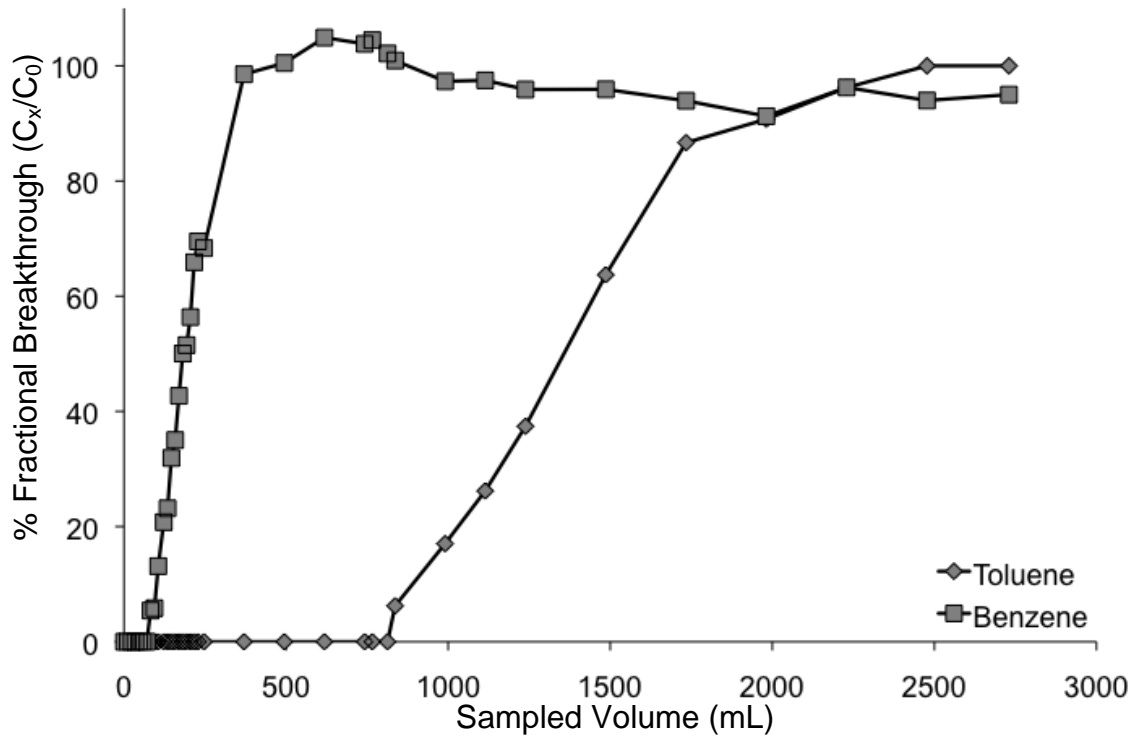


Figure 4-2. Example breakthrough curve of benzene and toluene in a mixture at similar concentrations (114 and 100 ppb, respectively). A moderate flow rate was chosen, corresponding to 18 msec. Notice that benzene reaches ~120% toluene is approaching 10% breakthrough indicating roll-up.

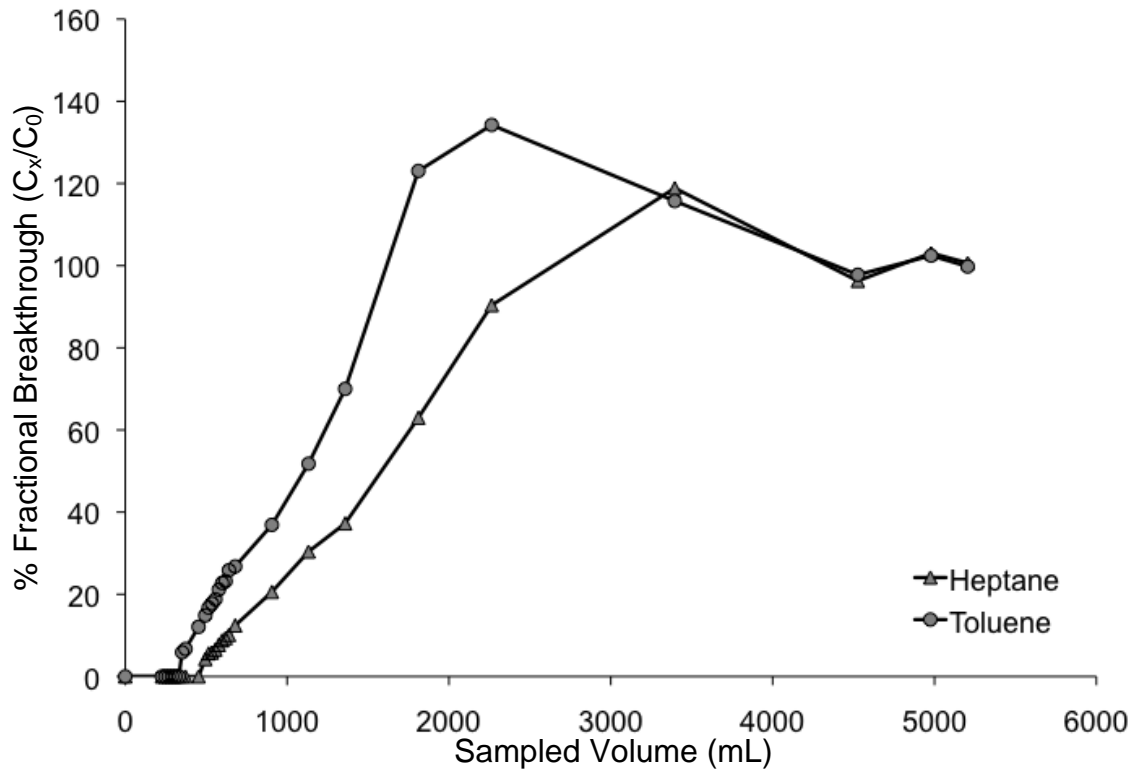


Figure 4-3. Example breakthrough curve of heptane and toluene at similar concentrations (100 and 90 ppb, respectively) at a flow rate corresponding to 18 msec. Both vapors achieve roll-up, but not until after each has reached 10% breakthrough.

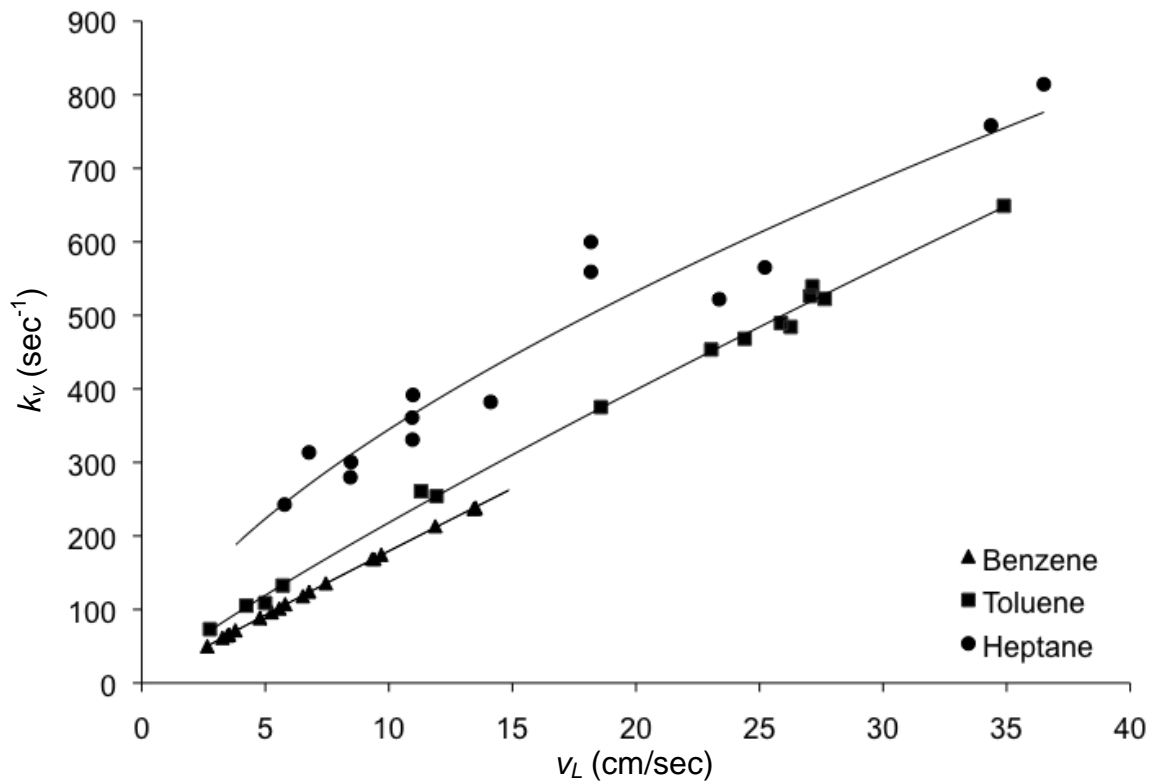


Figure 4-4. Benzene, toluene, and heptane exhibit similar shapes of curves for k_v vs. v_L . The power regressions obtained from this data were fit to the form of Equation 4.3 and used to model the single vapor breakthrough data, while correction factors were applied to these equations to provide the k_v values used to model the binary mixture breakthrough data.

References

- [1] S. C. Terry, J. H. Herman, and J. B. Angell, *IEEE Trans. Electron Dev.*, **1979**, 26, 1880.
- [2] P. R. Lewis, R. P. Manginell, D. R. Adkins, R. J. Kottenstette, D. R. Wheeler, S. S. Sokolowski, D. E. Trudell, J. E. Byrnes, M. Okandan, J. M. Bauer, R. G. Manley, and G. C. Frye-Mason, *IEEE Sensors J.*, **2006**, 6, 784.
- [3] C. J. Lu, W. H. Steinecker, W. C. Tian, M. C. Oborny, J. M. Nichols, M. Agah, J. A. Potkay, H. K. L. Chan, J. Driscoll, R. D. Sacks, K. D. Wise, S. W. Pang, and E. T. Zellers, *Lab on a Chip*, **2005**, 5, 1123.
- [4] C2V Concept to Volume, accessed online: <http://www.c2v.nl>
- [5] E. T. Zellers, W. H. Steinecker, and K. D. Wise, in *Technical Digest 2004 Solid-State Sensor and Actuator Workshop*, **2004**, pp. 61.
- [6] E. T. Zellers, S. Reidy, R. Veeneman, R. Gordenker, W. Steinecker, G. R. Lambertus, H. Kim, J. Potkay, M. P. Rowe, Q. Zhong, C. Avery, H. Chan, R. Sacks, K. Najafi, and K. Wise, in *Proc. 2007 Solid-State Sensor and Actuator Conf.-Transducers 07*, Lyon, France, **2007**, pp. 2091 - 2094.
- [7] E. T. Zellers, M. Morishita, and Q.-Y. Cai, *Sens. Actuators B*, **2000**, 67, 244.
- [8] I. Ciucanu, A. Caprita, A. Chiriac, and R. Barna, *Anal. Chem.*, **2003**, 75, 736.
- [9] J. W. Grate, N. C. Anheier, and D. L. Baldwin, *Anal. Chem.*, **2005**, 77, 1867.
- [10] S. Mitra and C. Yun, *J. Chrom. A*, **1993**, 648, 415.
- [11] C. Feng and S. Mitra, *J Chrom A*, **1998**, 805, 168.
- [12] M. Kim and S. Mitra, *J. Chrom.A*, **2003**, 996, 1.
- [13] I. Voiculescu, R. A. McGill, M. E. Zaghoul, D. Mott, J. Stepnowski, S. Stepnowski, H. Summers, V. Nguyen, S. Ross, K. Walsh, and M. Martin, *IEEE Sensors J.*, **2006**, 6, 1094.
- [14] M. Martin, M. Crain, K. Walsh, R. A. McGill, E. Houser, J. Stepnowski, S. Stepnowski, H.-D. Wu, and S. Ross, *Sens. Actuators B*, **2007**, 126, 447.
- [15] C. E. Davis, C. K. Ho, R. C. Hughes, and M. L. Thomas, *Sens. Act. B.*, **2005**, 104, 207.
- [16] R.P. Manginell, G.C. Frye-Mason, R.J. Kottenstette, P.R. Lewis, C.C. Wong,

Tech. Digest 2000 Sol.-State Sensor and Actuator Workshop, Transducers Research Foundation, Cleveland, OH, USA, **2000**, pp. 179-182.

- [17] P.R. Lewis, R.P. Manginell, D.R. Adkins, R.J. Kottenstette, D.R. Wheeler, S.S. Sokolowski, D.E. Trudell, J.E. Byrnes, M. Okandan, J.M. Bauer, R.G. Manley, G.C. Frye-Mason, *IEEE Sens. J.*, **2006**, 6, 784.
- [18] C.-J. Lu and E. T. Zellers, *Anal. Chem.*, **2001**, 73, 3449.
- [19] C.-J. Lu and E. T. Zellers, *The Analyst*, **2002**, 127, 1061.
- [20] W. A. Groves, E. T. Zellers, and G. C. Frye, *Anal. Chim. A.*, **1998**, 371, 131.
- [21] W. C. Tian, S. W. Pang, C. J. Lu, and E. T. Zellers, *J. Microelectromech. Sys.*, **2003**, 12, 264.
- [22] W. C. Tian, H. K. L. Chan, C. J. Lu, S. W. Pang, and E. T. Zellers, *J. Microelectromech. Sys.*, **2005**, 14, 498.
- [23] H. K. L. Chan, S. W. Pang, R. A. Veeneman, E. T. Zellers, and M. Takei, *Proc. 2005 Solid-State Sensor and Actuator Conf.-Transducers-05*, Seoul, Korea, **2005**, pp. 2091 – 2094
- [24] R. P. Manginell, S. Radhakrishnan, M. Shariati, A. L. Robinson, J. A. Ellison, R. J. Simonson, *IEEE Sensors J.*, **2007**, 7, 1032.
- [25] G. O. Wood, *Am. Ind. Hyg. Assoc. J.*, **1994**, 55, 11.
- [26] L. A. Jonas and J. A. Rehrmann, *Carbon*, **1972**, 10, 657.
- [27] P. Lodewcky, G. O. Wood, and S. K. Ryu, *Carbon*, **2004**, 42, 1351.
- [28] G. O. Wood, *Carbon*, **2002**, 40, 685.
- [29] C. A. Robbins, P. N. Breysse, *Am. Ind. Hyg. Assoc. J.*, **1996**, 57, 717.
- [30] R. A. Veeneman and E. T. Zellers, *Carbon*, submitted.
- [31] P. Lodewyckx and E. F. Vansant, *Am. Ind. Hyg. Assoc. J.*, **2000**, 61, 501.
- [32] G. O. Wood and P. Lodewcky, *Am. Ind. Hyg. Assoc. J.*, **2003**, 64, 646.
- [33] R. A. Veeneman and E. T. Zellers, *in prep.*
- [34] L. A. Jonas, E. B. Sansone, and T. S. Farris, *Am. Ind. Hyg. Assoc. J.*, **1983**, 44, 716.

- [35] Y. H. Yoon, J. H. Nelson, J. Lara, C. Kamel, and D. Fregeau, *Am. Ind. Hyg. Assoc. J.*, **1991**, 52, 65.
- [36] Y. H. Yoon, J. H. Nelson, and J. Lara, *Am. Ind. Hyg. Assoc. J.*, **1996**, 57, 809.
- [37] Y. H. Yoon, J. H. Nelson, J. Lara, C. Kamel, and D. Fregeau, *Am. Ind. Hyg. Assoc. J.*, **1992**, 53, 493.
- [38] P. M. Swerengen and S. C. Weaver, *Am. Ind. Hyg. Assoc. J.*, **1988**, 49, 70.
- [39] H. J. Cohen, D. E. Briggs, and R. P. Garrison, *Am. Ind. Hyg. Assoc. J.*, **1991**, 52, 34.
- [40] G. O. Nelson and C. A. Harder, *Am. Ind. Hyg. Assoc. J.*, **1976**, 37, 514.
- [41] N. Vahdat, P. M. Sweargen, and J. S. Johnson, *Am. Ind. Hyg. Assoc. J.*, **1994**, 55, 909.
- [42] N. Vahdat, *Carbon*, **1997**, 35, 1545.
- [43] G. O. Wood, *Carbon*, **2002**, 40, 231.
- [44] L. A. Jonas and J. A. Rehrmann, *Carbon*, **1974**, 12, 95.

Chapter 5

Conclusions

Summary of Dissertation

This dissertation presented the characterization of adsorbent materials for use in a microfabricated vapor preconcentrator/focuser (μ PCF). Fundamental thermodynamic measurements as well as applications of a μ PCF were presented in the context of classical models of adsorption (Dubinin-Radushkevich isotherm model) and kinetics (Wheeler model). This is the first time the Dubinin-Radushkevich model has been applied to organic vapors in the concentration range of interest for typical applications of the μ GC (low parts-per-billion to parts-per-trillion). The Wheeler model, while widely used for predicting the service life of respirator cartridges, had not been applied to μ PCFs typically employed in portable instruments.

In Chapter 2 we showed the value of applying classical thermodynamic models of adsorption to the low concentration ranges found in typical applications of the WIMS μ GC and μ PCF. We chose to use the Dubinin-Radushkevich isotherm model (DR) to examine a range of volatile organic compounds (VOCs) on two graphitized carbons commonly used in the μ PCF. The DR model gives adsorption capacity as a function of adsorbent (micropore volume and adsorption energy) and adsorbate (analyte density and

vapor pressure) properties. Our initial attempts at applying the DR model were unsuccessful, as the model did not accurately reflect the adsorption phenomenon observed with VOCs on the graphitized carbons at the low concentration range of interest. Conventional applications of the DR model employ a single equation to describe data in parts-per-million range. However, we showed that doing so leads to significant errors between model and experiment (up to 85%) especially at low concentrations (20-500 ppb). Upon further inspection of our data, we found two distinct linear regions corresponding to higher and lower concentrations. These two linear sections were evident for all but three of the 23 vapor-adsorbent pairs examined. These two regions describe the strength of adsorbate-adsorbent interactions (at low concentrations) and adsorbate-adsorbate interactions (at higher concentrations). The two regions also yielded two values for the adsorption energy, and consequently two equations for the DR model. In general, non-polar vapors presented stronger adsorbate-adsorbent interactions (evident in the higher adsorption energy found at lower surface coverage) in comparison to polar vapors. The polar vapors generally presented stronger adsorbate-adsorbate interactions, evident in their higher energies of adsorption found at higher surface coverage. Lower energies were found at lower surface coverages for these vapors due to poor interactions of the polar vapor with a predominately non-polar surface. We hypothesized that surface heterogeneity was resulting in two distinct sites for adsorption. These different sites yielded different adsorption energies depending on the type of vapor (polar or non-polar) and the surface coverage. Once these different energies were taken into account in the model (to yield a dual energy model), agreement improved significantly, with errors less than 15%.

These results have significant impact on the amount of adsorbent mass included in the μ PCF. A poor choice of model for the adsorption capacity negatively impacts the amount of mass calculated for use in the μ PCF. For the vapors whose single energy model overestimated the adsorption capacity (largely the polar VOCs), the amount of mass incorporated in the μ PCF as a consequence would be less than needed. This would result in early breakthrough of the analytes, which complicates the desired quantitative analysis and negatively impacts the detection limits of the system and performance of the column ensemble. For the vapors whose single energy model underestimated the adsorption capacity (largely the non-polar VOCs), additional adsorbent mass would be incorporated in the μ PCF. This would lead to poor desorption efficiency, a larger injection band, and additional power required to heat the device. Because proper functioning of the μ PCF impacts the μ GC system as a whole, the detrimental impact of a poorly chosen model are not limited to operation of the μ PCF. Instead, a poorly designed μ PCF, due to inaccurate adsorption models, negatively impacts the operation of the total system.

Chapter 3 investigated the application of the Wheeler model to the μ PCF as well as a more conventionally designed capillary μ PCF. We found that when comparing the two designs, for two vapors (toluene and benzene) on a single adsorbent bed containing a graphitized carbon (Carbopack X), similar results were obtained. The similarity in results, less than 20% difference between breakthrough volumes for both vapors and both devices over a range of bed residence times, indicate that adsorbent bed geometry does not significantly impact the breakthrough performance of the device. It also allows us to conclude that using the capillary μ PCF in lieu of the μ PCF, when a microfabricated

structure is not available, will produce the same conclusions regarding adsorbent performance.

When examining breakthrough volume vs. bed residence time, a sharp dependence on bed residence time was seen at times < 15 msec. In this range, small changes in the analytical flow rate through the adsorbent bed results in large changes in breakthrough volume and μ PCF performance. For example at bed residence times shorter than 15 msec, a 50% decrease in bed residence time, results in a 50% decrease in breakthrough volume. This is in contrast to bed residence times longer than 15 msec, where the same 50% decrease results in only a 15% decrease in breakthrough volume. Operating at flow rates corresponding to bed residence times less than 15 msec results in greater sensitivity of breakthrough volume to small changes in system operation. At bed residence times of 3 msec (for toluene) and 3.5 msec (for benzene), the critical bed residence time is reached at which point breakthrough occurs immediately. This corresponds to 25 mL/min for toluene and 20 mL/min for benzene. These flow rates represent the point at which no adsorption occurs within the adsorbent bed of the μ PCF and should be avoided.

The combination of these results with the isotherms collected in Chapter 2 allowed us to determine the kinetic rate coefficient (k_v) from the Wheeler model. By plotting k_v versus the linear velocity, we fit our data to the form commonly used for respirator cartridges (Equation 1.19). While we were able to maintain the same form of the equation, we were unable to achieve the same equation for both vapors. We observed a non-linear dependence on linear velocity as predicted by Equation 1.19, but not to the same extent. Because benzene gave breakthrough volumes around 200 mL, in contrast to

toluene where breakthrough volumes were on the order of 2000 mL, the model for benzene is more sensitive to changes in k_v . This resulted in different equations of k_v for the two vapors. Similarly, the smaller linear velocities examined for benzene also contributed to the differences in the linear velocity dependence. As linear velocity increases, the boundary layer of the adsorbent material decreases which causes an increase in the nonlinearity of the rate coefficient dependence on linear velocity.

While the same equation was not achieved for both vapors, the Wheeler model was still shown to accurately reflect the data obtained for both vapors and both devices. While our model was a descriptive, not a predictive one, we found good agreement between model and data.

Binary mixtures were examined as a function of bed residence time in Chapter 4. We examined two binary mixtures on a single adsorbent bed (Carbopack X), benzene/toluene and toluene/heptane. Because we assumed the adsorption capacity per analyte to decrease by the mole fraction of the analyte in the mixture (using the Molar Proportionality Model), we were able to determine k_v as a function of linear velocity for a mixture in the same manner as Chapter 3. We observed no change in k_v for benzene in a mixture with toluene due to its early breakthrough. Since benzene was the first vapor through the adsorbent bed, it interacts with the bed as if it was a single vapor. The values of k_v for toluene in the benzene/toluene mixture decreased by 15%. For toluene and heptane, we again observed a 15% decrease in k_v for toluene (as seen with benzene) but no decrease in the k_v for heptane. It was hypothesized that this was due to the extremely non-polar nature of heptane. When using the modified Wheeler model to describe our data, we applied correction factors suggested by Wood. These correction factors

decrease k_v by 15% for compounds with similar breakthrough volumes (heptane and toluene) and compounds that breakthrough second (toluene with benzene). No correction factor is applied to k_v for vapors that breakthrough first (benzene with toluene). Using this method, we found good agreement between the model and experiment. As seen with Chapter 3, the model was a descriptive one rather than a predictive model, but our data showed good agreement with the trends predicted by Wood from the modified Wheeler model for binary mixtures.

Because we observed a decrease in breakthrough volumes for all the vapors tested, this indicates that mixture analysis must be considered when designing μ PCFs for complex mixture. With binary mixtures, the breakthrough volumes decreased nearly 4-fold for benzene and toluene and 3-fold for heptane. It is expected that this difference between breakthrough volumes would increase for mixtures beyond two vapors.

The characterization of these materials is important because it provides information vital to the design and operation of the μ PCF within the μ GC. As described in Chapter 2, the choice of model for adsorption capacity has implications for the operation of the total system. Recognizing the effect of flow rate (as it relates to bed residence time) is important in maintaining quantitative analysis as seen in Chapter 3. Lastly a systematic investigation of binary mixtures on the μ PCF, as seen in Chapter 4, adds to the body of work leading to better μ PCF design.

Future Work

While a significant body of work has been presented here, additional research is foreseen. In fact the research presented opens new avenues for future studies to further

improve preconcentrator technology. In Chapter 2, we investigated the use of the DR model to the adsorption capacity of VOCs on two graphitized carbons. The results found in Chapter 2 call into question some of the accepted theories surrounding adsorption by solids. However, since the observations we made were at very low concentration levels, it is difficult to accurately apply these previous notions.

To further understand adsorption at low concentrations, additional isotherms should be collected, focusing on two things in particular. First, additional vapors should be examined. A small test set of VOCs (23 in total) were initially examined to cover a range of vapors with different vapor pressures and chemical functionality, but a systematic investigation of a wider range of vapors with different functionality would be valuable. For example, on Carbopack B, only two alkanes were examined. To properly draw conclusions regarding the potential dependence of adsorption energy on number of carbons, additional data for other straight-chain alkanes is needed. Second, our isotherms were measured to 2000 ppb since that was the highest concentration of interest for our applications. However, in doing this, the data collected did not overlap with any data presented in literature. To further validate the results achieved with these isotherm studies, isotherms should be repeated with their concentration range extended in order to reproduce published data.

Within the context of the DR model, only two of the materials used in the μ PCF (Carbopack B and Carbopack X) were examined. However, the μ PCF often employs a third material, Carboxen 1000 to capture the highest volatility compounds. Future studies should apply a similar analysis as seen in Chapter 2 to Carboxen 1000 and other novel materials. Carboxen 1000, a high surface area, porous, carbon molecular sieve would

undoubtedly exhibit different adsorption behavior in comparison to the two nominally non-porous graphitized carbons. It also provides a unique challenge to isotherm collection since it adsorbs water, unlike Carbopack B and X, which are hydrophobic. Toward that end, additional precautions would have to be taken in order to prevent humidity from entering the test atmosphere for initial experiments. Eventually, since these materials are intended for real world use, humidity effects would also need to be investigated.

Carbon nanotubes (CNTs) also provide an interesting avenue for additional studies. A recent collaboration with Professor Hart demonstrated the ability to pattern CNT growth. This makes them ideal candidates for μ PCFs since they have the potential to be grown, in patterns, within a microfabricated device. CNTs can not be packed as densely as graphitized carbons or other granular carbons because they can prohibit flow through the device. However, patterning their growth allows for a dense population of small CNT “forests” that adsorb vapors within the μ PCF structure without inhibiting the flow. The accessibility of the inner layers of these multi-walled CNTs has yet to be seen; however, they have potential for higher adsorption capacity than previously examined graphitized carbons.

Mixtures, as seen in Chapter 4, also warrant future studies. Here, we presented data for two binary mixtures. Ideally, the results observed for these two test cases would be reproduced with additional binary mixtures. Investigating binary and higher order mixtures on the basis of similarity or difference in molecule size, functionality, and vapor pressure would provide relevant data for the μ PCF and aid in characterization of the selectivity of the adsorbent materials. Likewise, modeling with these mixtures is an

important aspect for μ PCF design since it is unlikely that applications would consist of a single vapor. We showed that the Wheeler model was applicable to binary mixtures, provided correction factors were applied. The published study providing these correction factors showed significant standard deviations. To provide accurate modeling results for mixture analysis, these correction factors must be verified for a larger set of mixtures.

Lastly, the studies presented here did not explore the desorption process for μ PCFs. This, however, is an important aspect of preconcentrator operation since it affects the analytical capabilities of the entire system. The effect of desorption temperature on the recovery of trapped vapors and the injection band should be investigated to provide a lower temperature limit for μ PCF desorption. The heating rate of the μ PCF is another important variable to characterize. Ideally, the heating rate should be maximized to provide the narrowest injection band possible. However, the effect of this rate on the total power consumption of this system must also be considered. Since the μ GC is to be ultimately battery powered, the total power available for operation of the μ PCF will be limited. Therefore, for final implementation, the desorption heating rate should be optimized for both narrow injection bands and total power consumption. To aid in this achievement, different flow rates, split operation, and pulsed flow methods should also be explored.

This dissertation focused on the characterization of adsorbent materials as they impact the design and operation of μ PCFs and the μ GC and adds to the body of work on μ PCFs and adsorbent materials. Notable results were found pertaining to the thermodynamic and kinetic factors influencing the design and operation of such devices.

This document provides useful information to not only introduce preconcentration to the uninitiated but also to facilitate the optimal performance of future μ PCFs and μ GCs.

Appendix

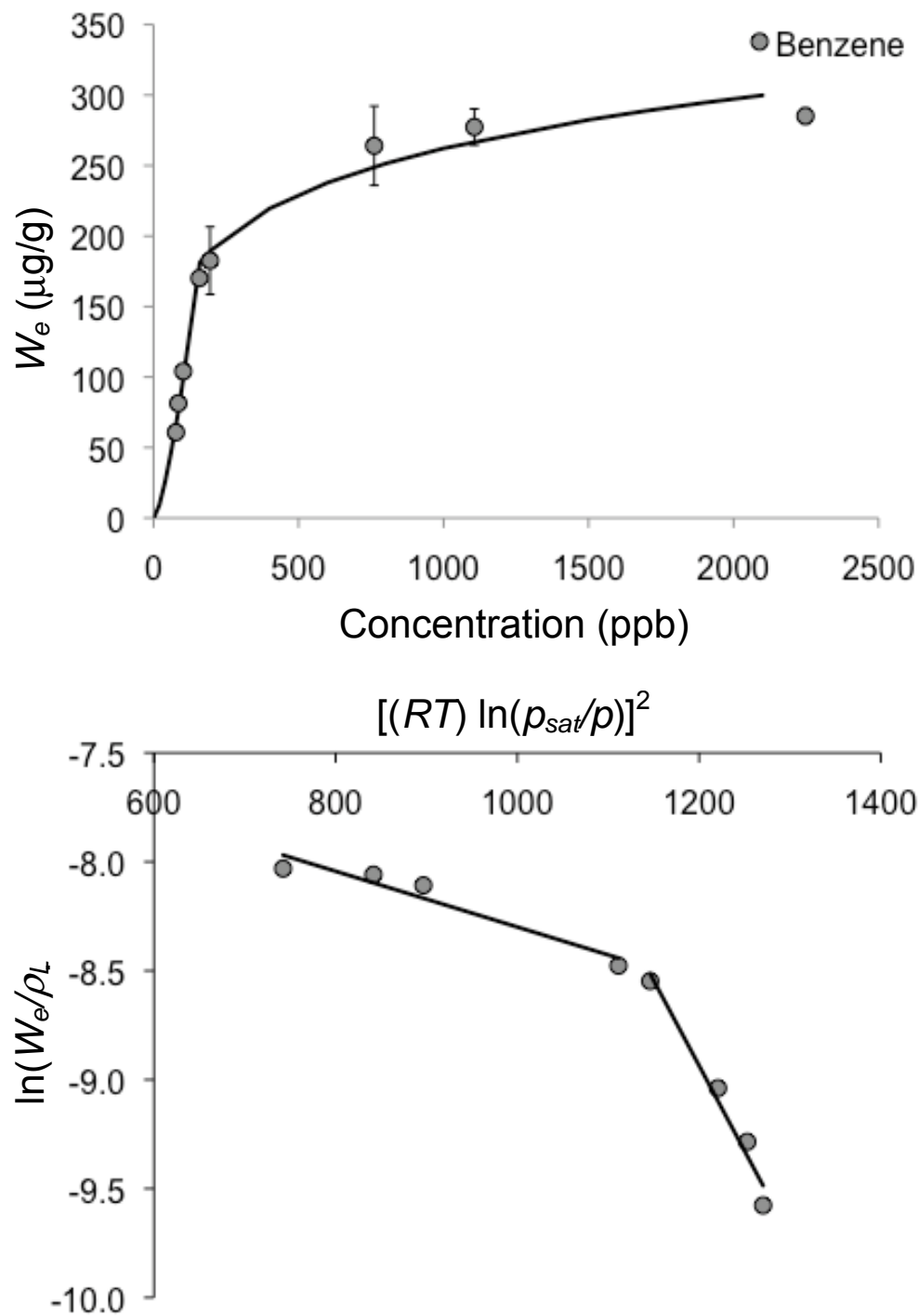


Figure A-1. The isotherm for benzene on Carbo-pack B with the DR modeling result using two energies is shown (top). The linearized isotherm is shown at the bottom indicating the two regions of adsorption yielding two values of E_o .

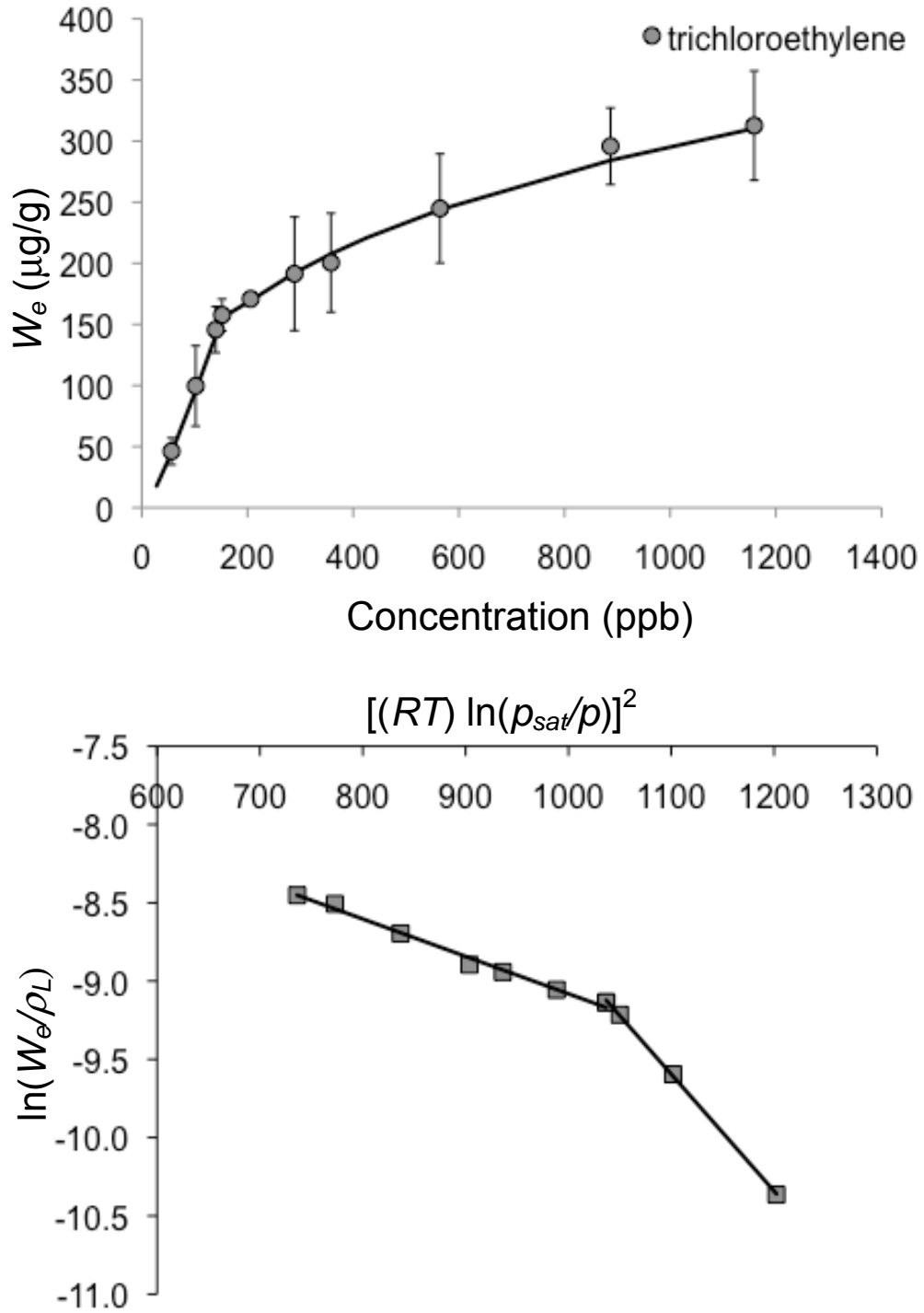


Figure A-2. The isotherm for trichloroethylene on Carbo-pack B with the DR modeling result using two energies is shown (top). The linearized isotherm is shown at the bottom indicating the two regions of adsorption yielding two values of E_o .

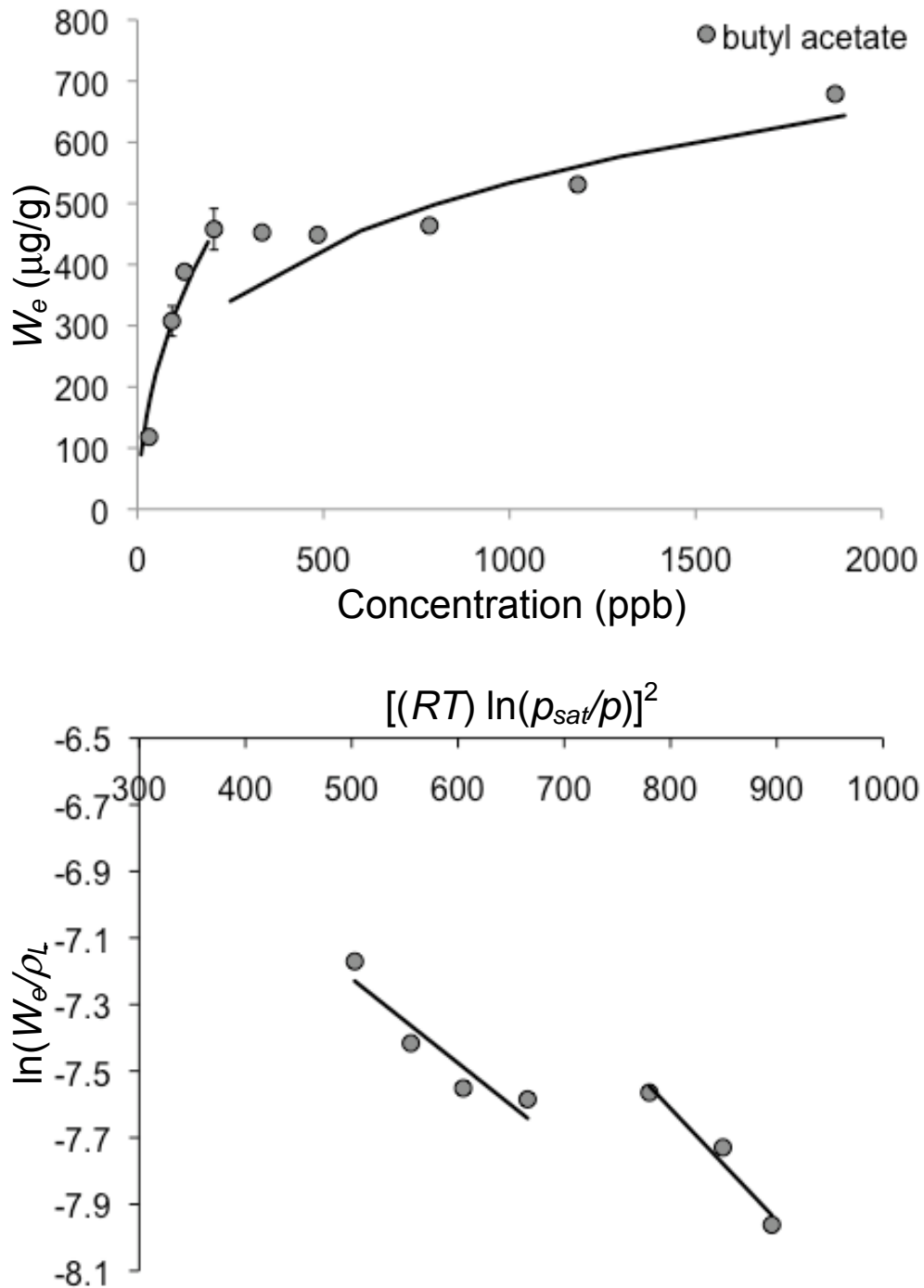


Figure A-3. The isotherm for butyl acetate on Carbpacck B with the DR modeling result using two energies is shown (top). The linearized isotherm is shown at the bottom indicating the two regions of adsorption yielding two values of E_o .

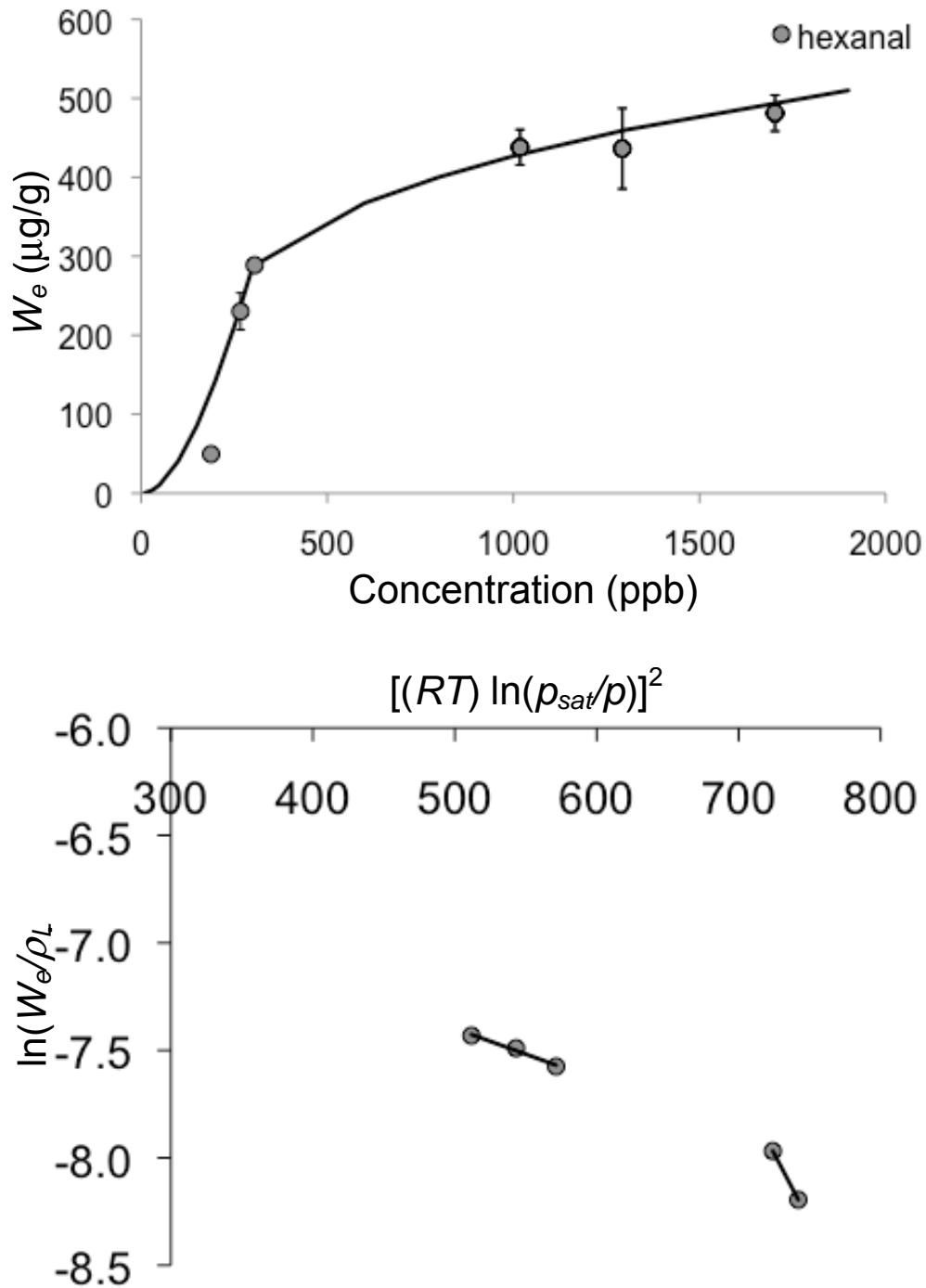


Figure A-4. The isotherm for hexanal on Carbpacck B with the DR modeling result using two energies is shown (top). The linearized isotherm is shown at the bottom indicating the two regions of adsorption yielding two values of E_o .

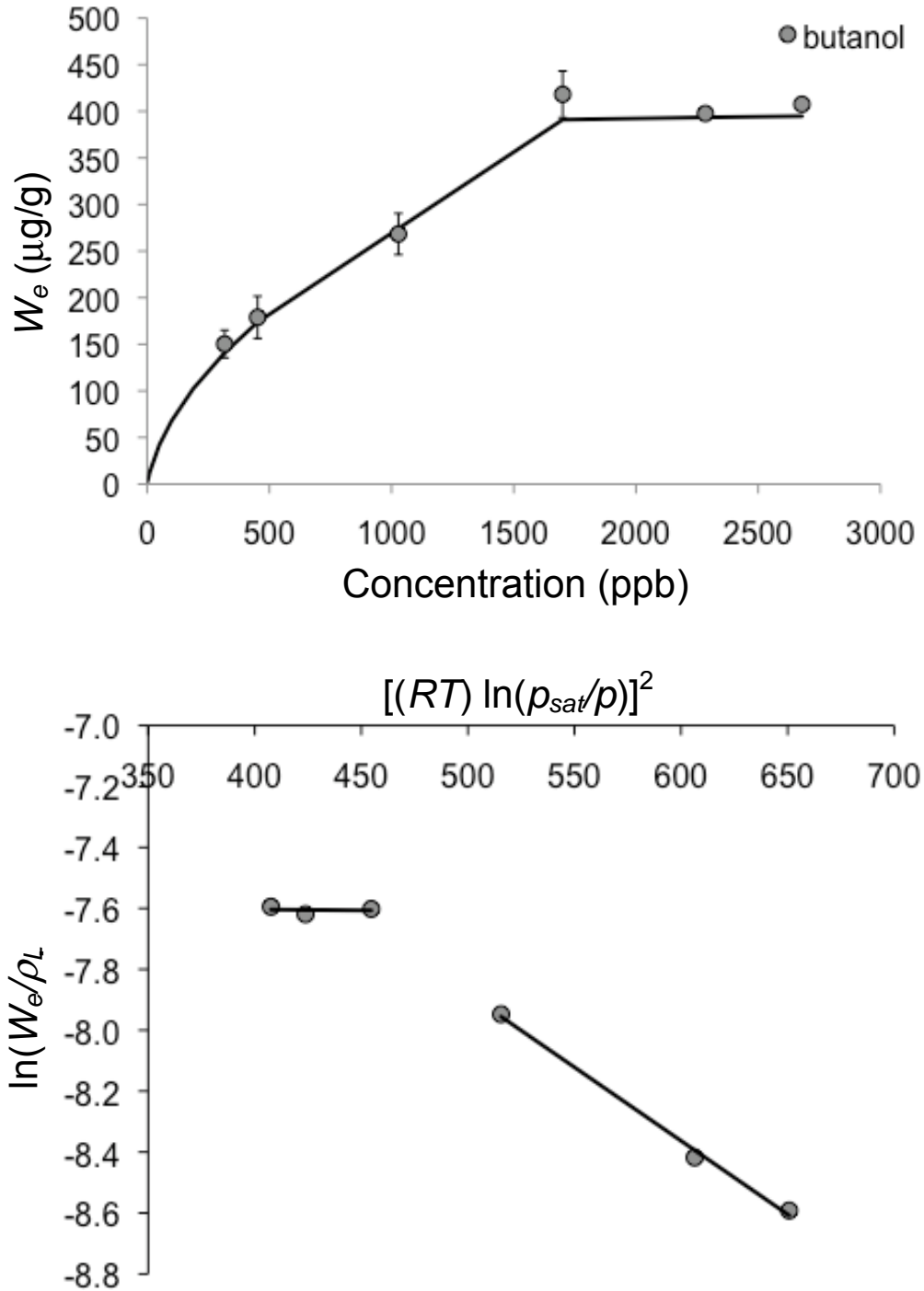


Figure A-5. The isotherm for butanol on Carbopack B with the DR modeling result using two energies is shown (top). The linearized isotherm is shown at the bottom indicating the two regions of adsorption yielding two values of E_o .

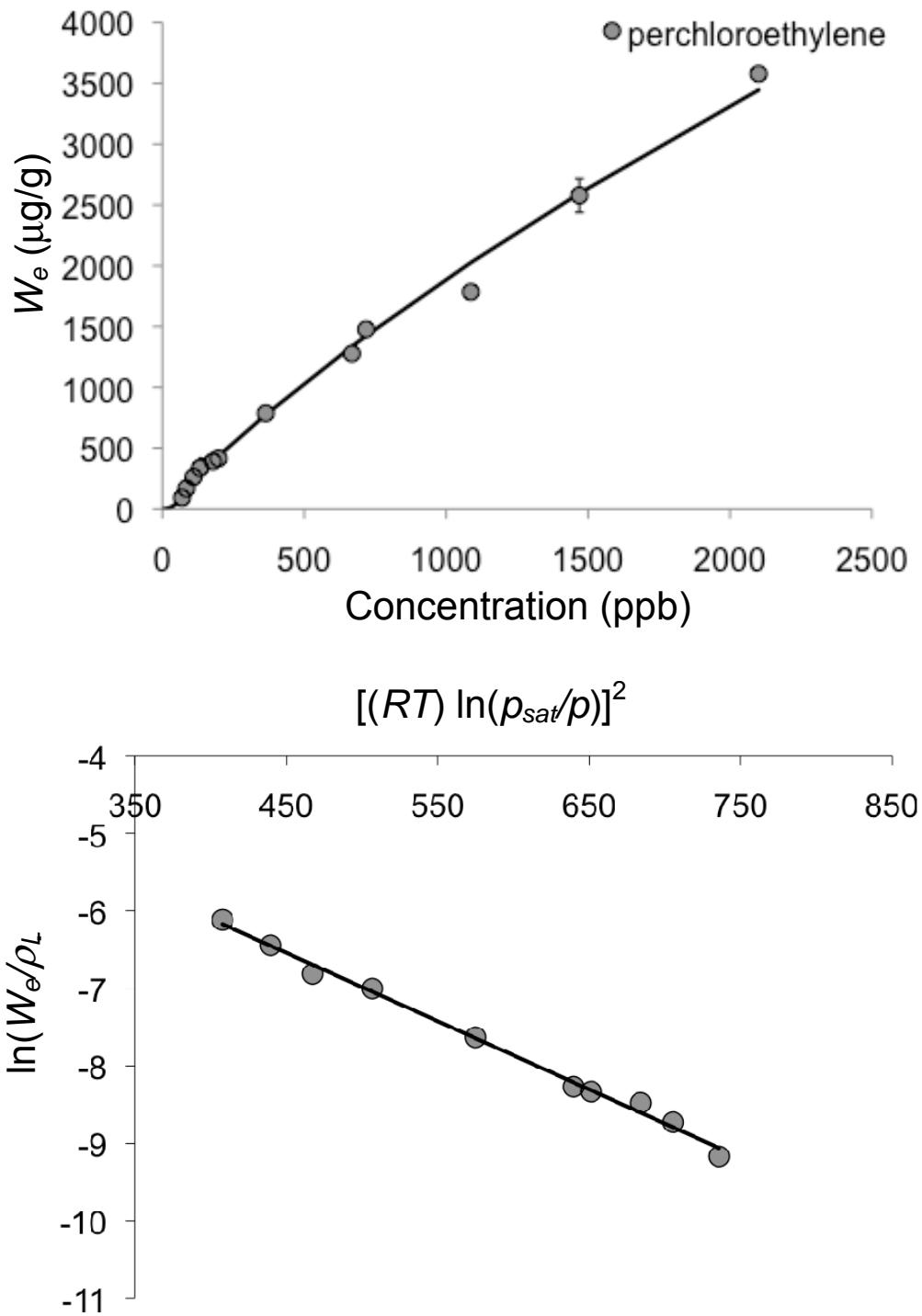


Figure A-6. The isotherm for perchloroethylene on Carbopack B with a single DR equation model (top). The linearized isotherm is shown at the bottom indicating the range of linearity yielding a single value for E_o .

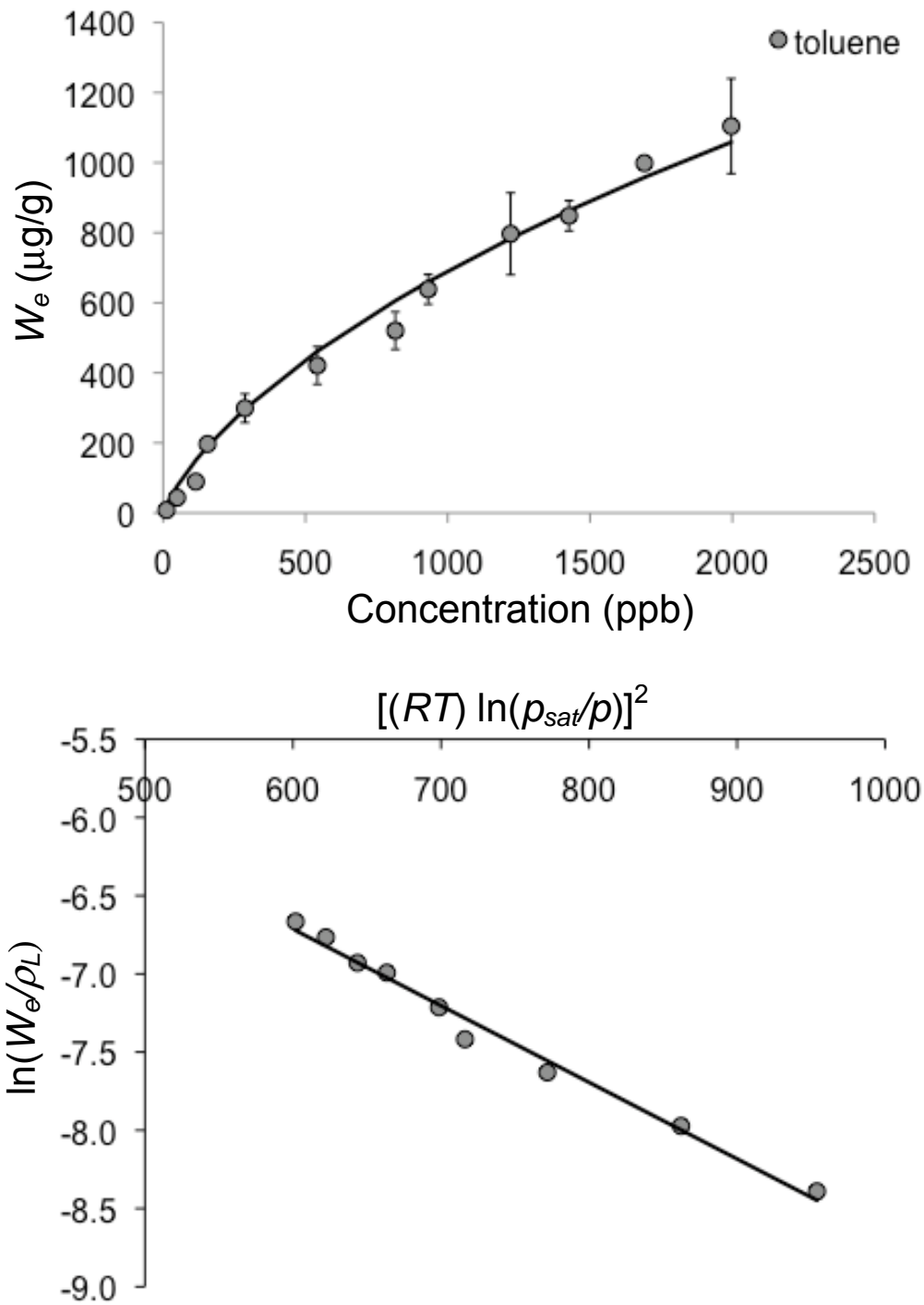


Figure A-7. The isotherm for toluene on Carboxpack B with a single DR equation model (top). The linearized isotherm is shown at the bottom indicating the range of linearity yielding a single value for E_o .

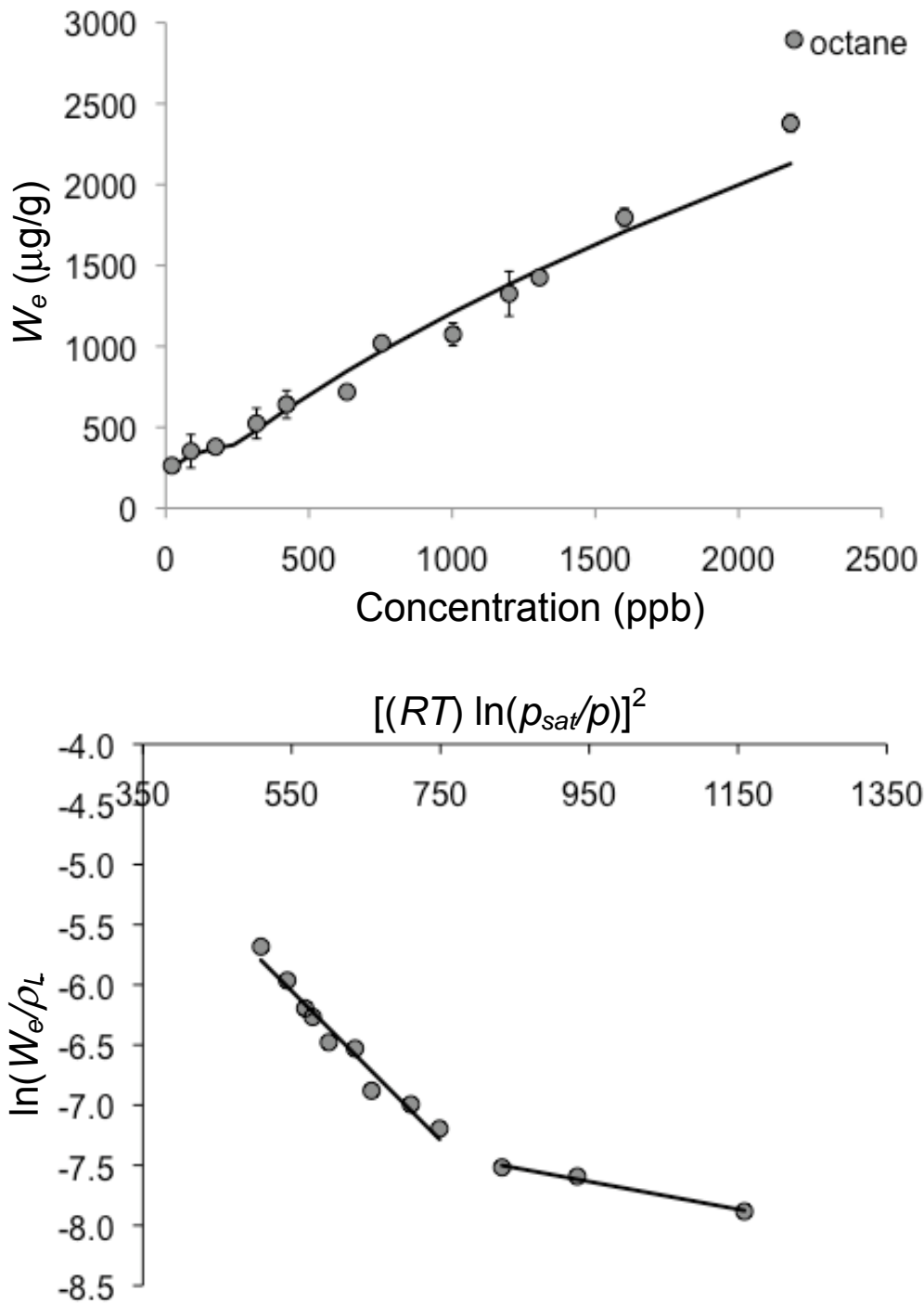


Figure A-8. The isotherm for octane on Carboxpack B with the DR modeling result using two energies is shown (top). The linearized isotherm is shown at the bottom indicating the two regions of adsorption yielding two values of E_o .

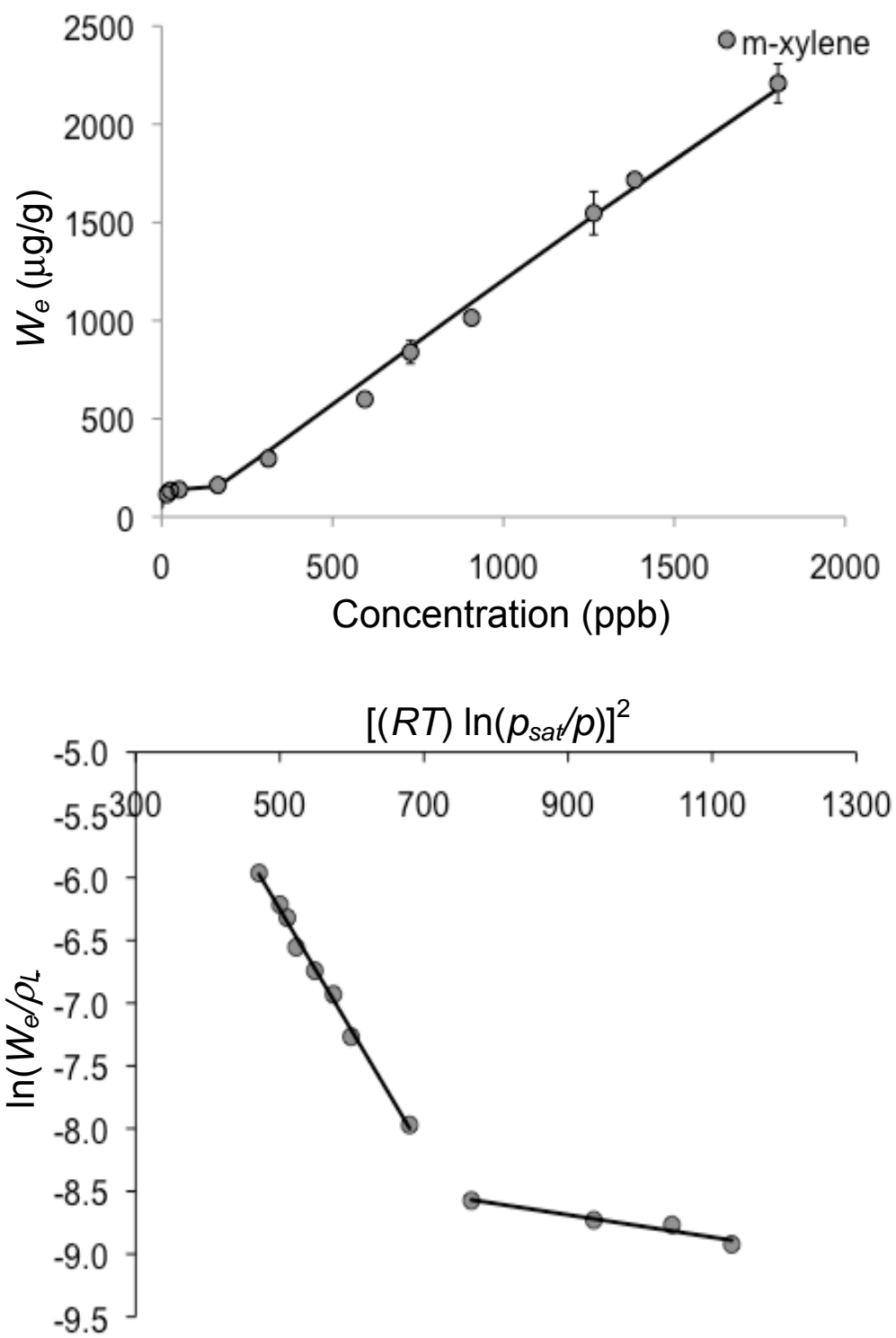


Figure A-9. The isotherm for m-xylene on Carbopack B with the DR modeling result using two energies is shown (top). The linearized isotherm is shown at the bottom indicating the two regions of adsorption yielding two values of E_o .

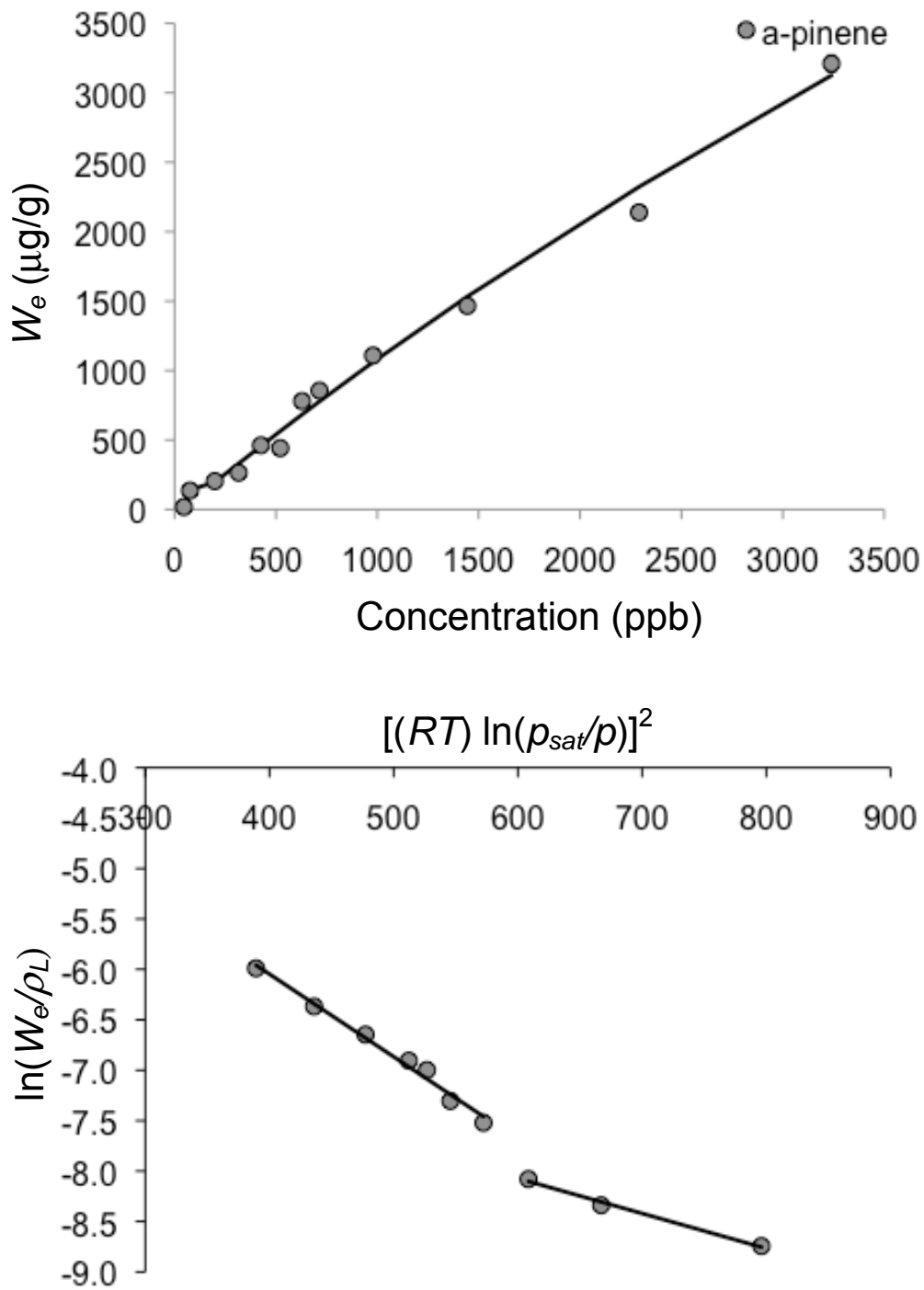


Figure A-10. The isotherm for α -pinene on Carboxpack B with the DR modeling result using two energies is shown (top). The linearized isotherm is shown at the bottom indicating the two regions of adsorption yielding two values of E_o .

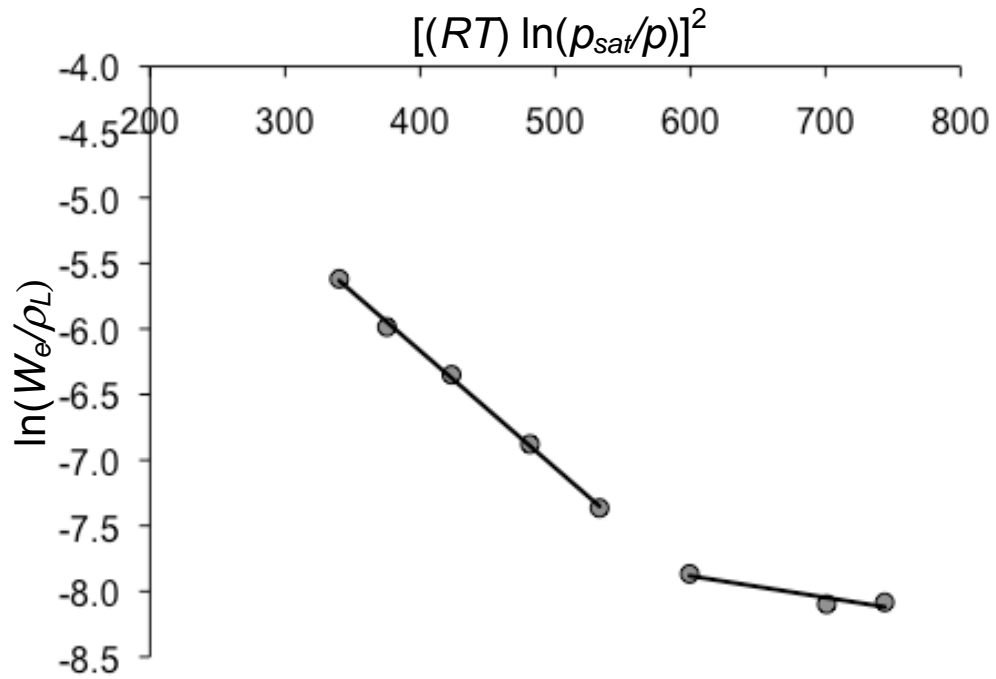
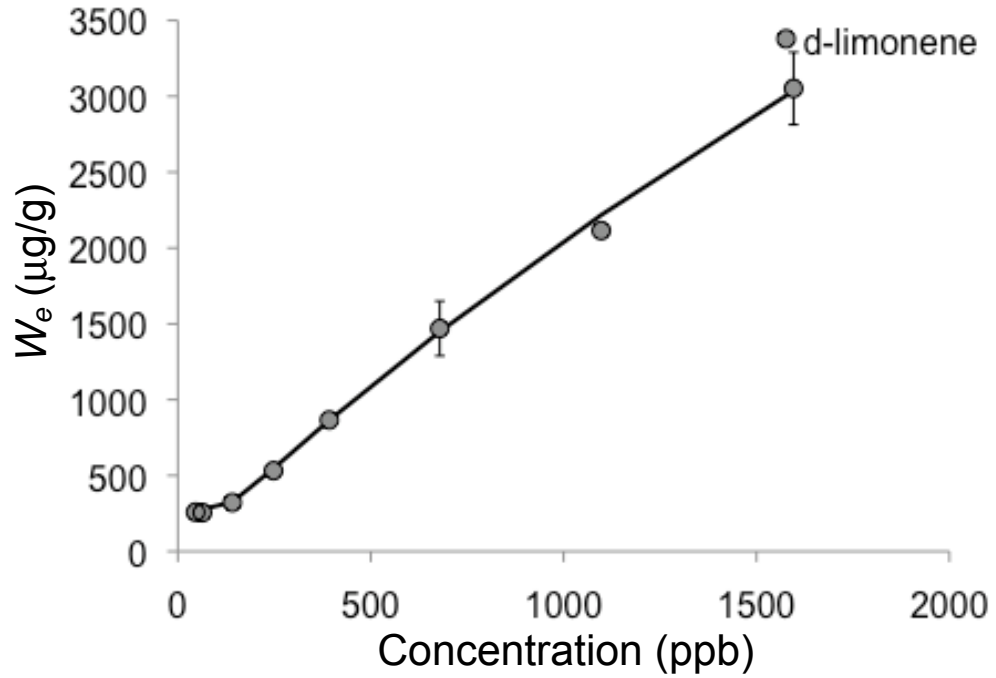


Figure A-11. The isotherm for d-limonene on Carbpac B with the DR modeling result using two energies is shown (top). The linearized isotherm is shown at the bottom indicating the two regions of adsorption yielding two values of E_o .

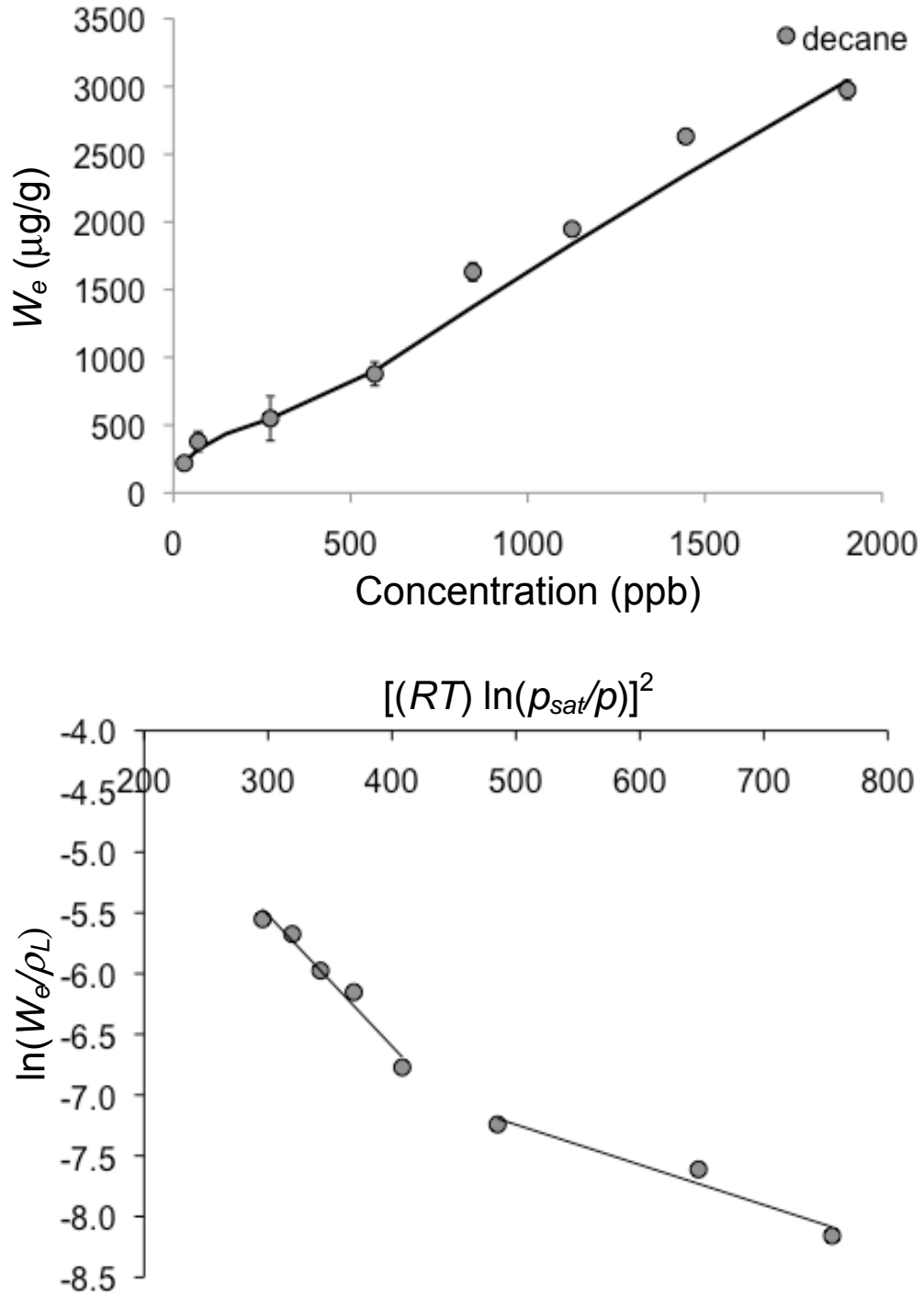


Figure A-12. The isotherm for decane on Carboxpack B with the DR modeling result using two energies is shown (top). The linearized isotherm is shown at the bottom indicating the two regions of adsorption yielding two values of E_o .

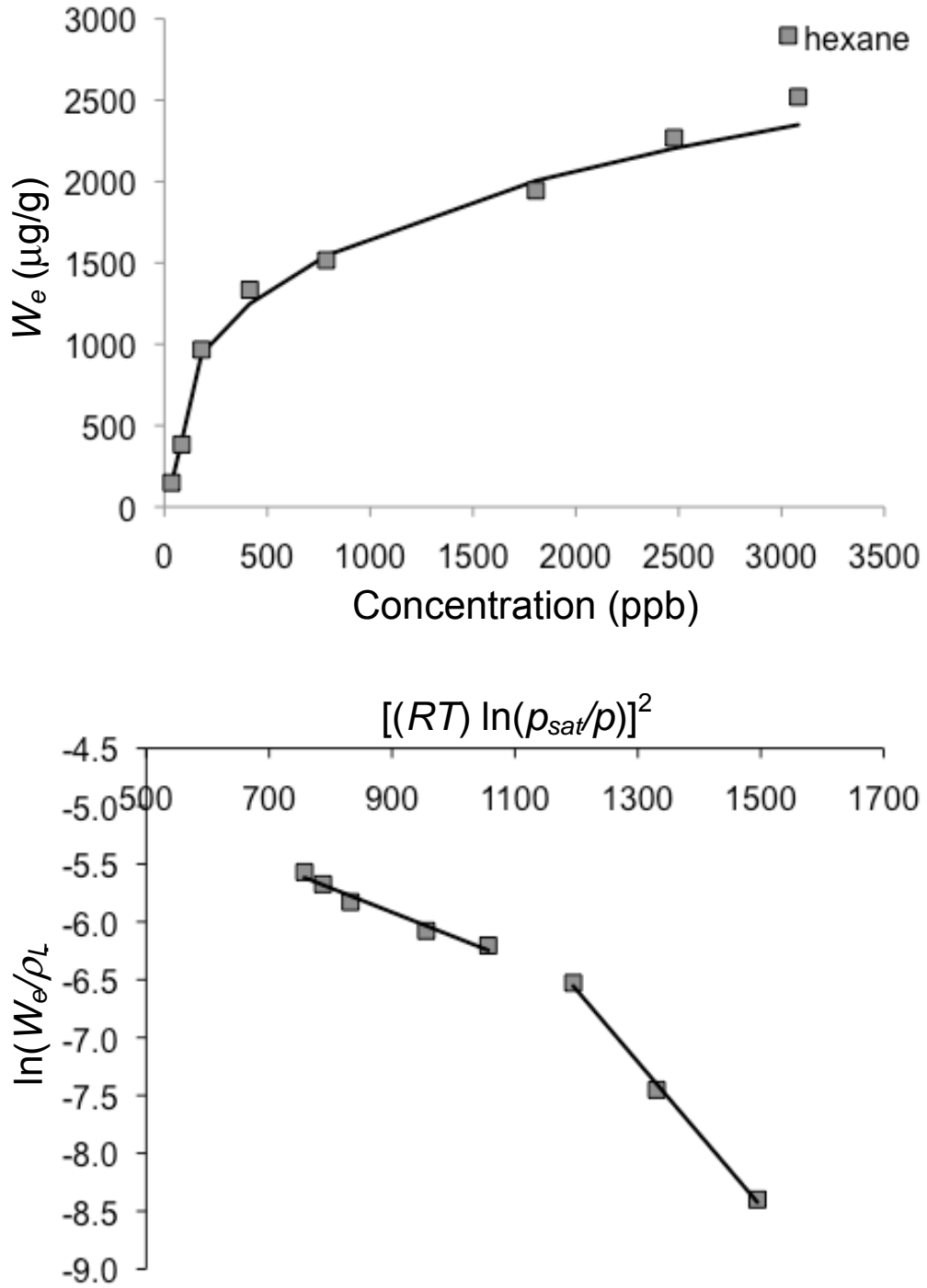


Figure A-13. The isotherm for hexane on Carpack X with the DR modeling result using two energies is shown (top). The linearized isotherm is shown at the bottom indicating the two regions of adsorption yielding two values of E_o .

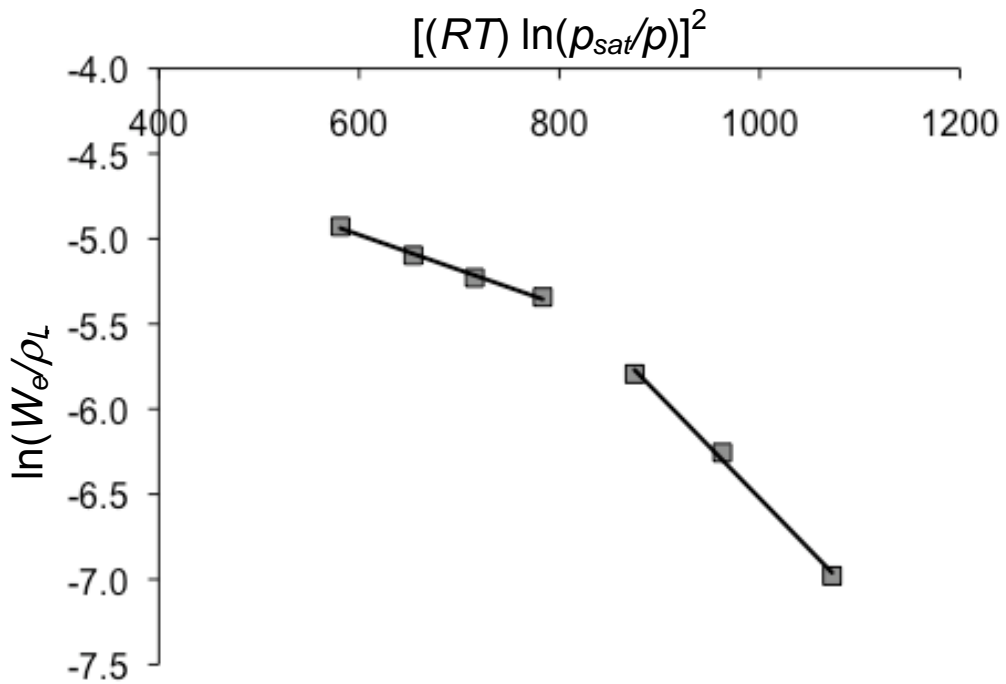
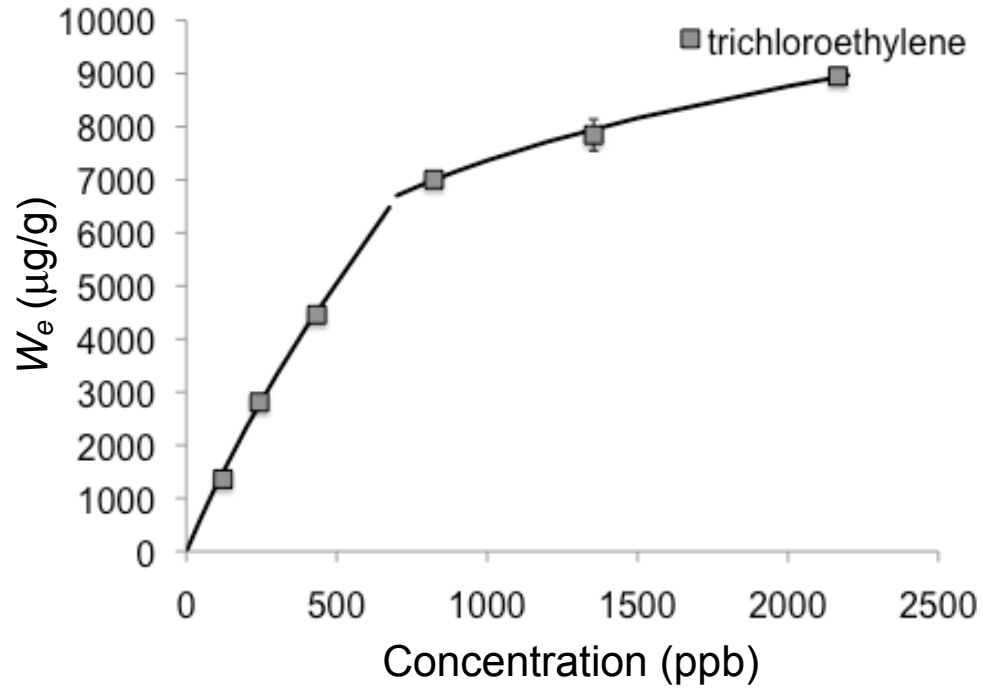


Figure A-14. The isotherm for trichloroethylene on Carbopack X with the DR modeling result using two energies is shown (top). The linearized isotherm is shown at the bottom indicating the two regions of adsorption yielding two values of E_o .

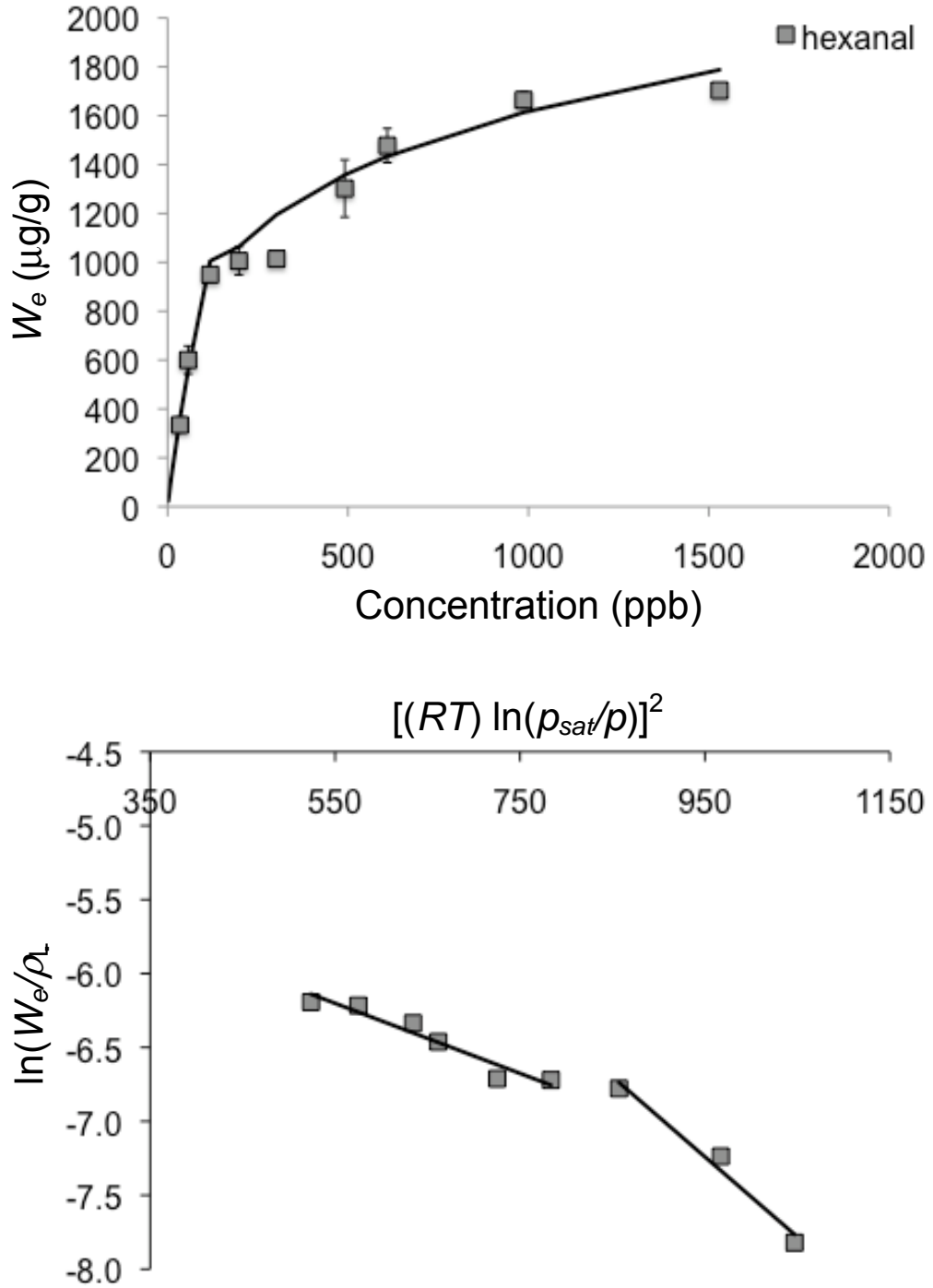


Figure A-15. The isotherm for hexanal on Carbpacck X with the DR modeling result using two energies is shown (top). The linearized isotherm is shown at the bottom indicating the two regions of adsorption yielding two values of E_o .

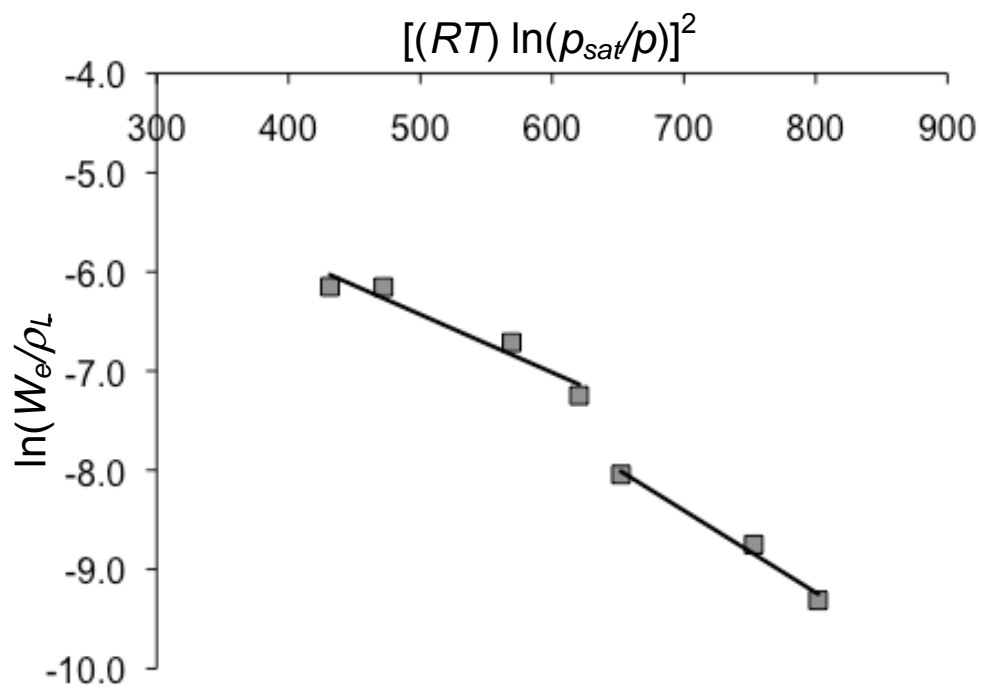
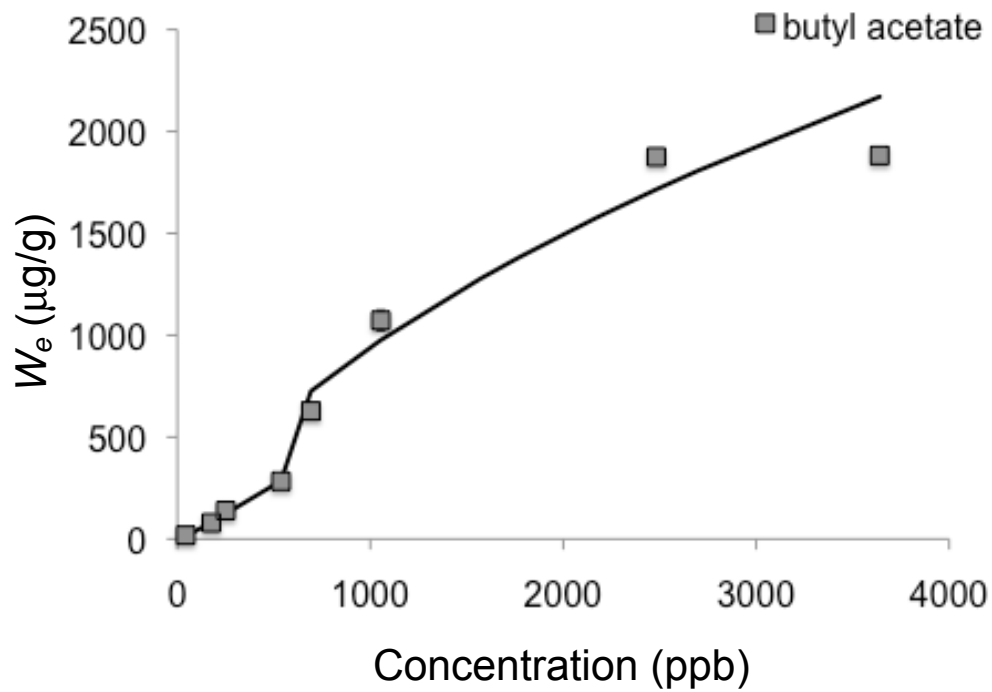


Figure A-16. The isotherm for butyl acetate on Carpack X with the DR modeling result using two energies is shown (top). The linearized isotherm is shown at the bottom indicating the two regions of adsorption yielding two values of E_o .

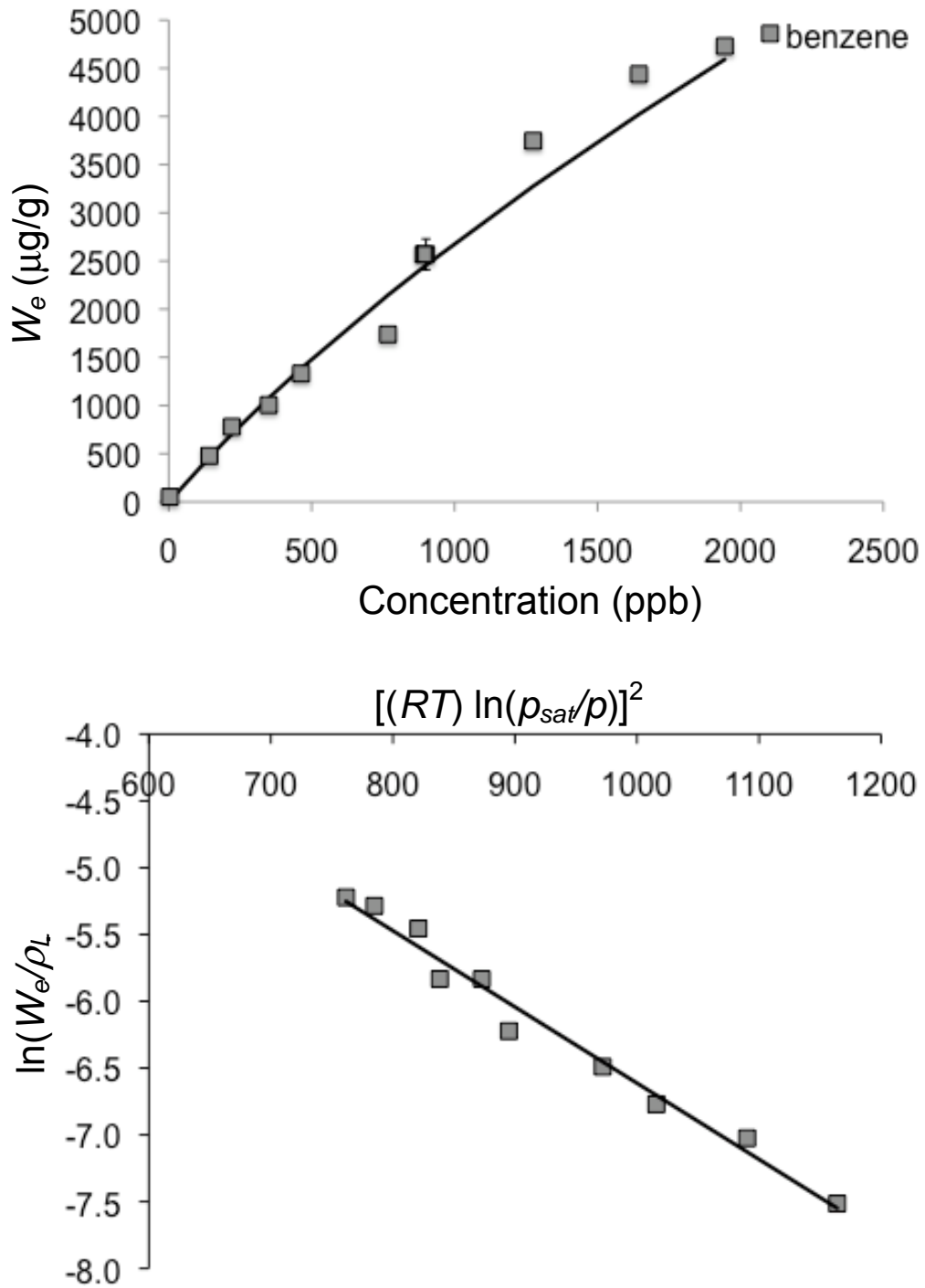


Figure A-17. The adsorption isotherm for benzene on Carbopack X with the DR modeling result from a single linear regression is shown (top). The linearized isotherm is shown at the bottom indicating the single linear region yielding a single E_o value.

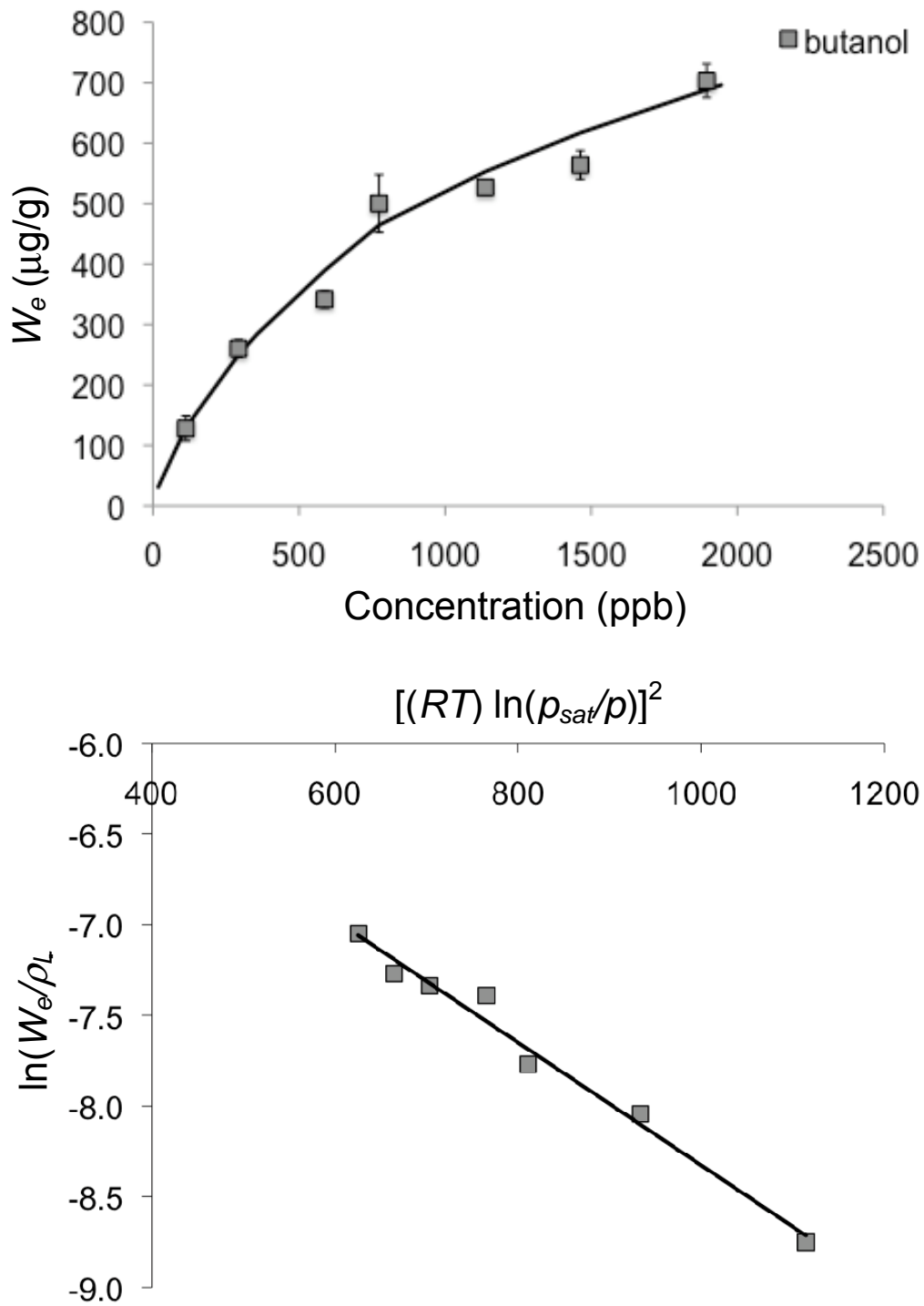


Figure A-18. The adsorption isotherm for butanol on Carbopack X with the DR modeling result from a single linear regression is shown (top). The linearized isotherm is shown at the bottom indicating the single linear region yielding a single E_o value.

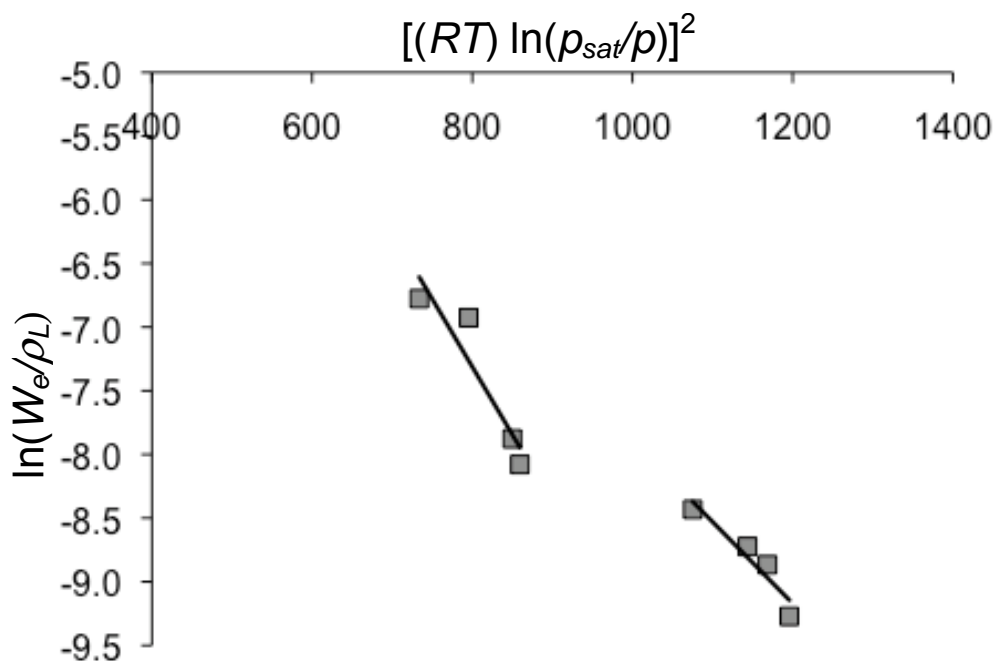
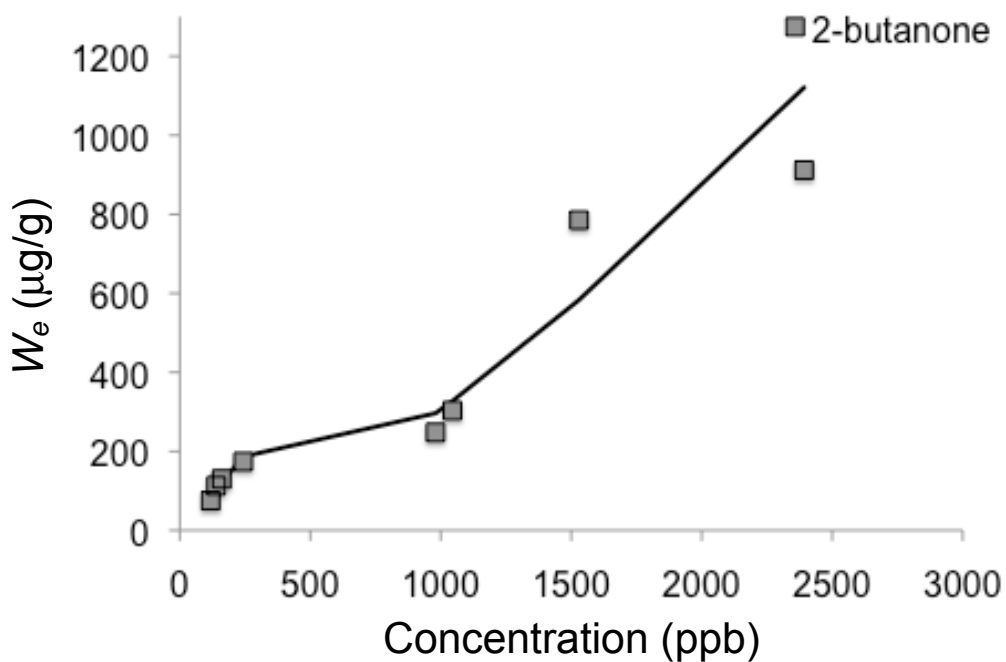


Figure A-19. The isotherm for 2-butanone on Carpack X with the DR modeling result using two energies is shown (top). The linearized isotherm is shown at the bottom indicating the two regions of adsorption yielding two values of E_o .

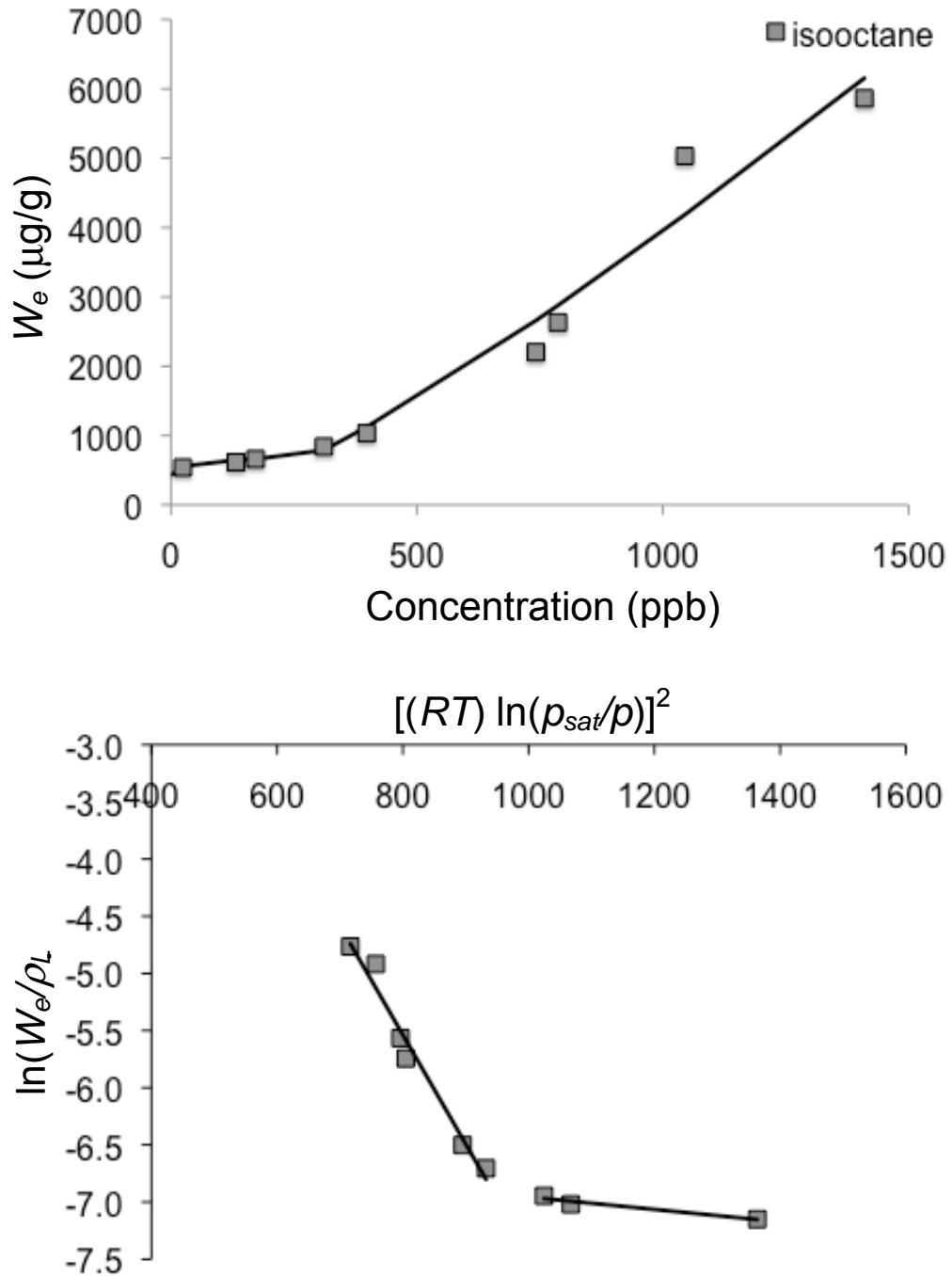


Figure A-20. The isotherm for isooctane on Carbpacck X with the DR modeling result using two energies is shown (top). The linearized isotherm is shown at the bottom indicating the two regions of adsorption yielding two values of E_o .

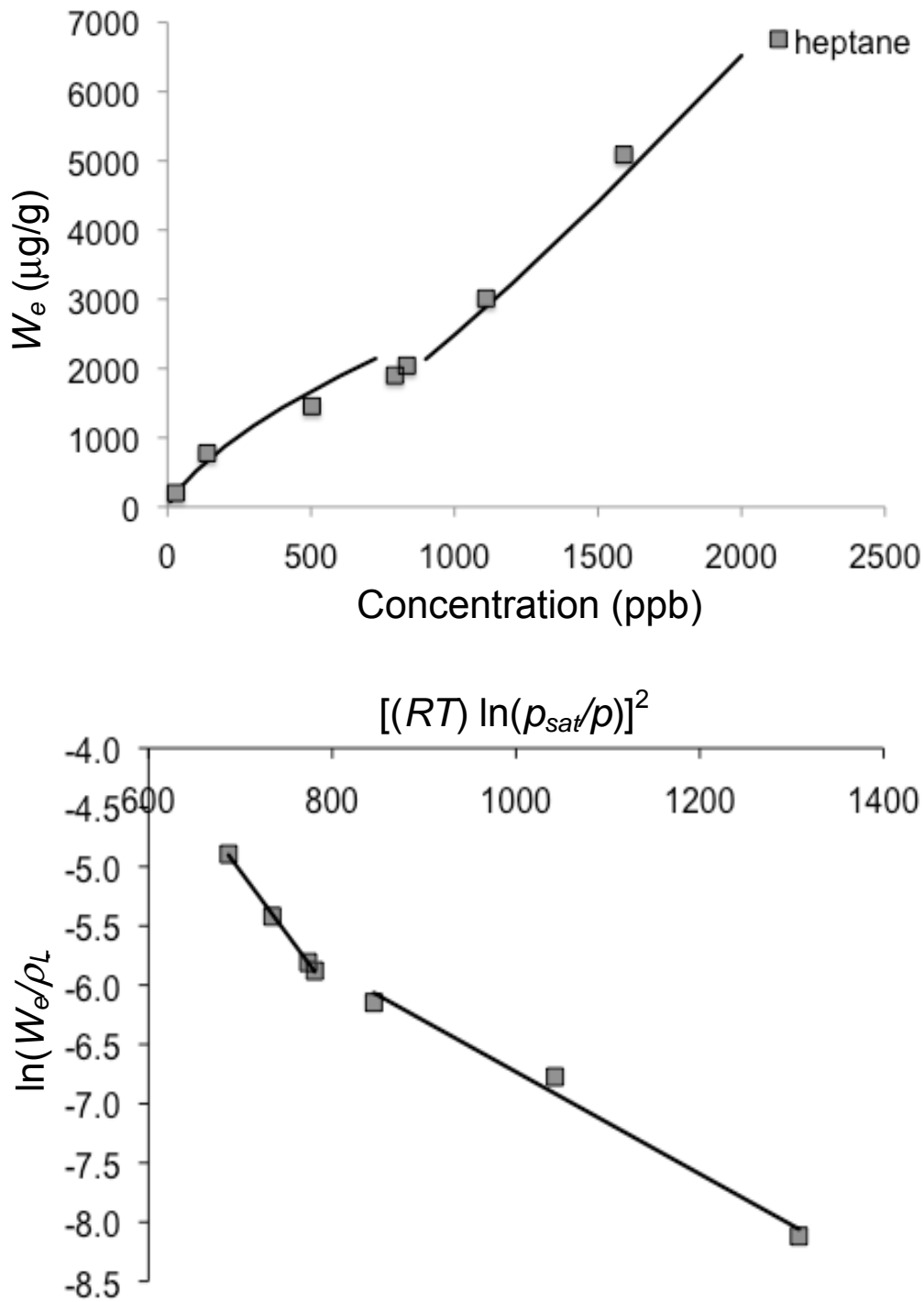


Figure A-21. The isotherm for heptane on Carbpac X with the DR modeling result using two energies is shown (top). The linearized isotherm is shown at the bottom indicating the two regions of adsorption yielding two values of E_o .

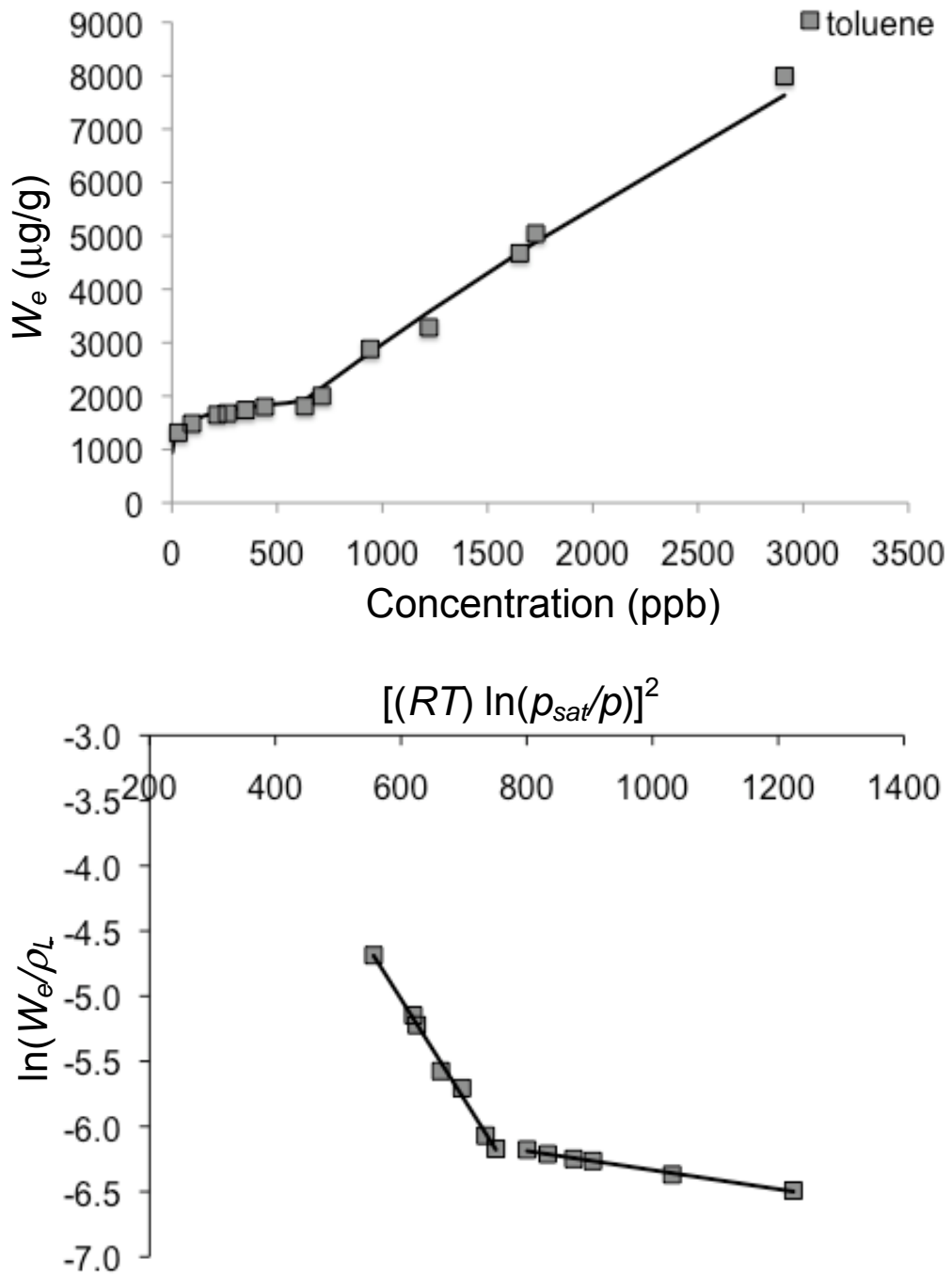


Figure A-22. The isotherm for toluene on Carbpacck X with the DR modeling result using two energies is shown (top). The linearized isotherm is shown at the bottom indicating the two regions of adsorption yielding two values of E_o .

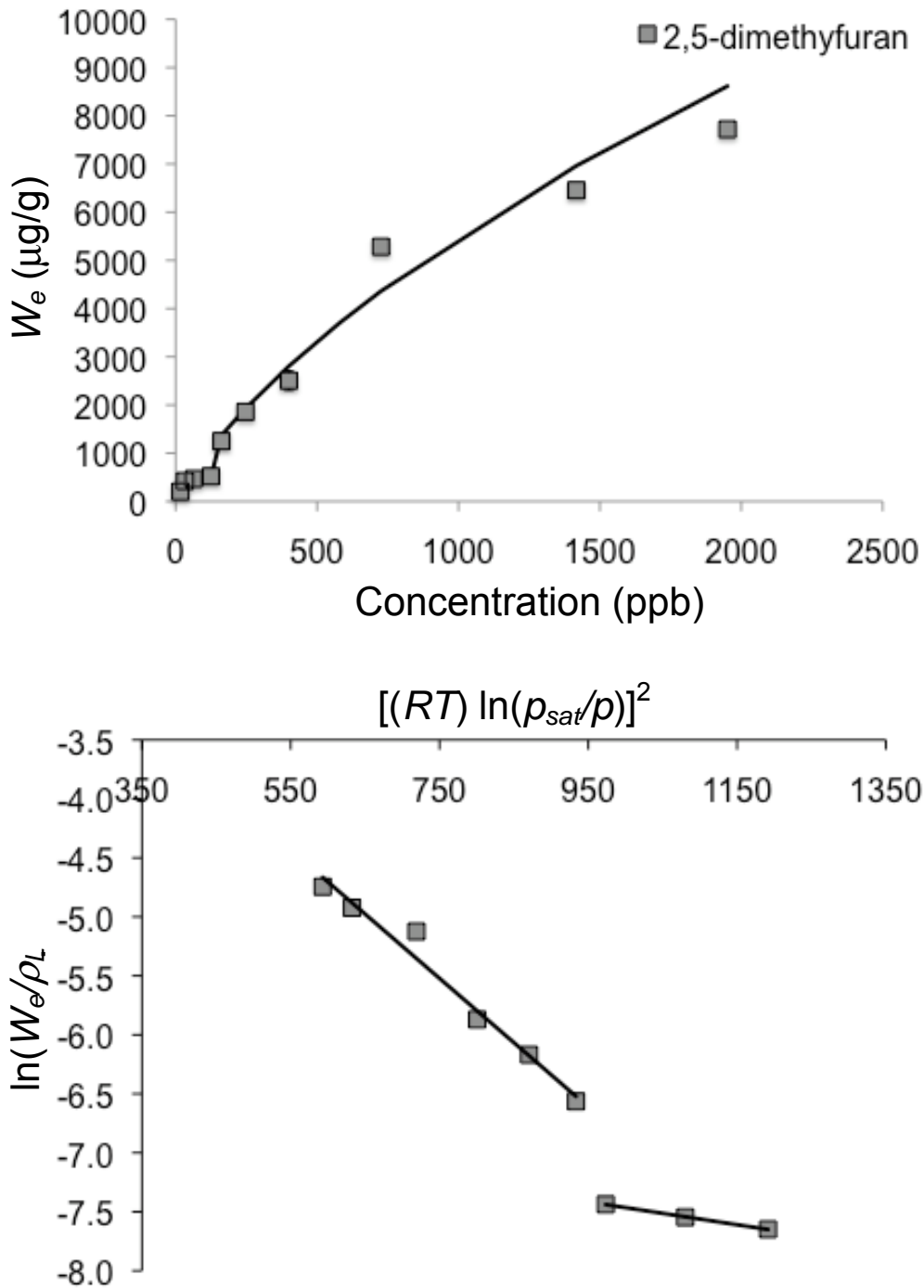


Figure A-23. The isotherm for 2,5-dimethylfuran on Carbopack X with the DR modeling result using two energies is shown (top). The linearized isotherm is shown at the bottom indicating the two regions of adsorption yielding two values of E_o .